REDUCED-ORDER MODELING OF POWER ELECTRONICS COMPONENTS AND SYSTEMS

BY

ALI DAVOUDI

DISSERTATION

Submitted in partial fulfillment of the requirements
for the degree of Doctor of Philosophy in Electrical and Computer Engineering
in the Graduate College of the
University of Illinois at Urbana-Champaign, 2010

Urbana, Illinois

Doctoral Committee:

Associate Professor Patrick L. Chapman, Chair
Professor Philip T. Krein
Professor Peter W. Sauer
Professor Andreas C. Cangellaris

ABSTRACT

This dissertation addresses the seemingly inevitable compromise between modeling fidelity and simulation speed in power electronics. Higher-order effects are considered at the component and system levels. Order-reduction techniques are applied to provide insight into accurate, computationally efficient component-level (via reduced-order physics-based model) and system-level simulations (via multiresolution simulation). Proposed high-order models, verified with hardware measurements, are, in turn, used to verify the accuracy of final reduced-order models for both small- and large-signal excitations.

At the component level, dynamic high-fidelity magnetic equivalent circuits are introduced for laminated and solid magnetic cores. Automated linear and nonlinear order-reduction techniques are introduced for linear magnetic systems, saturated systems, systems with relative motion, and multiple-winding systems, to extract the desired essential system dynamics. Finite-element models of magnetic components incorporating relative motion are set forth and then reduced.

At the system level, a framework for multiresolution simulation of switching converters is developed. Multiresolution simulation provides an alternative method to analyze power converters by providing an appropriate amount of detail based on the time scale and phenomenon being considered. A detailed full-order converter model is built based upon high-order component models and accurate switching transitions. Efficient order-reduction techniques are used to extract several lower-order models for the desired resolution of the simulation. This simulation framework is extended to higher-order converters, converters with nonlinear elements, and closed-loop systems. The resulting rapid-to-integrate component models and flexible simulation frameworks could form the computational core of future virtual prototyping design and analysis environments for energy processing units.

To the most precious, *my sister's smile*

ACKNOWLEDGMENTS

I want to thank the Grainger Center for Electric Machinery and Electromechanics as well as the Office of Naval Research (N00014-5-1-0621), whose generous support has allowed me to pursue my graduate research at the University of Illinois.

I want to express thanks to Professor Patrick Lyle Chapman who gave me the opportunity to study, discuss, argue, and complain. He has patiently mentored me for four years technically, professionally, and personally. His unorthodox approach to research and supervision as well as his professional success relative to his age are inspirational and among the reasons I chose academia (I will hold him accountable for possible consequences). My committee members—Professors Krein, Sauer, and Cangellaris— have played an essential rule in my development as a future researcher. Professor Krein helped me to think outside the box. Professor Sauer was very helpful with system dynamics, and his positive attitude toward sometimes bitter facts of teaching and research is a necessary quality for any true academic. Professor Cangellaris has shed light on many aspects of order-reduction techniques. I also accept the responsibility for future blood-pressure complications of Professor Juri Jatskevich, who spent countless hours on my papers.

I believe I tasked staff members at UIUC and CEME more than any other graduate student. Joyce Mast committed countless hours of individual attention to help me with my writing. She patiently read more than forty manuscripts. My numerous lunches with Karen Driscoll helped me make sense out of the Midwest. Josh and Brandi were always handy with my last-minute paperwork.

Nick Benavides, Bret Nee, Trishan Esram, and YingYing Kuai helped me realize that Professor Chapman is an equal-opportunity, busy adviser. John Ehlman and Charlie were very

helpful with my hardware setups. Sairaj Dhople and Brian Johnson provided me with precious mentorship opportunities to add dimension to my limited scope of research. Matias shared my cynical views about life in the C-U area. Hector Pulgar gracefully left our office at five p.m. so I could take over and start my night shifts.

I am short of words when it comes to thanking my mother, who selflessly endured my five-year absence.

TABLE OF CONTENTS

CHAPTER 1

INTRODUCTION

1.1 Modeling and Simulation Diagram

Switching power converters are building blocks of energy processing units. They are integrated to form complex interconnected multi-converter systems with provisions for hybrid dc and ac distribution, advanced power-system architecture, and improved reliability and performance [1]. These multi-converter structures have also recently found application in hybrid electric vehicles, photovoltaic energy conversion systems, wind farms, and modular microgrids. Future energy processing systems and green energy technologies are likely to be more dependent on power converters.

Modeling and simulation of components and systems of power converters is essential to mimic actual hardware and, therefore, to minimize hardware design iterations and retrofits. Dynamic models are required to study the large signal time-domain transients (e.g., to characterize the losses in the power electronics devices, batteries, and ultra capacitor [2]) as well as small-signal frequency-domain stability and controller design. Simulation-based design tools are used in electric ships for risk analysis, for configuration, and to ensure the final model meets design tolerances [3]. A truly functional virtual/computational prototyping environment [2, 4] is built on existing accurate and efficient modeling and simulation tools (See Fig. 1.1).

Fundamental obstacles to the modeling and simulation are a lack of high-fidelity models, an exhaustive computational burden, and rigid simulation platforms. Automated order-reduction techniques facilitate efficient physics-based component models and flexible simulation

environments that help designers synthesize dynamic behavior of the original system within a tight design cycle. A candidate for efficient simulation frameworks is shown in Fig. 1.2. First physics-based descriptions of components provide highly accurate models. Then, order reduction facilitates system-level integration of physics-based component models in a switching converter model. Order-reduction techniques are then used to provide a flexible-resolution simulation environment.

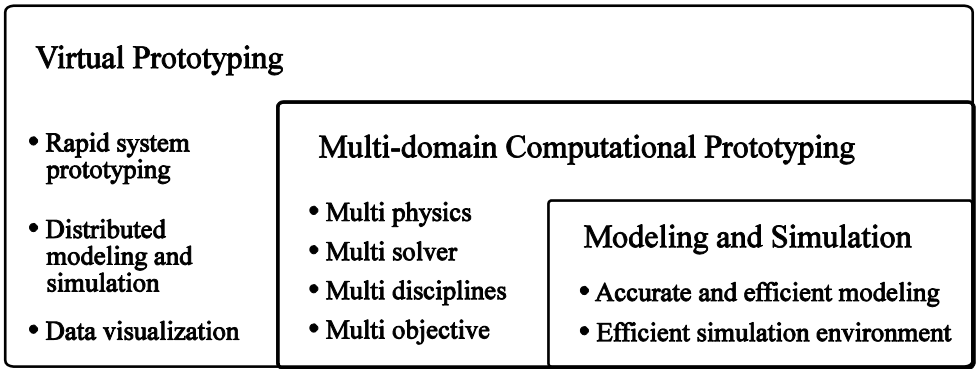

Fig. 1.1. Hierarchical modeling and simulation diagram.

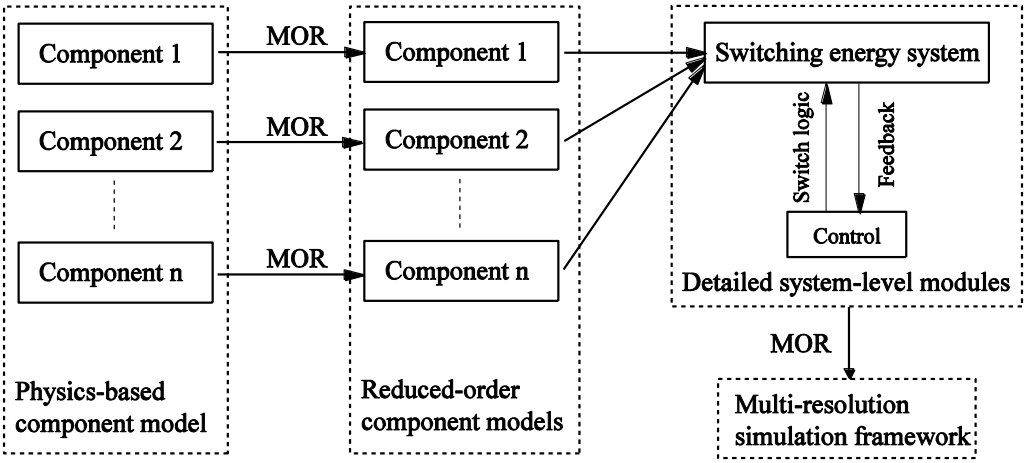

Fig. 1.2. Efficient simulation framework for switching power converters.

1.2 Component-level Modeling and System-level Simulation

Physics-based models are available for various power electronics components, including capacitors [5], IBGTs and MOSFETs [6-8], and diodes [9-11]. Magnetic components are, arguably, the most important ingredients of power electronics systems. Thus, rapid-to-integrate magnetic component models are of paramount value and constitute an active research area [12]. An accurate magnetic model needs to have enough resolution to capture the highest expected frequency. Using the Nyquist criterion as a crude approximation, for a 50 kHz PWM used in motor-drive applications, a minimum of 100,000 samples/second are needed for an adequate sampling. It has been shown in [13] that even if computational power increases exponentially, it will be decades before it reaches the level required for real-time solution of magnetic systems. Iterative methods to implement nonlinear magnetic characteristics add to the computational costs. This becomes a problem especially since magnetic components are part of a larger, more complex and dynamically diverse system.

Magnetic models conventionally lend themselves to behavioral modeling, where many simplifying assumptions severely affect the final macro-model performance. More rigorous approaches, e.g., harmonics analysis, require prior knowledge of system frequencies and need a large number of harmonic field simulations to reach an acceptable level of accuracy [13]. First-principle methods, e.g., finite element methods (FEM) or high-fidelity magnetic equivalent circuits (HFMEC), are highly accurate but computationally expensive. The presence of eddy currents in dynamic FEM or HFMEC models introduces large sets of differential equations, very fast dynamic modes, and ill-conditioned matrix equations. This inevitably leads to numerical instability and slow simulation runs. The problem is exacerbated when nonlinear magnetic systems (e.g., saturated inductors), systems with relative motion (e.g., actuators), and multi-port

systems (e.g., transformers) are considered. Mathematically rigorous order-reduction techniques can be applied to extract low-order dynamic models from high-order, physics-based models.

Although system designers often concentrate on only a few critical issues at a time, the general trend is toward an integrated design approach [14]. Power-processing and energy-conversion systems are complex multi-domain mixtures of electrical, magnetic, mechanical, thermal, and fluid dynamic components that exhibit a wide range of time scales. Consider a typical power propulsion system in transportation fleets such as hybrid vehicles or all-electric ships. These systems include solid-state switching converters with nanosecond-level time constants as well as mechanical prime movers or fuel cells with second-level time constants. Now, if one takes a system snapshot that goes into more detail, each subsystem may also represent a stiff subsystem. For example, a switching converter represents a wide range of dynamics: very high-frequency magnetic components that include eddy current dynamics, high-frequency switching spikes imposed by semiconductor switches and packaging and parasitic effects resulting from circuit layout; medium-range dynamics associated with thermal effects; and, finally, slower dynamics associated with external controller circuitry. Thus, a detailed switch-by-switch simulation of a typical power electronics-based system may include time constants that span ten orders of magnitude. Simulation of this system can be tedious, especially when multi-objective parametric multiple-run optimization studies or real-time simulations are desired.

System-level simulation of power electronics may be conducted at several resolution levels, e.g. steady-state characterization, average-value modeling, switch-level waveforms, etc. If a higher level of resolution is required (e.g., to study very high frequency effects such as switching spikes and transients [15]), the resulting ill-conditioned systems of equations jeopardize simulation stability and make it computationally prohibitive. This is further pronounced when

higher-order converters (e.g., cascaded converters), nonlinear elements (e.g., saturated magnetic components), and external circuitry (e.g., closed-loop systems) are considered. However, a very high level of simulation resolution is not needed for a complete simulation cycle. Thus, a simulation engine with flexible resolution levels is desirable. Order-reduction techniques can be used to extract different simulation resolutions. Such a multiresolution simulation engine can both result in accelerated simulation speed in a lower resolution mode, and utilize a high-resolution mode to "zoom-in" for study of higher-frequency phenomena.

1.3 Dissertation Outline

This dissertation is organized as follows. Chapter 2 covers the fundamentals of order reduction techniques and tools used in the remaining chapters for linear, nonlinear, and multiple-input/multiple-output systems. In Chapter 3, dynamic HFMEC models are introduced that include eddy current effects. Reduced-order magnetic models of linear, nonlinear, time-varying, and multiple-input/multiple-output systems are developed. Chapter 4 utilizes a fixed grid concept in FEM to incorporate relative motion in the final reduced model. Chapter 5 considers the use of order-reduction techniques in flexible simulation of switching converters. Multiresolution simulation environments are developed for different order-reduction techniques and several classes of switching converters. The contributions of this dissertation and future directions are discussed in Chapter 6. Parts of this dissertation are published in [16-24].

CHAPTER 2

MODEL ORDER REDUCTION

The order reduction process replaces the original high-order state space with a lower-order space, while preserving the input-output relationship. Order reduction and model simplification are not new ideas; Newton [25], Taylor [26], Euler [27], Lagrange [28], and Fourier published their work on model simplification and function approximation in 1704, 1715, 1755, 1759, and 1807, respectively. Pade's PhD dissertation and his approximations were published in 1892 [29]. Lanczos [30], Arnoldi [31], Saad/Schultz [32], and Fletcher [33] published their iterative methods, foundations of moment-matching Krylov-subspace techniques, in 1950, 1951, 1976, and 1986, respectively. Moore introduced truncated balanced realization (TBR) [34] in 1981, and Glover published his famous work on Hankel-norm reduction [35] in 1984. Proper orthogonal decomposition was introduced by Sirovich in 1987 [36]. Different classes of Krylov-subspaces methods, explicit moment matching (asymptotic waveform evaluation introduced in 1990 [37]) and implicit moment matching (Pade via Lanczos introduced by Freund in 1993 [38] and Pade via Arnoldi introduced by Silveira in 1995 [39]) currently dominate the order-reduction realm.

2.1 Order Reduction Framework

Power electronics systems can generally be represented by a nonlinear differential algebraic equation (DAE)

$$\begin{cases} \dfrac{d\mathbf{x}}{dt} = \mathbf{F}(\mathbf{x},\mathbf{z},\mathbf{u},t) \\ \mathbf{z} = \mathbf{G}(\mathbf{x},\mathbf{z},\mathbf{u},t) \\ \mathbf{y} = \mathbf{H}(\mathbf{x},\mathbf{z},\mathbf{u},t) \end{cases} \tag{2.1}$$

where **x**, **z**, **u**, and **y** are state variable, algebraic variable, input, and output vectors, respectively. Many order-reduction techniques are applicable only to linear models [40]. Nonlinear order-reduction methods are conventionally based on piecewise linear approaches using various training, projection and weighting processes [41]. Computational efficiency and numerical accuracy can be improved by partitioning the original large system into weakly connected smaller (and possibly linear) subsystems and then applying order-reduction techniques [42]. Linear, time-invariant (LTI) systems are considered first. The algebraic variables in (2.1), **z**, can be removed using primary reduction techniques (e.g., Kron reduction) to form a standard state-space model

$$\begin{cases} \dfrac{d\mathbf{x}}{dt} = \mathbf{A}\mathbf{x} + \mathbf{B}\mathbf{u},\ \mathbf{A} \in \Re^{n\times n}, \mathbf{B} \in \Re^{n\times p}, \mathbf{x} \in \Re^{n} \\ \mathbf{y} = \mathbf{C}\mathbf{x} + \mathbf{D}\mathbf{u},\ \mathbf{C} \in \Re^{p\times n}, \mathbf{D} \in \Re^{p\times p}, \mathbf{u} \in \Re^{p} \end{cases} \tag{2.2}$$

The state trajectory and output of system (2.2) can be computed as

$$\begin{cases} \mathbf{x}(t) = e^{A(t-t_0)}\mathbf{x}(t_0) + \displaystyle\int_{t_0}^{t} e^{A(t-\upsilon)}\mathbf{B}\mathbf{u}(\upsilon)d\upsilon \\ \mathbf{y}(t) = \mathbf{C}e^{A(t-t_0)}\mathbf{x}(t_0) + \mathbf{C}\displaystyle\int_{t_0}^{t} e^{A(t-\upsilon)}\mathbf{B}\mathbf{u}(\upsilon)d\upsilon + \mathbf{D}\mathbf{u}(t) \end{cases} \tag{2.3}$$

which is computationally infeasible for a large system $(n \gg 1)$. A model reduction process seeks to replace (2.2) with a "similar" system

$$\begin{cases} \dfrac{d\mathbf{x}_r}{dt} = \mathbf{A}_r\mathbf{x}_r + \mathbf{B}_r\mathbf{u},\ \mathbf{A}_r \in \Re^{q\times q}, \mathbf{B}_r \in \Re^{q\times p}, \mathbf{x}_r \in \Re^{q} \\ \tilde{\mathbf{y}} = \mathbf{C}_r\mathbf{x}_r + \mathbf{D}_r\mathbf{u},\ \mathbf{C}_r \in \Re^{p\times q}, \mathbf{D}_r \in \Re^{p\times p}, \mathbf{u} \in \Re^{p} \end{cases} \tag{2.4}$$

of the order *q*, much smaller than the original order, *n*. Meanwhile, for the input $\mathbf{u}(t)$, the reduced-order model output, $\tilde{\mathbf{y}}(t)$, closely resembles the original outputs, $\mathbf{y}(t)$:

$$\|\mathbf{y}(t)-\tilde{\mathbf{y}}(t)\| < \varepsilon \tag{2.5}$$

Likewise, transfer functions of systems in (2.2) and (2.4) match for a given tolerance and frequency range:

$$\begin{cases}\mathbf{H}(s)=\mathbf{D}+\mathbf{C}(\mathbf{sI}-\mathbf{A})^{-1}\mathbf{B}\\ \mathbf{H}_r(s)=\mathbf{D}_r+\mathbf{C}_r(\mathbf{sI}-\mathbf{A}_r)^{-1}\mathbf{B}_r\end{cases} \Rightarrow \|\mathbf{H}(s)-\mathbf{H}_r(s)\| \le \varepsilon \tag{2.6}$$

The goal of order reduction is to find $\{\mathbf{A}_r,\mathbf{B}_r,\mathbf{C}_r,\mathbf{D}_r\}$in (2.4) or $\mathbf{H}_r(s)$ in (2.6).

2.2 Linear Order Reduction

Linear order-reduction techniques have mainly been categorized based on their properties or implementation methodologies. Based on their properties, order-reduction techniques are classified as *moment matching* (e.g., Pade, partial realization, etc.) and *singular-value decomposition* (SVD) (e.g., Hankel norm approximation, singular perturbation, etc.). Moment-matching techniques utilize the Arnoldi or Lanczos methods to find an orthonormal transformation basis for system matrices using Krylov subspaces. The SVD-based reduction family acts on the information extracted from Hankel singular values of the balanced system. Based on implementation methodologies, order-reduction techniques are categorized as projection-based (e.g., proper orthogonal decomposition, Krylov-subspace methods, etc.) and non-projection-based (e.g., Hankel optimal model reduction, singular perturbation approximation, transfer function fitting, etc.) [43]. The interested reader can find rigorous discussion of the various reduction techniques and their classifications in [43-48].

Other linear order-reduction methods are based on minimizing the integral of the square error between the impulse response of the high-order and low-order model (Walsh functions [49]). In contrast to "mathematically driven" order-reduction techniques, there are bond-graph based order-reduction techniques that seek to remove those energy components, i.e., state variables, that contribute the least amount of energy to the total system energy [50]. This should effectively be equivalent to "modal reduction" based on the Hankel singular values. In addition to the LTI systems, linear order reduction has been extended to time-varying [51] and frequency-dependent systems [52]. Multiple-input/multiple-output systems are also accommodated by PRIMA [53], block Arnoldi, global Lanczos [54], and global Arnoldi algorithms [55].

Among linear reduction tools used in this dissertation are Kron reduction, fast state elimination, quasi-pole/zero cancellation, state residualization, singular perturbation, and Krylov methods. It should be noted that order-reduction techniques are implemented as tools tailored to our application; their theoretical characteristics are beyond the scope of this thesis. The numerical aspects and error bounds in the final reduced-order model are well known and discussed [56]. Moreover, the majority of these techniques have recently been automated in available numerical toolboxes [57].

2.2.1 Kron reduction

Formulations of HFMEC and FEM yield hundreds or thousands of differential and algebraic variables. For example, the algebraic variables resulting from the FEM formulation forthcoming in Chapter 4 are the magnetic vector potentials, **A**, associated with the nodes in the air. There are systematic ways to extract several sets of ODEs from the original DAEs. The algebraic variables are excluded from the DAE, e.g., using Kron reduction [58-59], named after the famous power

system engineer Gabriel Kron in 1939 [60]. Kron reduction is used to eliminate the magnetic vector potentials in the magnetic materials of a power transformer [61] or induction machine [58], assuming linearity of the magnetic material. After differential equations associated with FEM are discretized and replaced by algebraic equations (similar to EMTP simulation environments [62]), Kron reduction is used to eliminate air-gap variables [63]. This leaves us with a minimal set of differential equations.

A simple demonstration of Kron reduction is given here. One may consider a linear DAE in descriptor form, where the variable vector, $\boldsymbol{x}$, is partitioned into the state variables, $\boldsymbol{x}_s$, and algebraic variables, $\boldsymbol{x}_a$, with zero dynamics:

$$\begin{bmatrix} \mathbf{E}_{ss} & 0 \\ 0 & 0 \end{bmatrix} \frac{d}{dt} \begin{bmatrix} \mathbf{x}_s \\ \mathbf{x}_a \end{bmatrix} = \begin{bmatrix} \mathbf{A}_{ss} & \mathbf{A}_{sa} \\ \mathbf{A}_{as} & \mathbf{A}_{aa} \end{bmatrix} \begin{bmatrix} \mathbf{x}_s \\ \mathbf{x}_a \end{bmatrix} + \begin{bmatrix} \mathbf{b}_s \\ \mathbf{b}_a \end{bmatrix} u \ . \tag{2.7}$$

Subscripts *s* and *a* denote state and algebraic variables, respectively. By eliminating the algebraic variable, $\boldsymbol{x}_a$, using Gaussian elimination, the state-variable dynamics are found:

$$\mathbf{E}_{ss} \frac{d\mathbf{x}_s}{dt} = \left[\mathbf{A}_{ss} - \mathbf{A}_{aa}^{-1}\mathbf{A}_{as}\right]\mathbf{x}_s + \left[\mathbf{b}_s - \mathbf{A}_{aa}^{-1}\mathbf{b}_a\right]u \ . \tag{2.8}$$

The algebraic variables, $\boldsymbol{x}_a$, can be obtained from state variables, $\boldsymbol{x}_s$, and input, *u*, as

$$\mathbf{x}_a = -\mathbf{A}_{aa}^{-1}\mathbf{A}_{as}\mathbf{x}_s - \mathbf{A}_{aa}^{-1}\mathbf{b}_a u \ . \tag{2.9}$$

This is a primary stage in reducing the model order. Kron reduction will be used in Chapter 4 to remove the air-gap nodes from a FEM formulation of electromechanical systems.

2.2.2 Fast state elimination

Formulations of HFMEC and FEM usually yield a wide range of dynamic modes. Consider the state equations

$$\dot{\mathbf{x}} = \mathbf{A}\mathbf{x}, \quad \mathbf{x} \in \Re^n \tag{2.10}$$

We make the blanket assumption that **A** has a set of *n* distinct eignevalues. One may form a diagonal matrix of eigenvalues, λ_i, and matrices whose columns are sets of corresponding left, $\mathbf{l}_i$, and right, $\mathbf{r}_i$, eigenvectors as

$$\begin{cases} \mathbf{\Lambda} = diag\{\lambda_1, \lambda_2 \cdots \lambda_n\} \\ \mathbf{V} = [\mathbf{r}_1, \mathbf{r}_2, \cdots, \mathbf{r}_n] \\ \mathbf{V}^{-1} = [\mathbf{l}_1, \mathbf{l}_2, \cdots, \mathbf{l}_n]' \end{cases} \tag{2.11}$$

which can be used to decouple the dynamic modes in (2.10)

$$\dot{\mathbf{z}} = \mathbf{V}^{-1}\mathbf{A}\mathbf{V}\mathbf{z} = \mathbf{\Lambda}\mathbf{z} \quad \Rightarrow \quad z_i(t) = z_i(0)e^{\lambda_i t} \tag{2.12}$$

Some dynamic modes are beyond what is physically meaningful. This is mainly because of the assumptions made in the model development stage. Stray capacitors and displacement currents are neglected in both FEM and HFMEC formulations, and resulting dynamic modes beyond a few MHz are invalid. Also, the fast dynamic modes subside quickly and their contribution is small. Thus, the fast eigenvalues of the decoupled system can be eliminated. This leads to a reduced-order model

$$\begin{cases} \dot{\mathbf{x}}_r = \mathbf{V}_r \mathbf{\Lambda}_r \mathbf{V}_r^{-1} \mathbf{x}_r, \mathbf{x}_r \in \Re^q \\ \mathbf{\Lambda}_r = diag\{\lambda_1, \lambda_2, \cdots, \lambda_q\} \\ \mathbf{V}_r = [\mathbf{r}_1^{/}, \mathbf{r}_2^{/}, \cdots, \mathbf{r}_q^{/}] \end{cases} . \tag{2.13}$$

The fast state elimination belongs to the SVD-based, non-projection methods.

2.2.3 Quasi pole/zero cancellation

Quasi pole/zero cancellation is similar to the transfer-fitting approach and the simplified convex optimization method [64], which are non-projecting approaches. This method aims to approximate the transfer function of the original model in (2.6) at a given frequency range (usually a lower frequency range). Dynamic input-impedance characterization of a HFMEC usually leads to closely spaced poles and zeros that vary over a wide range of frequencies

$$z_{in}(s)=\frac{v_{in}(s)}{i_{in}(s)}=\prod_{i=1}^{n}k\frac{(s-z_i)}{(s-p_i)} \tag{2.14}$$

The quasi pole/zero cancellation is utilized to eliminate the pole/zero pair if their difference is less than some tolerance level (e.g., 10%). An updated gain/pole/zero set constitutes a new state-space formulation, with a new order, $q<<n$. The dc gain of the resulting reduced-order model is adjusted to be the same as the dc gain of the original full-order model

$$z_{in}^{r}(s)=\frac{v_{in}(s)}{i_{in}(s)}=\prod_{i=1}^{q}k'\frac{(s-z_i)}{(s-p_i)},\quad \left|\frac{z_i-p_i}{p_i}\right|>\varepsilon \tag{2.15}$$

2.2.4 Balanced system approaches

Balanced system approaches are SVD-based methods. They first transform the coordinates of the original state space, i.e., balance the system. The main idea is to transform the system to a base where the states that are difficult to reach are simultaneously difficult to observe, and later truncate those states or associated dynamics. This is done by changing the system coordinates such that the observability and controllability Gramian matrices are equal. The state vector of the balanced system is ordered based on the state contributions to the input-output relationship (Hankel singular values). Then, for a given cut-off Hankel singular value, the last (*n*-*q*) state

variables, or their dynamics, are eliminated. The variables *n* and *q* are the model order for the full and reduced order models, respectively. In truncated balanced residualization (TBR) methods, unimportant state variables are set to zero. In singular perturbation approximation (SPA) methods [65], one may set the derivative of the "unimportant" states to zero. Both methods rely on the information obtained from the controllability, $\mathbf{W}_c$, and observability, $\mathbf{W}_o$, Gramians

$$\begin{cases} \mathbf{W}_c = \int_0^\infty e^{\mathbf{A}t}\mathbf{B}\mathbf{B}^T e^{\mathbf{A}^T t}dt \\ \mathbf{W}_o = \int_0^\infty e^{\mathbf{A}^T t}\mathbf{C}^T\mathbf{C}e^{\mathbf{A}t}dt \end{cases} \tag{2.16}$$

These Gramians are found by solving the following (dual) Lyapunov equations:

$$\begin{cases} \mathbf{A}\mathbf{W}_c + \mathbf{W}_c\mathbf{A}^T = -\mathbf{B}\mathbf{B}^T \\ \mathbf{W}_o\mathbf{A} + \mathbf{A}^T\mathbf{W}_o = -\mathbf{C}^T\mathbf{C} \end{cases}. \tag{2.17}$$

Hankel singular values are extracted as the square roots of the products of eigenvalues of two Gramians:

$$\delta_i = \sqrt{eig\left(\mathbf{W}_c\mathbf{W}_o\right)}, \quad i = 1\cdots n \tag{2.18}$$

Hankel singular values contain useful information about the input-output relationship; the states with small singular values have a weaker effect on input-output relationships and most likely are less controllable/observable. Thus, states with smaller Hankel singular values can be removed. To accomplish this, one should use a change of coordinates to balance the system, i.e., give it equal, diagonal Gramians. In particular, one may solve for a balancing transformation matrix **T**

$$\begin{cases} \mathbf{W}_c\mathbf{W}_o\mathbf{T} = \mathbf{T}\mathbf{\Sigma}^2 \\ \mathbf{\Sigma} = diag\left\{\delta_1, \delta_2, \cdots, \delta_n\right\} \end{cases} \tag{2.19}$$

This matrix then can be used to equate and diagonalize the Gramian matrices in (2.15)

$$\begin{cases} \mathbf{W}_c \to \mathbf{T}^{-1}\mathbf{W}_c\mathbf{T}^{-T} \\ \mathbf{W}_o \to \mathbf{T}^{T}\mathbf{W}_o\mathbf{T} \end{cases} \tag{2.20}$$

and to balance the state equations in (2.2) by a change of coordinates

$$\begin{cases} \dfrac{d\tilde{\mathbf{x}}}{dt} = \tilde{\mathbf{A}}\tilde{\mathbf{x}} + \tilde{\mathbf{B}}\mathbf{u} & ,\tilde{\mathbf{A}} = \mathbf{T}\mathbf{A}\mathbf{T}^{-1}, \tilde{\mathbf{B}} = \mathbf{T}\mathbf{B} \\ \mathbf{y} = \tilde{\mathbf{C}}\tilde{\mathbf{x}} + \tilde{\mathbf{D}}\mathbf{u} & ,\tilde{\mathbf{C}} = \mathbf{C}\mathbf{T}^{-1}, \tilde{\mathbf{D}} = \mathbf{D} \end{cases} \tag{2.21}$$

In the resulting balanced system, the full state vector is balanced and partitioned, based on state contributions to the input-output response (or corresponding Hankel singular values):

$$\tilde{\mathbf{x}} = \mathbf{T}\mathbf{x} = \begin{bmatrix} \tilde{\mathbf{x}}_1 \\ \cdots \\ \tilde{\mathbf{x}}_2 \end{bmatrix} \tag{2.22}$$

where $\tilde{\mathbf{x}}_1$ and $\tilde{\mathbf{x}}_2$ are state variables associated with significant and small Hankel singular values, respectively. The system matrices are partitioned accordingly. Magnetic systems are usually modeled with voltage as the input variable, v_{in}, and current, i_{in}, as the output variable. Thus, one may have a partitioned system as in

$$\begin{cases} \dot{\tilde{\mathbf{x}}} = \begin{bmatrix} \dot{\tilde{\mathbf{x}}}_1 \\ \cdots \\ \dot{\tilde{\mathbf{x}}}_2 \end{bmatrix} = \tilde{\mathbf{A}}\tilde{\mathbf{x}} + \tilde{\mathbf{b}}v_{in} = \begin{bmatrix} \tilde{\mathbf{A}}_{11} & \vdots & \tilde{\mathbf{A}}_{12} \\ \cdots & \cdots & \cdots \\ \tilde{\mathbf{A}}_{21} & \vdots & \tilde{\mathbf{A}}_{22} \end{bmatrix} \begin{bmatrix} \tilde{\mathbf{x}}_1 \\ \cdots \\ \tilde{\mathbf{x}}_2 \end{bmatrix} + \begin{bmatrix} \tilde{\mathbf{b}}_1 \\ \cdots \\ \tilde{\mathbf{b}}_2 \end{bmatrix} v_{in} \\ i_{in} = \tilde{\mathbf{C}}\tilde{\mathbf{x}} + dv_{in} = \begin{bmatrix} \tilde{\mathbf{C}}_1 & \tilde{\mathbf{C}}_2 \end{bmatrix} \begin{bmatrix} \tilde{\mathbf{x}}_1 \\ \cdots \\ \tilde{\mathbf{x}}_2 \end{bmatrix} + dv_{in} \end{cases} \tag{2.23}$$

From this point, one can use either the state truncation (TBR) or state residualization (SPA) approaches. In SPA, the reduced-order model is extracted by setting the derivative of the state variables with small Henkel singular values, $\tilde{\mathbf{x}}_2$, to zero and modifying (2.23)

$$\begin{cases} \dot{\tilde{\mathbf{x}}}_1 = \underbrace{\left(\tilde{\mathbf{A}}_{11} - \tilde{\mathbf{A}}_{12}\left(\tilde{\mathbf{A}}_{22}\right)^{-1}\tilde{\mathbf{A}}_{21}\right)}_{\mathbf{A}_r}\tilde{\tilde{\mathbf{x}}}_1 + \underbrace{\left(\tilde{\mathbf{b}}_1 - \tilde{\mathbf{A}}_{12}\left(\tilde{\mathbf{A}}_{22}\right)^{-1}\tilde{\mathbf{b}}_2\right)}_{\mathbf{B}_r}v_{in} \\ i_{in} = \underbrace{\left(\tilde{\mathbf{C}}_1 - \tilde{\mathbf{C}}_2\left(\tilde{\mathbf{A}}_{22}\right)^{-1}\tilde{\mathbf{A}}_{21}\right)}_{\mathbf{C}_r}\tilde{\tilde{\mathbf{x}}}_1 + \underbrace{\left(d - \tilde{\mathbf{C}}_2\left(\tilde{\mathbf{A}}_{22}\right)^{-1}\tilde{\mathbf{b}}_2\right)}_{D_r}v_{in} \end{cases} \tag{2.24}$$

The resulting reduced-order model does not match at very high frequency $\left(d \neq \mathbf{D}_r\right)$, but the dc-gain match between the reduced and full-order models is guaranteed [44]:

$$H(0) = \mathbf{CA^{-1}B} + \mathbf{D} = \mathbf{C}_r\mathbf{A}_r^{-1}\mathbf{B}_r + \mathbf{D}_r = H_r(0) \tag{2.25}$$

In the TBR method, the reduced-order model is extracted by eliminating the state variables with small Henkel singular values, $\tilde{\tilde{\mathbf{x}}}_2$, and truncating (2.23):

$$\begin{cases} \dot{\tilde{\mathbf{x}}}_1 = \tilde{\mathbf{A}}_{11}\tilde{\tilde{\mathbf{x}}}_1 + \tilde{\mathbf{b}}_1 v_{in} \\ i_{in} = \tilde{\mathbf{C}}_1\tilde{\tilde{\mathbf{x}}}_1 + dv_{in} \end{cases} \tag{2.26}$$

It should be noted that (2.26) is the same as (2.13) if the participation factors of the fast dynamic modes are small. The reduced- and full-order model transfer functions in (2.6) do not match in DC, but converge to *d* at a very high frequency:

$$H(\infty) = d = H_r(\infty) \tag{2.27}$$

Error bounds for the q^{th}-order reduced model in the frequency domain can be calculated [66] as

$$\left\|H(s) - H_r(s)\right\|_\infty \leq 2\sum_{k=q+1}^{n}\delta_k \tag{2.28}$$

TBR and SPA methods are projection-based and non-projection-based methods, respectively. For relatively small systems, e.g., fewer than 100 state variables, SVD-based methods are superior in accuracy to moment-matching techniques (e.g., Krylov subspace). For larger systems, balancing and truncating the equations makes the reduction process computationally intractable.

The computational intensity is O(n^3), where n is the model order. Thus, SVD-based methods are usually used in a hybrid fashion in conjunction with another method. For example, in Chapter 3, SPA follows the initial reduction technique, quasi pole-zero cancellation, to reduce the HFMEC of a linear inductor.

2.2.5 Krylov-subspace methods

Krylov-subspace order-reduction techniques have long been used in many applications (e.g., communication systems [51], [67], electric circuits [68], [69], digital VLSI [70], MEMS [71], high-speed interconnection [72-73], multi-conductor transmission line [74], electromagnetic [75-77], and power systems [78]); their application in power electronics has been little researched. Krylov-subspace-based methods are projection-based, moment-matching techniques that project a higher-order state space into a lower-order space. The space projection and order reduction is in following form:

$$\begin{cases} \dfrac{d\mathbf{x}_r}{dt} = \mathbf{A}_r\mathbf{x}_r + \mathbf{B}_r\mathbf{u} & ,\mathbf{A}_r = \mathbf{W}^T\mathbf{A}\mathbf{V}, \mathbf{B}_r = \mathbf{W}^T\mathbf{B} \\ \tilde{\mathbf{y}} = \mathbf{C}_r\mathbf{x}_r + \mathbf{D}_r\mathbf{u} & ,\mathbf{C}_r = \mathbf{C}\mathbf{V}, \mathbf{D}_r = \mathbf{D} \end{cases} \tag{2.29}$$

where columns of matrices **W** and **V** span Krylov subspaces. The Krylov subspace $\mathbf{K}_q(\mathbf{M}, \mathbf{v})$ of order q is the space spanned by the set of vectors generated from matrix **M** and vector **v**

$$\mathbf{K}_q(\mathbf{M}, \mathbf{v}) = span\left\{\mathbf{v}, \mathbf{M}\mathbf{v}, \cdots, \mathbf{M}^{q-1}\mathbf{v}\right\} \tag{2.30}$$

Different choices of **W**, **V**, **M**, and **v** in (2.29)-(2.30) lead to different Krylov methods. For example, this thesis utilizes the Arnoldi implementation which is a variation of modified Gram-Schmidt orthogonalization [79]. The components of Krylov subspace in (2.29) and (2.30) are

$$\mathbf{W} = \mathbf{V},\ \mathbf{M} = \mathbf{A}^{-1},\ \mathbf{v} = \mathbf{A}^{-1}\mathbf{B} \qquad . \tag{2.31}$$

Thus, an orthogonal projection matrix, **W**, is extracted from the q^{th}-order Krylov subspace:

$$\mathbf{K}_q\left(\mathbf{A}^{-1},\mathbf{B}\right) = span\left\{\mathbf{B},\mathbf{A}^{-1}\mathbf{B},\cdots,\left(\mathbf{A}^{-1}\right)^{q-1}\mathbf{B}\right\} \tag{2.32}$$

Then, the full-order state vector is projected into a lower-order state vector by a similarity transform:

$$\mathbf{x}_r = \mathbf{W}\mathbf{x},\ \mathbf{x}_r \in \Re^q,\ \mathbf{W} \in \Re^{q\times n},\ \mathbf{x} \in \Re^n \tag{2.33}$$

By a similar transformation, the resulting reduced-order model is

$$\begin{cases} \dfrac{d\mathbf{x}_r}{dt} = \mathbf{W}\mathbf{A}\mathbf{W}^T\mathbf{x}_r + \mathbf{W}\mathbf{B}\mathbf{u} = \mathbf{A}_r\mathbf{x}_r + \mathbf{B}_r\mathbf{u} \\ \mathbf{y} = \mathbf{C}\mathbf{W}^T\mathbf{x}_r + \mathbf{D}\mathbf{u} = \mathbf{C}_r\mathbf{x}_r + \mathbf{D}_r\mathbf{u} \end{cases} \tag{2.34}$$

Based on the moment-matching property of Krylov-subspace methods, the reduced- and full-order model transfer functions in (2.6) match up with the first q moments around a chosen frequency point, s_o.

$$H^{(k)}(s_0) = H_r^{(k)}(s_0), \quad k = 1\cdots q \tag{2.35}$$

where the transfer-function moments, $H^{(0)}(s_0), H^{(1)}(s_0),\ldots$, at the frequency point, s_0, are defined as terms in Taylor series expansion of the transfer function, **H**(s), around the point s_0 as

$$H^{(k)}(s_0) = \frac{1}{k!}\frac{d^k}{dt}H(s)\Big|_{s=s_0} = \mathbf{C}\left(\left(\mathbf{A}-s_0\mathbf{I}\right)^{-1}\mathbf{I}\right)^k\left(\mathbf{A}-s_0\mathbf{I}\right)^{-1}\mathbf{B} \tag{2.36}$$

Krylov-subspace methods are valid only in a narrow frequency range and large-signal fidelity is not always guaranteed. Also, as opposed to the SVD-based method, error bounds are not

known a priori. Krylov-subspace methods are computationally efficient $(o(n))$, especially with a sparse **A** matrix, and are thus attractive options for large scale systems.

2.3 Nonlinear and Parametric Order Reduction

Magnetic systems are mainly nonlinear due to the presence of saturation. Order-reduction of weakly and strongly nonlinear systems is usually addressed by trajectory piecewise linear techniques (moment matching [79], [80] truncated balance realization [81], and piecewise polynomial [82]). Order reduction of nonlinear systems represents a special challenge, requiring good local and global accuracy. Piecewise polynomial nonlinear order-reduction techniques [42] mix polynomial-based order-reduction techniques (with good small-signal fidelity [83], [84]) and piecewise linear methods. The latter represents a nonlinear system as a collage of linear models in adjoining polytopes centered around an expansion point in state space (with large-signal fidelity [58]). Because covering the entire state space with linear approximations would be computationally expensive, the nonlinear system is simulated with some training input, and only the trajectory of the states excited by those inputs is populated by the linearized models. As an example, consider the nonlinear system

$$\frac{d\mathbf{x}}{dt} = \mathbf{f}(\mathbf{x}) + \mathbf{Bu} \tag{2.37}$$

The nonlinear function can be approximated with a convex combination of affine functions

$$\frac{d\mathbf{x}}{dt} = \sum_{i=1}^{k-1} \omega_i(\mathbf{x},\mathbf{X})\left[\mathbf{A}_i\mathbf{x} + \mathbf{h}_i\right] + \mathbf{Bu} \tag{2.38}$$

The weighting functions $\omega_i(\mathbf{x},\mathbf{X})$ depend on the current state, **x**, and *k* linearization point in

$$\mathbf{X} = \left[\mathbf{x}_1, \mathbf{x}_2, \cdots, \mathbf{x}_k\right] \tag{2.39}$$

In a standard trajectory piecewise linear method [79], the linearization points, $\mathbf{x}_i$, are chosen as the state vectors along trajectories of (2.37). The first-order linearized coefficients are found through the Jacobean of the nonlinear matrix, **f**:

$$\begin{cases} \mathbf{A}_i = \mathbf{J}_f\left(\mathbf{f}(\mathbf{x})\right)\Big|_{\mathbf{x}_i} \\ \mathbf{h}_i = \mathbf{f}(\mathbf{x}_i) - \mathbf{J}_f\left(\mathbf{f}(\mathbf{x})\right)\Big|_{\mathbf{x}_i} \mathbf{x}_i \end{cases} \tag{2.40}$$

Using the projection-based order-reduction techniques, one can reduce (2.38) to

$$\begin{cases} \dfrac{d\mathbf{x}_r}{dt} = \displaystyle\sum_{i=1}^{k-1} \omega_i(\mathbf{x}_r, \mathbf{X}_r)\left[\mathbf{A}_{i,r}\mathbf{x}_r + \mathbf{h}_{i,r}\right] + \mathbf{B}_r\mathbf{u},\ \mathbf{A}_{i,r} = \mathbf{V}^T\mathbf{A}_i\mathbf{V},\ \mathbf{B}_r = \mathbf{V}^T\mathbf{B} \\ \mathbf{X}_r = \left[\mathbf{V}^T\mathbf{x}_1, \mathbf{V}^T\mathbf{x}_2, \cdots, \mathbf{V}^T\mathbf{x}_k\right]\ \mathbf{x}_r = \mathbf{V}^T\mathbf{x},\ \mathbf{h}_{i,r} = \mathbf{V}^T\mathbf{h}_i \end{cases} \tag{2.41}$$

There are different weighting schemes, $\omega_i(\mathbf{x},\mathbf{X})$ [85], as well as methods for generating the columns of projection matrix, **V** (e.g., Krylov vectors of the individual linearized systems [79] or dominant singular vectors from simulated trajectories [86]).

However, the accuracy of the final reduced-order model depends highly on the input chosen for training and the resulting linearized point in (2.39). Also, large-signal time-domain transients of the full-order model are required for the training. This process is very time-consuming. Later, an approximate training trajectory is introduced by simulating only the partially created reduced-order model. A new linearized/reduced model is generated when a new approximated state falls outside a pre-defined neighborhood of the previous state [79]. Reliability and stability of the reduction process for piecewise linear models are discussed in [87].

Magnetic systems might have time-varying external parameters. For example, it will be shown in Chapters 3 and 4 that an electromechanical system can be modeled as a position/speed-

dependent inductor coupled with force formulation. Mechanical position and speed are externally provided by the mechanical domain subsystem as parameters into the magnetic domain subsystem. Parametric order-reduction techniques have long been investigated in the literature. Different techniques for linear systems are developed (e.g., statistical performance valuation [88], moment matching [89], [90], truncated balance realization [91], and quasi-convex optimization [64]). In general, nonlinear parametric order-reduction techniques require linearization and subsequent order reduction in parameter space as well as state space [71], [92]. Therefore, the computational burden of time-domain training is still unavoidable and even more time-consuming.

To avoid costly large-scale transient simulation required for time-domain training, we will resort to training based on steady-state solutions. A magnetic system is usually modeled with v_{in} as the input, i_{in} as the output, ϕ as the state variable, and mechanical position and speed, x_m and v_m, as parameters. The general form can be both nonlinear, i.e., a function of flux, and time-varying, i.e., a function of mechanical position/speed

$$\begin{cases} \dfrac{d\Phi}{dt} = \mathbf{F}\left(\Phi, x_m, v_m, v_{in}\right) \\ i_{in} = g\left(\Phi, x_m, v_m, v_{in}\right) \end{cases} \tag{2.42}$$

The mechanical position and speed are provided by the external mechanical sub-domain. Thus, piecewise representation of (2.42) is

$$\begin{cases} \dfrac{d\Phi}{dt} = \mathbf{A}\Phi + \mathbf{b}v_{in} = \mathbf{J}_F\left(\Phi\right)\Phi + \mathbf{J}_F\left(v_{in}\right)v_{in} \\ i_{in} = \mathbf{C}\Phi + dv_{in} = \mathbf{J}_g\left(\Phi\right)\Phi + \mathbf{J}_g\left(v_{in}\right)v_{in} \end{cases} \tag{2.43}$$

where the Jacobian matrices are evaluated at externally determined mechanical operating points, $(\mathrm{x}_m, \mathrm{V}_m)$, and the nominal flux, Φ_0 (determined by the dc input current, $\mathrm{I_{in}}$). The details of model derivation in (2.42) will be given in the corresponding sections in Chapters 3 and 4.

The linear model in (2.43) can be reduced using any linear order-reduction technique in Chapter 2.2. The resulting reduced-order model can be represented by a state-space model, rational function, or set of gain/pole/zero associated with the input-admittance transfer function

$$\begin{cases} \dfrac{d\Phi}{dt} = \mathbf{A}_r \Phi + \mathbf{b}_r v_{in} \\ i_{in} = \mathbf{C}_r \Phi + d_r v_{in} \end{cases} \Rightarrow \frac{i_{in}}{v_{in}} = \mathbf{C}_r \left[s\mathbf{I} - \mathbf{A}_r \right]^{-1} \mathbf{b}_r + d_r = \prod_{i=1}^{q} k \frac{(s - z_i)}{(s - p_i)} = \\ \frac{a_q s^q + a_{q-1} s^{q-1} + \cdots + a_1 s + a_0}{b_q s^q + b_{q-1} s^{q-1} + \cdots + b_1 s + b_0} \qquad (2.44)$$

One may save the state matrices, $\{\mathbf{A}_r, \mathbf{b}_r, \mathbf{C}_r, d_r\}$, rational function coefficients, $\{a_i, b_i\}$, or gain/pole/zero sets, $\{k, z_i, p_i\}$, for future use as lookup tables. These lookup tables are parameterized, possibly as functions of dc input current levels, I_{in}, and mechanical characteristics, $\{x_m, v_m\}$. The final piecewise linear model is shown in Fig. (2.1) and can be used for time-domain transient simulation. At a given point in time, t_n, the mechanical subsystem inputs $\{x_m(t_n), v_m(t_n)\}$ and the current $i_{in}(t_n)$ are fed to the lookup tables to interpolate and find corresponding gain/pole/zero sets $\{K(t_n), z_i(t_n), p_i(t_n)\}$. This set is transformed into a canonical state space form, which is implemented by any general-propose ODE solver. This yields the system output at the next time step, $i_{in}(t_{n+1})$. This process is repeated for the full cycle of transient simulation run.

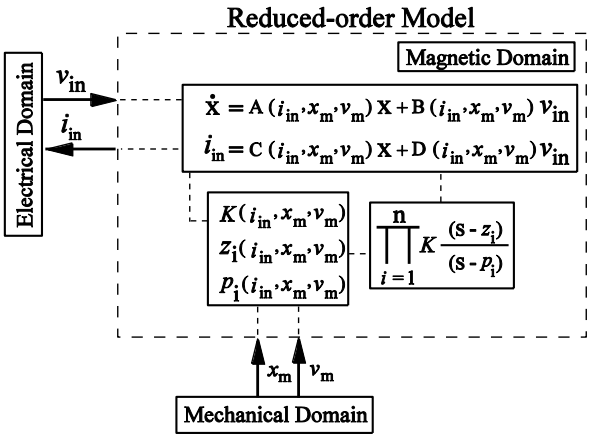

Fig. 2.1. Nonlinear order-reduction framework.

2.4 Order-reduction Criteria

To effectively utilize the reduction process in an automated design environment, special attention should be paid to the choice of reduction technique and the final model order. Among the techniques introduced in this chapter, Kron reduction is used to remove the algebraic variables from the DAE set of equations. If an impedance/admittance transfer function of a magnetic system is available, quasi pole/zero cancellation is a more suitable reduction tool. Considering the computational costs involved in balanced reduction techniques, they are typically used in combination with other reduction techniques. Among balanced reduction techniques, state residualizations and truncations are more accurate at dc and very high frequencies, respectively. For systems with more than 100 state variables, Krylov-subspace techniques are preferred.

The final model order is determined based on the assumptions in model formulation, desired model bandwidth, numerical stability, and computational costs. For example, displacement currents and windings capacitance are neglected in HFMEC and FEM formulation of the linear inductor in Section 3.2. Thus, the original full-order model is valid in frequency ranges up to

several MHz. Subsequently, a low order sufficient to resemble system dynamics within a few MHz range is satisfactory. The desired model bandwidth depends on the underlying application and frequency content of excitation signal. For example, higher-order models are required for applications in which the magnetic system is excited with high-frequency PWM signals that have rich harmonic content.

The model order determination for nonlinear systems has not yet been fully formulated and is a subject of ongoing research. In those applications, the final model order is decided empirically. If the time-domain transient of the original high-order model is available, one can compare it to a medium model-order and, if a match is reported, further reduce the model order. This cycle is repeated until an acceptable match is no longer found. Without the response from the higher-order model, one can start with the lowest-order model plausible considering the engineering judgment. Then, the model order is increased and resulting waveforms are compared to those of previous-order models. If a noticeable difference is reported, the order of the reduced model is increased until sequentially reduced models produce similar results. This approach is computationally more efficient.

Engineering judgment and intuition can help in determining the final model order. For example, in a two-winding transformer with external inductances, there are four state variables (two for external inductances, one for dominant eddy-current dynamics, and one for the magnetizing inductance). The designer can then set the final model order at 4 or 5 (to ensure numerical stability and convergence).

2.5 Summary

An overview of different reduction tools and techniques is presented. Reduction techniques used in the following chapters are discussed in detail. A primary reduction technique to remove algebraic variables from DAEs, Kron reduction, is discussed. Krylov-subspace method using the Arnoldi technique is chosen as an example of the moment-matching class of reduction tools. Singular perturbation approximation and truncated balanced residualization are discussed as examples of SVD-based techniques. Quasi pole/zero cancellation and fast state elimination are shown to be complimentary methods along with SVD-based techniques. A nonlinear order-reduction framework is set forth that relies on previously stored characteristics of linear reduced-order models and their parametric representation in lookup tables.

CHAPTER 3

MAGNETIC EQUIVALENT CIRCUITS MODELING

3.1 Magnetic Modeling Overview

Accurate modeling and formulation of magnetic components that include nonlinear B-H characteristics have been investigated in the literature for a century (e.g., Jiles and Atherton [93-94], Preisach [95], Chan [96], Carpenter [97], Hodgdon [98], Wilson [99]). Magnetic component modeling usually deals with loss characterization based on the Steinmetz equation (or its extension) [100]. It is parameterized empirically [101-102] or formulated analytically [103-106] as a function of flux density magnitude/frequency and magnetic materials characteristics. However, loss characterization is a static phenomenon which is only valid for low single-frequency excitation signals [101-102, 104-111]. Alternatively, the approach set forth in this chapter provides accurate and rapid-to-simulate dynamic models for system-level transient studies.

Dynamic modeling of magnetic components represents a special challenge, as the results should be accurate over a wide range of operating conditions and frequencies. They are usually represented by behavioral models based on often unreliable approximations. Physics-based models, such as finite-element models (FEM), are based on established principles (e.g., Maxwell equations) and are considered to be fundamentally reliable. FEM-based approaches are highly accurate and, therefore, desirable for design verification and analysis purposes. Boundary-based methods, that mainly concentrate on exterior regions of electromechanical systems (e.g., air gap), are used alone (Schwarz-Christoffel (SC) [112-113]) or along with FEM (Hybrid [13]) to expedite accurate steady-state characterizations of electrical machines. In particular, SC

transformations and the SC toolbox in MATLAB are used to solve boundary-value problems in two-dimensional linear magnetic materials [112-114]. Various hardware platforms, e.g., graphic processor units [115], are investigated for boundary element methods.

The eddy current is automatically included in dynamic FEM. However, FEM models are not intuitive and do not facilitate design. Including system nonlinearity (e.g., saturation) and geometrical complexity (e.g., laminations and 3-D effects) substantially complicates model formulation. Optimization routines of magnetic components can require on the order of 10^6 solutions [116], [117]. Although significant work has been done on meshing and sparse matrix algebra [118-120], FEM tools are unlikely to be used in an iterative design framework. Rather, due to their high reliability, they are more suitable for design verification and analysis. Order reduction of FEM with relative motion will be considered in Chapter 4.

Magnetic equivalent circuits (MECs) are more intuitive while remaining based on physics [121-124]. MEC models are easily parameterized and allow for a fast parameter sweep, which is ideal for iterative design optimizations. They include local saturation effects and require fewer computational resources as compared to lumped-parameter models and FEM, respectively. The extension to 3-D cases is straightforward as MEC uses tube elements rather than point elements in FEM. An interested reader can find an excellent comparison between FEM and MEC in [125] (and references within it) with special emphasis on saturation and iron losses. MEC models are growing as an alternative design tool to lumped-parameter models and FEM for modeling and simulation of electrical machines [126-127], e.g., induction machines [125-126, 128-135], hysteresis synchronous motors [136], switched-reluctance machines [137], and brushless motors [138].

Crude geometrical simplifications often degrade the accuracy of the final MEC model. Significant analysis of leakage and fringing permeances is required to make the MEC models achieve a level of accuracy comparable to that of the FEM approach for an EI core [116]. Hybrid methods use the computational efficiency and model accuracy of MEC and FEM [139-141]. MEC parameters are refined using FEM solutions [142]. MEC models can be improved by introducing more reluctance terms in the air gap [143]. For example, a denser grid and, subsequently, a larger reluctance network are implemented in [126, 128-129, 135]. MEC models with relative motion are refined to include leakage and fringing effects [144]. However, MEC models normally omit a precise consideration of eddy currents. Eddy currents are not easily accommodated as magneto-motive force (MMF) formulation is a scalar magnetic potential problem without the geometric properties necessary to induce eddy currents [125]. In general, static MEC models are only valid for low-frequency excitations, as they assume the magnetic field penetrates the core completely.

Accurate dynamic models for solid powdered iron or laminated steel cores [145-146] require the inclusion of eddy currents. In conductive magnetic materials, such as laminated steel, change in the magnetic field induces eddy currents that oppose the change, so the MMF is not uniform within the core cross section. The flux distribution changes as the excitation frequency increases (skin effect). Thus, both the effective equivalent inductance, representing the magnetic path, and the equivalent resistance, representing the eddy currents path, are frequency-dependent [147]. “Foster” or dual “Cauer” equivalent circuits are proposed for eddy-currents and skin effects in transformer winding [147-149] and magnetic cores [99, 150-156]. Using a continued fraction expansion, a standard Cauer equivalent circuit can be derived from the original Foster equivalent circuit [147]. The challenge is accurate representation of the magnetic core using “Cauer”

models. Linear, static parameter models fail to reproduce the actual material behavior over a large range of input frequency and excitation levels without resorting to adaptively re-tuning the Cauer model parameters [157]. The accuracy of the final Cauer model depends on the number of terms retained in a partial fraction expansion, which determines the number of circuit stages. However, the large number of subcircuit stages introduces hundreds to thousands of state variables, often with very fast dynamic modes that are not physically meaningful. The physics-based models (either FEM or MEC), despite their high accuracy, then, are computationally expensive, memory-consuming, and vulnerable to numerical instability.

Model order-reduction techniques are considered to reduce the number of equations and achieve a computationally tractable model. Low-order dynamic magnetic models are mainly behavioral models that are parameterized from post-processing of FEM simulations (2^{nd} order RLC equivalent models [158], bond graph [132], lumped parameters [159]). Empirical eigenvectors are used to reduce the nonlinear FEM toroidal core model [160]. This requires extensive time-domain excitation/training and computationally sensitive singular-value decomposition and eigenvector extraction from the covariance matrix. Proper orthogonal decomposition reduces the model order in low-frequency hysteresis [161]. Chapman has provided some insight into FEM-based order-reduction techniques for 2-D, single-lamination stationary magnetic components (e.g., linear [162-163], saturated [164-166], multiple-winding [167], and hysteresis cases [168]). However, to the best of our knowledge, neither a high-fidelity MEC model nor its reduced-order model has been developed.

In this chapter, we first try to provide an accurate dynamic model of magnetic systems, and then develop linear and nonlinear order-reduction frameworks. This methodology is then extended to systems with linear motion and multiple winding systems. In all cases, the magnetic

component is modeled as a subsystem with voltage as the input variable and current as the output variable. This is to implement dynamic equations in an integral form and avoid the numerical noise associated with differentiation.

3.2 High-fidelity Dynamic Magnetic Equivalent Circuits

A simple representation of an MEC model is shown in Fig. 3.1(a). Two approaches to MEC are nodal-based methods that use magnetic scalar potentials as unknowns, and mesh-based approaches that use magnetic flux. Although identical in the linear magnetic region, nodal-based approaches are shown to have ill-conditioned matrices in saturated regions [127]. Thus, mesh-based approaches are considered here. The interaction between the electric and magnetic domains is facilitated by a magneto-electric differential gyrator [123]. Electromagnetic curl equations of Maxwell's equations can be reduced to equivalent electric circuits

$$\begin{cases} \nabla \times E = -\dfrac{\partial B}{\partial t} & \Rightarrow \quad v = ri + L\dfrac{\partial i}{\partial t} \\ \nabla \times H = J & \Rightarrow \quad F = \Phi R(\Phi) \end{cases} \tag{3.1}$$

where F, R, and ϕ represent magneto-motive force, magnetic reluctance, and magnetic flux, respectively. Using a stacking factor, laminated cores are usually treated as a single bulk core [126]. We consider individual laminations as parallel magnetic cores in order to effectively capture the actual eddy-current path (Fig. 3.1(b)).

In the presence of eddy currents, the magnetic core is divided into a few concentric zones, each carrying flux perpendicular to the zone and behaving as a current sheet circulating around the cross section (Fig. 3.1(c)) [99], [150-154]. Each zone is modeled as a magnetic-domain *R-L* pair (Fig. 3.1(d)), where R_k represents the k^{th} zone flux path reluctance, and transference G_k

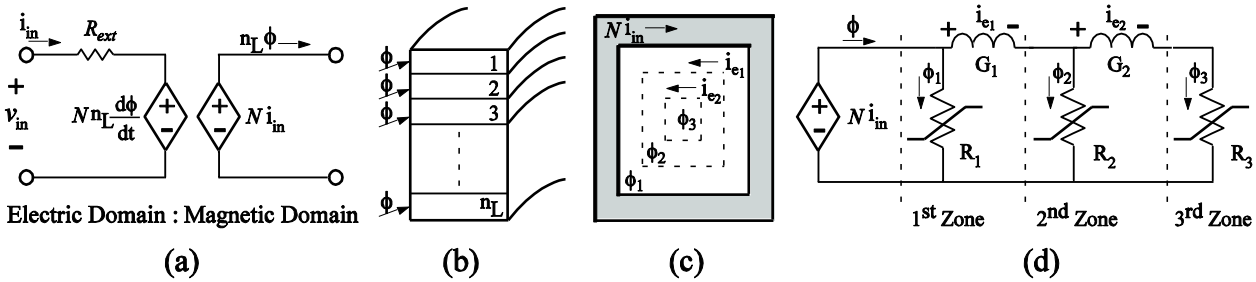

Fig. 3.1 MEC model of a laminated structure: (a) Coupled electric-magnetic domain circuits; (b) Laminated magnetic core; (c) Single-lamination representation with opposing eddy currents in each magnetic zone; (d) Equivalent magnetic *R-L* ladder structure with (possibly) nonlinear reluctances.

accounts for the conductivity of the k^{th} zone eddy-current path. The reluctance terms could be nonlinear functions of corresponding fluxes to represent possible saturation.

In available models with few magnetic zones, the mutual interaction between the eddy current, i_{e_k}, and the magnetic flux, ϕ_k, is neglected [150-154]. This implies a uniform flux density B_k in each magnetic zone. This simplification is justifiable when the segmentation thickness, Δ_k, is less than the magnetic skin depth

$$\Delta_k \le \delta = \sqrt{\frac{1}{\sigma \mu_o \mu_r \pi f}} \tag{3.2}$$

Thus, available models with few magnetic zones are not suitable for PWM excitation waveforms with rich high-frequency content, commonly used in motor drives [145]. Moreover, MEC models are based on the assumption that the magnetic flux should not cross the permeance tube walls and should be distributed homogeneously in the tube cross section. This is not satisfied by a single permeance in true 3-D cores, as the flux lines are not uniformly distributed and have sharp gradients [143].

A high-fidelity magnetic equivalent circuit (HFMEC) is considered as a modular assembly of flux-tube building blocks. These flux tubes (Fig. 3.2(a)) form concentric magnetic zones (Fig.

3.2(b)), which in turn form the final reluctance networks for each lamination. The resulting reluctance network of a laminated magnetic structure is shown in Fig. 3.2(c). As the laminated plates are in parallel, a single lamination is discussed first. The magnetic core cross section is considered as a dense uniform grid (Fig. 3.3(a)) that effectively captures corner effects and can be extended outwardly to include external leakage and fringing effects. Grid thickness is defined by considering magnetic skin depth δ based on material characteristics and desired model bandwidth. Magnetic flux density in each element is now safely assumed to be uniform. Flux tubes are equal in area, but their depth into the third dimension varies based on the core geometry. As an example, the reluctance and transference formulations are shown in (3.3) and (3.4) for a toroidal core; μ_r is the relative permeability, σ is the electrical conductivity, N_z is the number of magnetic zones, r_{in} and r_{out} are the inner and outer radii, respectively, and d_x and d_y are the flux tube's lengths in *x* and *y* directions, respectively.

Each magnetic zone is the combination of several associated flux tubes, where the number of associated flux tubes decreases from the outside zone to the center. As an example, the second zone and its associated flux tubes are shown as black in Fig. 3.3(a). The k^{th} zone overall reluctance is calculated as the parallel combination of its associated flux-tube reluctances. The time-varying fluxes in the zones enclosed by that k^{th} zone cause the eddy current, i_{e_k}. This eddy current passes through a series combination of flux-tube electrical resistances. Alternatively, the equivalent magnetic-domain inductance of each zone is the parallel combination of associated flux-tube electrical conductances. The final magnetic *R-L* ladder structure is shown in Fig. 3.3 (b). The equivalent circuit is extracted via a parallel combination of *R*'s and *G*'s associated with each magnetic zone. This results in a large set of ODEs, (3.5), with v_{in} as the input variable, i_{in} as the output variable, and ϕ_k as the state variables.

$$\begin{cases} \Re_k = \dfrac{1}{\mu_0\mu_r d_x d_y \left(\dfrac{2(N_z-k)+1}{2\pi\left(r_{in} - d_x/2 + kd_x\right)} + \dfrac{2(N_z-k)+1}{2\pi\left(r_{out} + d_x/2 - kd_x\right)} \right) + \sum_{j=1}^{2(N_z-k)-1} \dfrac{\mu_0\mu_r d_x d_y}{\pi\left(r_{in} - d_x/2 + (k+j)d_x\right)}} & k = 1 \cdots N_z - 1 \\ \Re_{N_z} = \dfrac{\pi(r_{in}+r_{out})}{\mu_0\mu_r d_x d_y} \end{cases} \tag{3.3}$$

$$\begin{cases} G_k = \dfrac{1}{\dfrac{d_y(2(N_z-k)+1)}{2\pi\alpha d_x}\left(\dfrac{1}{r_{in} - d_x/2 + kd_x} + \dfrac{1}{r_{out} + d_x/2 - kd_x} \right) + \sum_{j=1}^{2(N_z-k)-1} \dfrac{d_x}{\pi\alpha d_y\left(r_{in} - d_x/2 + (k+j)d_x\right)}} & k = 1 \cdots N_z - 1 \\ G_{N_z} = arbitrary \end{cases} \tag{3.4}$$

$$\begin{cases} \dfrac{d}{dt}\Phi = \mathbf{A}\Phi + \mathbf{b}v_{in} \quad \Phi = [\phi_1 \cdots \phi_{N_z}]^T \\ i_{in} = \mathbf{C}\Phi + dv_{in} \end{cases} \tag{3.5}$$

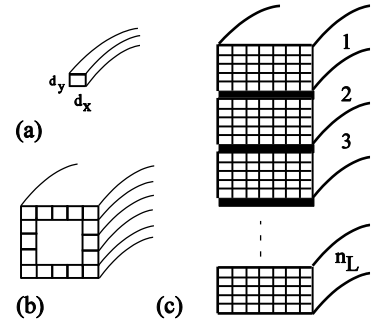

Fig. 3.2 Geometrical terminologies for the proposed HFMEC system: (a) A single flux tube element; (b) A magnetic zone and corresponding flux tubes; (c) Laminated magnetic structure with insulations and flux tubes.

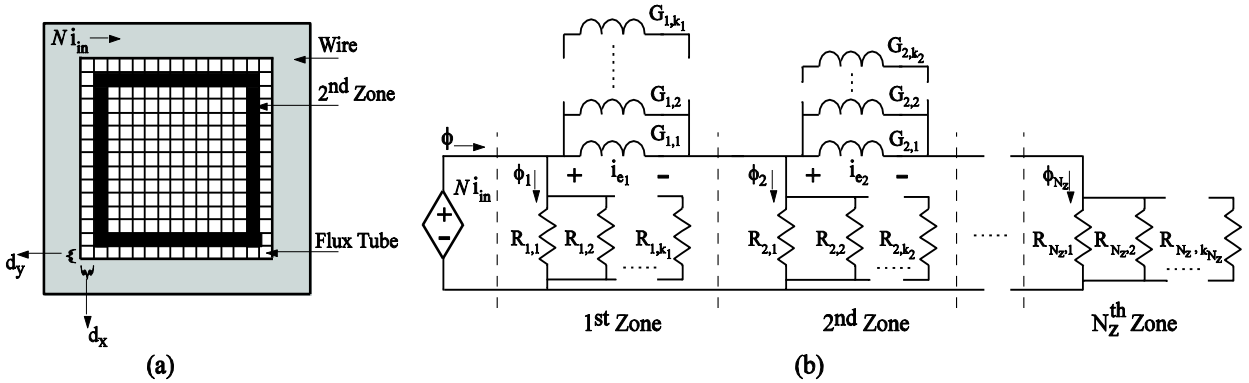

Fig. 3.3 Detailed 3-D MEC model including eddy current: (a) Detailed core cross-section meshing and associated flux tubes; (b) Equivalent magnetic *R-L* structure made of reluctances and transferences.

3.3 Linear Order-reduction in HFMEC

A hybrid linear order-reduction technique from Chapter 2, quasi pole/zero cancellation and the subsequent balanced residual method, is used. To verify the proposed linear high- and low-order HFMEC models, a T400-26 powdered-iron toroidal core, commonly used in PWM dc-dc converters, with parameters summarized in Appendix A.1, is considered here. The core input impedance is measured over a wide range of frequencies and is shown in Fig. 3.4, along with the input impedance extracted from the full-order HFMEC model. As expected, at very high frequencies, the effects of the eddy-current losses become significant. This is especially evident in the phase plot. As seen in Fig. 3.4, the full 400^{th} order model correctly represents the dynamics of the underlying hardware prototype. The proposed HFMEC is compared with a 2-D FEM model presented in [163]. As see in Fig. 3.5, the proposed model is more accurate, especially at higher frequency where the effects of eddy current are more pronounced. This can be attributed to the inherent 2-D approximations involved in the FEM model of [163]. On the other side, the FEM more accurately models wire-by-wire representation of the winding than does the lumped representation used in HFMEC. This comes at the cost of 822 state variables in FEM compared to 400 state variables in HFMEC. A 3-D FEM model with wire-by-wire representation of winding structures will be computationally prohibitive (due to the significant increase in the number of elements required), and numerically unstable (due to the mesh generation process, grid details, and round-off errors frequently encountered in FEM models). Once the HFMEC model is verified with hardware measurements and compared to the FEM model, quasi pole/zero cancellation followed by the balanced residual method is implemented.

When considering the input-impedance transfer function of the inductor core, a large number of closely spaced poles and zeros is observed (Fig. 3.6). The quasi pole/zero cancellation with

10% tolerance is applied. The resulting model is of order 10, while keeping close agreement with the original full-order model (Fig. 3.7). To further reduce the model order from 10 to 2, balanced truncation is used (Fig. 3.8). The condition number of the system matrix is improved from 4.88×10^{10} in the original full-order model to 6.22×10^{4} in the final reduced-order model. This greatly improves the simulation stability.

The model order is further reduced from 2 to 1 using balanced residualization. As seen in Fig. 3.9, this extra level of reduction jeopardizes model accuracy in the desired frequency range (2 MHz). Thus, the choice of 2nd-order model as the final reduced model is justified. If model fidelity in a higher frequency range is desired, then of course higher-order models can be used.

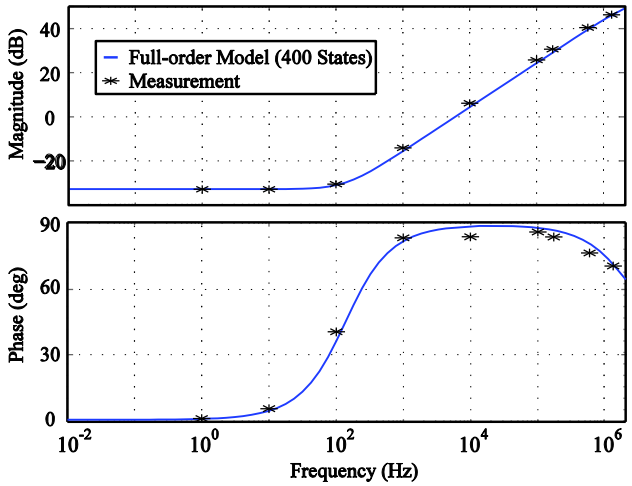

Fig. 3.4 Input impedance characterization of example inductor predicted both by the full-order model and hardware measurements.

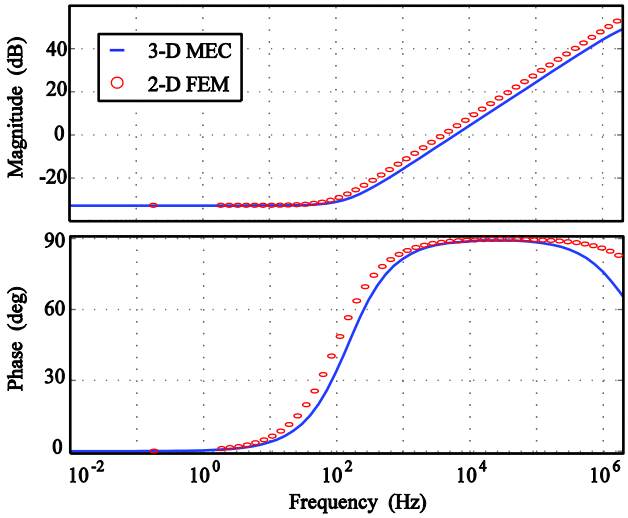

Fig. 3.5 Input impedance characterization of the example inductor predicted by the proposed HFMEC model and the 2-D FEM in [163].

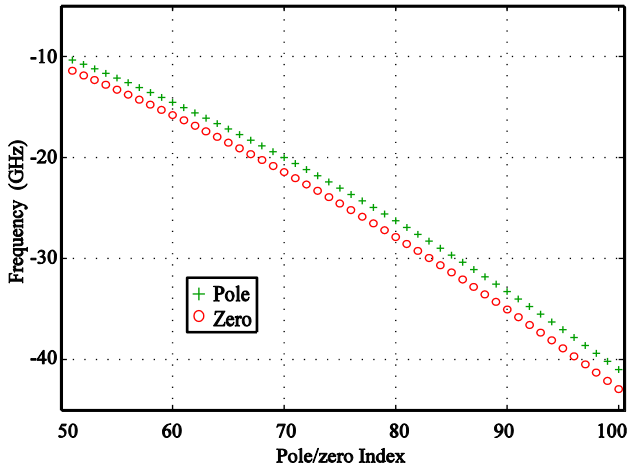

Fig. 3.6 Zoomed-in representation of selected pole/zeros of the full-order model.

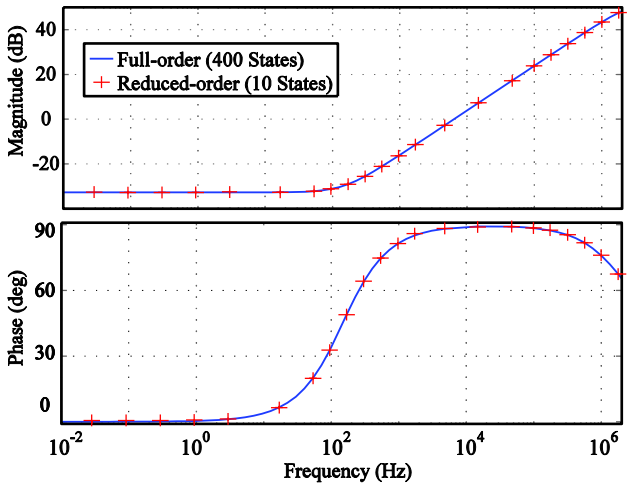

Fig. 3.7 Input-impedance characterization of original full-order model and resulting reduced-order model by quasi pole/zero cancellation.

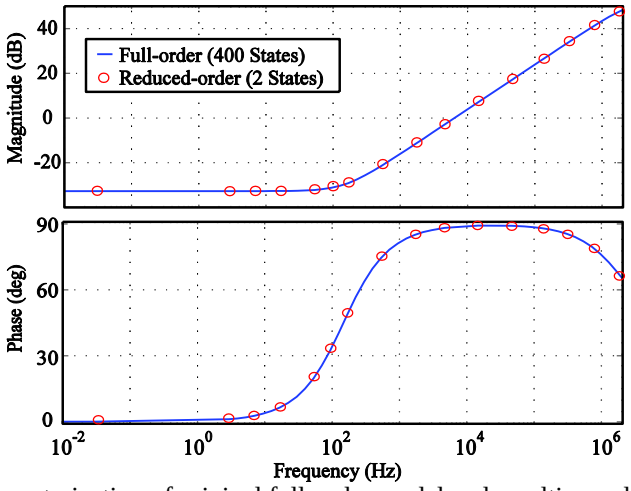

Fig. 3.8 Input-impedance characterization of original full-order model and resulting reduced-order model by quasi pole/zero cancellation and subsequent balanced residualization method.

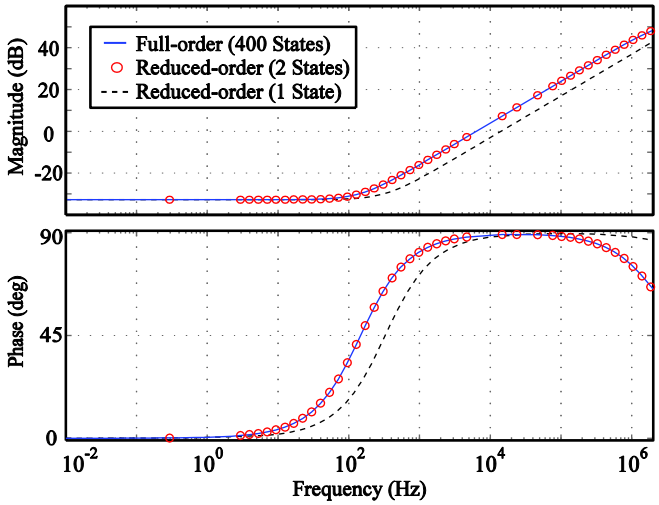

Fig. 3.9 Input-impedance characterization of original full-order model and resulting 2nd and 1st -order models.

The resulting low-order system can be transformed to a behavioral model suitable for system-level simulation. The impedance transfer function of the resulting 2nd-order model is

$$\frac{v_{in}(s)}{i_{in}(s)} = k\frac{(s+z_1)(s++z_2)}{(s+p_1)(s++p_2)} = 2556.13\frac{(s+924.7)(s+5.78\times10^7)}{(s+3.32\times10^8)(s+1.79\times10^7)} \tag{3.6}$$

As an example of a behavioral model, a 2nd-order lumped-parameter equivalent circuit is shown in Fig. 3.10. The overall impedance transfer-function extracted from Fig. 3.10 is

$$\frac{v_{in}(s)}{i_{in}(s)} = \frac{(r_C LC_L + r_s LC_L)s^2 + (r_L r_C C_L + L + r_s r_C C_L + r_s r_L C_L)s + r_L + r_s}{LC_L s^2 + (r_C C_L + r_L C_L)s + 1} \tag{3.7}$$

Fitting the equivalent circuit impedance of Fig. 3.10 to the transfer function of (3.7) leads to a set of nonlinear equations

$$\begin{cases} LC_L = \dfrac{1}{p_1 p_2} \\ r_C C_L + r_L C_L = \dfrac{p_1 + p_2}{p_1 p_2} \\ r_s + r_L = k\dfrac{z_1 z_2}{p_1 p_2} \\ r_C LC_L + r_s LC_L = \dfrac{k}{p_1 p_2} \\ r_C r_L C_L + r_s r_L C_L + r_s r_C C_L + L = k\dfrac{(z_1 + z_2)}{p_1 p_2} \end{cases} \tag{3.8}$$

which can be iteratively solved to find the circuit parameters in Fig. 3.10

$$r_s = 7.7\ \text{m}\Omega, \quad r_L = 15.3\ \text{m}\Omega, \quad r_C = 2.55\ \text{k}\Omega, \quad \text{L} = 24.85\ \mu\text{H}, \quad \text{C}_\text{L} = 241\ \text{pF} \tag{3.9}$$

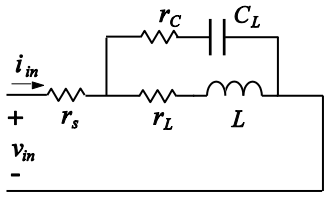

Fig. 3.10. An equivalent lumped-parameter inductor model.

3.4 Order-reduction in HFMEC with Saturation

The proposed HFMEC is a nonlinear system when saturation is considered in reluctance formulation in (3.1), and resulting permeabilities are a nonlinear function of the flux $(\mu_k(\phi_k))$. This will modify the HFMEC LTI system of equations to a nonlinear set of equations

$$\begin{cases} \dfrac{d}{dt}\Phi = \mathbf{A}(\Phi)\Phi + \mathbf{b}v_{in} \quad \Phi = [\phi_1 \cdots \phi_{N_Z}]^T \\ i_{in} = \mathbf{C}(\Phi)\Phi + dv_{in} \end{cases} \tag{3.10}$$

In order to use piecewise-linear reduction techniques established in Chapter 2, one may linearize the system in (3.10) at several steady-state points or along an excited trajectory. In stationary magnetic systems with fixed-coil windings distribution, the magnetic flux distribution and resulting effective permeability are determined by the input current level in steady state. It is shown in [165] that the magnetic vector potentials of the static Maxwell's equations can be determined solely by the dc input current. The resulting magnetic vector potentials are used to determine the flux density and, therefore, the effective permeabilities. A similar approach is taken to determine the effective permeabilities in the HFMEC circuit corresponding to a dc input current level in steady state. The flux derivatives, and therefore the eddy currents, are zero in the steady state associated with the dc current excitation. As shown in Fig. 3.2(b), the eddy currents are the MMF drops over the transferences (magnetic inductances) in the magnetic domain circuit. Therefore, zero eddy current implies a zero MMF drop over magnetic inductances. This simplifies the *R*-*L* ladder structure of the magnetic domain circuit to a parallel combination of the nonlinear reluctances (Fig. 3.11), from which corresponding permeability and reluctance terms are iteratively extracted. In particular, using the magnetic-domain circuit in Fig. 3.11, one may solve the nonlinear equations

$$NI_{in}^{ss} = \Phi_{i,j}\Re_{i,j} \qquad i = 1\cdots N_z,\ j = 1\cdots k_n \tag{3.11}$$

where N is the number of winding turns, I_{in}^{ss} is the given dc input current magnitude, N_z is the number of magnetic zones, and k_n is the number of flux tubes in the n^{th} magnetic zone. The saturated nonlinear model is linearized around the steady state associated with a given input current I_{in}^{ss}. Thus, the small-signal parameters corresponding to different values of input dc currents are extracted and used to form appropriate transfer functions (dynamic impedance and/or admittance). Now, any linear reduction process introduced in Chapter 2 can be applied to

reduce the model order. It should be noted that the steady-state points are only used for model extraction, whereas the resulting final model is dynamic.

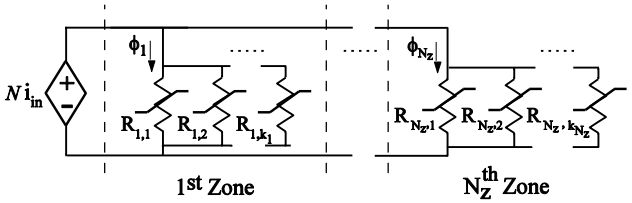

Fig. 3.11 Magnetic-domain circuit in steady state.

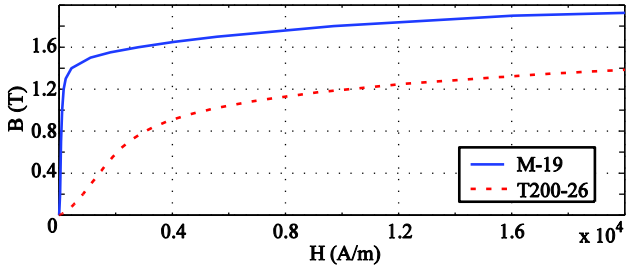

Fig. 3.12 Nonlinear magnetic charactersitics, B-H curve, for powdered iron [169] and laminated steel cores [170] considered.

The nonlinear magnetic characteristics, B-H curves, for the two considered cases here, T200-26 powdered iron and M-19 laminated steel, are shown in Fig. 3.12. The geometrical data of toroidal cores for both powdered iron and laminated steel are given in Appendix A.1. The input admittance of the laminated steel core is extracted over a wide range of frequencies corresponding to the unsaturated $(i_{in} = 0)$ and saturated $(i_{in} = 5)$ cases. Linear order-reduction techniques reduce the model order from 300 to 3. The results are overlaid in Fig. 3.13, where an excellent match between corresponding reduced- and full-order models is observed. The condition number of the system matrix is greatly improved from 1.28×10^{11} and 4.17×10^{10} in the full-order models, to 3×10^{4} and 2.96×10^{4} in the reduced-order models, for unsaturated and saturated cases, respectively. This greatly simplifies model execution for transient simulations. A similar process is done for powdered iron cores.

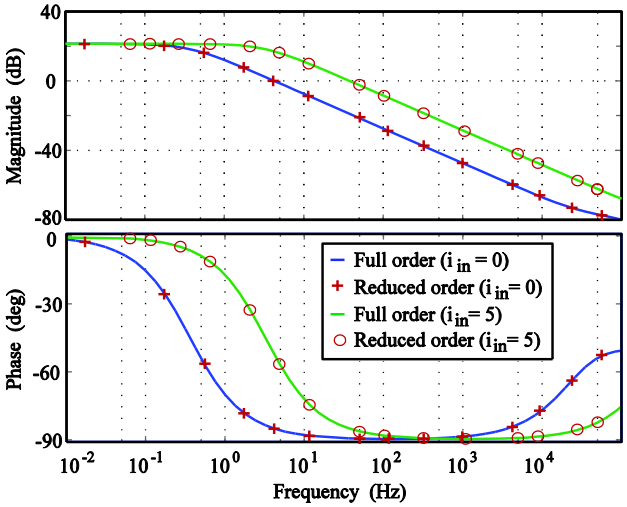

Fig. 3.13 Full- and reduced-order transfer functions for different current magnitudes: unsaturated $(i=0)$ and saturated laminated steel $(i=5)$.

The transfer-function extraction and order-reduction are implemented in an automated loop. The resulting gains, poles, and zeros are saved as numerical functions of the input current magnitude. For a T200-26 powdered iron core, the gain, poles, and zeros of the reduced-order model transfer function are plotted in Fig. 3.14, as functions of the input current magnitude. These data are re-organized and stored as lookup tables with appropriate interpolation. Then, the nonlinear order-reduction method is implemented, as shown in Fig 3.15. For a given input current value, i_{in}, the corresponding gain, poles, and zeros are extracted from previously developed lookup tables to form a transfer function valid for the vicinity of i_{in}

$$\frac{i_{in}(s)}{v_{in}(s)} = \prod_{j=1}^{n} K(i_{in}) \frac{(s - z_j(i_{in}))}{(s - p_j(i_{in}))} \tag{3.12}$$

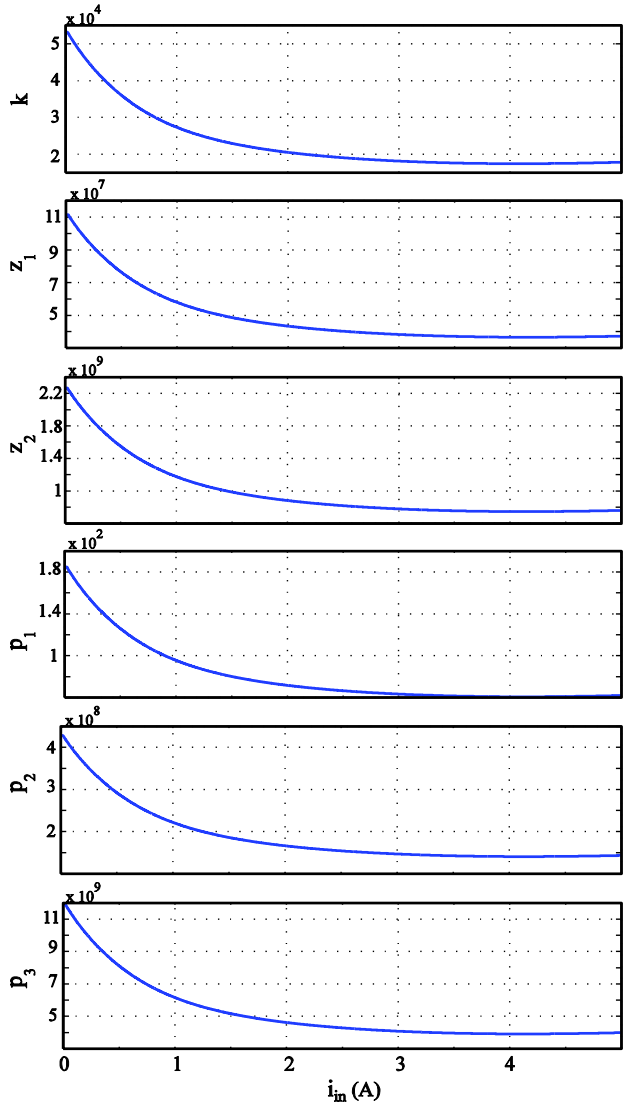

Fig. 3.14 Gain, zeros, and poles as functions of input currents for the reduced-order model of the T200-26 powdered iron core considered here.

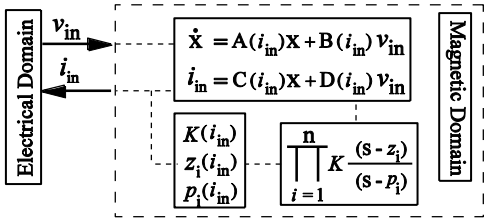

Fig. 3.15 Implementation of the nonlinear order-reduction framework.

It should be noted that the resulting systems (3.12) are used to approximate the original nonlinear system within a corresponding current region, instead of the entire state-space region. This greatly simplifies the weighting procedure. As opposed to the computationally intensive and numerically sensitive time-domain training procedure involved in the conventional Krylov-subspace methods [164], numerical transfer function extraction is a rapid and almost instantaneous procedure. Also, as the steady-state solutions are used to extract the linear models, instead of state variables populated along a training trajectory, the resulting model is not limited by a training input voltage. Moreover, the higher currents can be accommodated by assuming that the model extracted for the highly saturated current, $I_{in}^{ss,sat}$, is valid for $\left[I_{in}^{ss,sat},\infty\right)$. This is a reasonable assumption; a magnetic system behaves almost linearly when it is highly saturated.

To verify the original full-order model (300 states) and the resulting reduced-order model (3 states), a sinusoidal input voltage $\left(v_{in}=7.5\sin(120\pi t)\right)$ is applied to a toroidal core consisting of stack of a 50 laminations of M-19 steel. The hardware measurement results are shown in Fig. 3.16(a), where the current waveform clearly indicates saturation. The proposed full-order HFMEC model accurately portrays the system dynamics, as seen in Fig. 3.16(b). The proposed reduced-order model accurately reproduces the input currents predicted by the hardware measurement and the full-order model, as shown in Fig. 3.16(c).

Next, to verify the proposed nonlinear reduction methodology under the nonsinusoidal excitation, a PWM input voltage, with 10 V amplitude and 500 Hz frequency, is applied to the T200-26 powdered iron core. As shown in Fig. 3.17(a) and (b), the input current of the proposed nonlinear HFMEC model and the measured current show an acceptable match. The difference can be attributed to the absence of magnetic hysteresis in the proposed model. Moreover, as the study demonstrates, the input current waveform resulting from the reduced-order model (Fig.

3.17(c)) closely resembles that obtained from the full-order model (Fig. 3.17(b)), which verifies the reduction procedure.

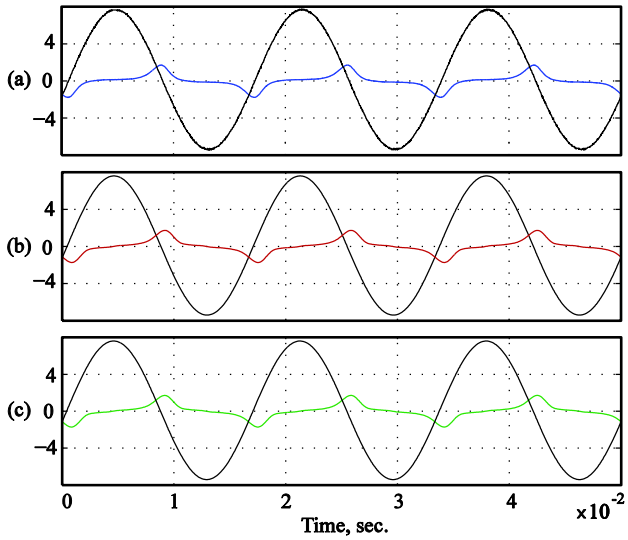

Fig. 3.16 Sinusoidal input voltage and resulting current waveforms: (a) Hardware measurement; (b) Full-order HFMEC with 300 state variables; (c) Reduced-order HFMEC with only 3 state variables.

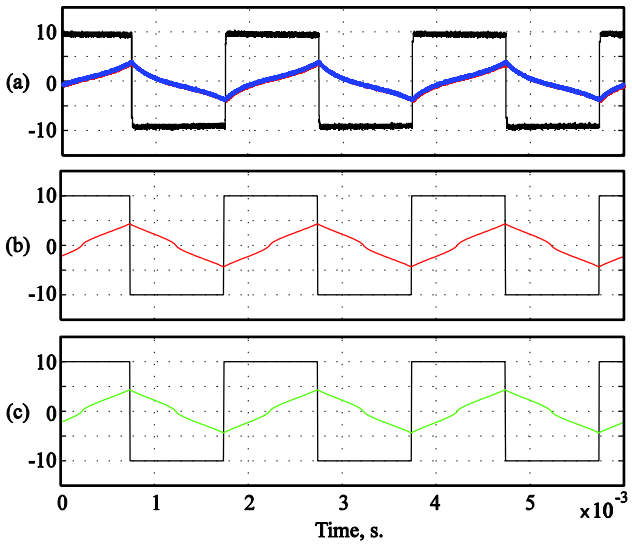

Fig. 3.17 PWM input voltage and resulting current waveforms: (a) Hardware measurement; (b) Full-order HFMEC with 300 state variables; (c) Reduced-order HFMEC with only 3 state variables.

3.5 Order-reduction in HFMEC with Relative Motion

Dynamic simulation of time-variant magnetic systems, e.g., magnetic systems with relative motion, is considerably more complex. Available reduced-order models are model specific [159]. A physics-based phase variable model of PM synchronous machines is developed to utilize an FE model and HIL real-time simulation [171]. The developed model uses tables that are obtained as a post-process of FE calculations over a complete ac cycle, to describe the variation of inductances with the rotor position and armature currents. A simpler, more efficient physics-based approach based on the HFMEC model is considered.

3.5.1 Model formulation

A simple representation of a plunger is shown in Fig. 3.18(a). This plunger consists of a stationary and a moving U93/76/30 (Ferroxcube Inc. [172]) core. Material parameters and specifications are summarized in Appendix A.2. Mechanical and magnetic domains are coupled by incorporating relative motion in position-dependent air-gap and fringing reluctances. The interaction of the electric and mechanical domains is accounted for by the induced voltage term (back EMF) in the electric domain. Similarly to Section 3.2, a dense grid is imposed on the magnetic core cross section (Fig. 3.18(b)), where the second magnetic zone is shown in black. In the presence of eddy currents in dynamic MEC models, each magnetic zone is modeled as a magnetic-domain R-L pair (Fig. 3.18(c)). Magnetic-domain R_k represents the k^{th} zone flux-path reluctance, and transference G_k accounts for the conductivity of the k^{th} zone eddy-current path. The corresponding reluctance and transference terms are formulated in (3.13) and (3.14), respectively, based on the geometrical and material data.

$$\begin{cases} \Re_k = \dfrac{1}{\mu_0\mu_r d_x d_y \left(\dfrac{\left(2\left(N_z-k\right)+1\right)}{\left(r_{in}+\left(k-0.5\right)d_z\right)} + \dfrac{\left(2\left(N_z-k\right)+1\right)}{\left(r_{out}+\left(0.5-k\right)d_z\right)} + \sum_{i=1}^{2(N_z-k)-1} \dfrac{2}{\left(r_{in}+\left(k+i-0.5\right)d_z\right)} \right)} & k=1\cdots N_z-1 \\ \Re_{N_z} = \dfrac{\left(r_{in}+r_{out}\right)}{2\mu_0\mu_r d_x d_y} \end{cases} \tag{3.13}$$

$$\begin{cases} G_k = \dfrac{1}{\dfrac{d_y\left(2\left(N_z-k\right)+1\right)}{\delta d_x}\left(\dfrac{1}{r_{in}+\left(k-0.5\right)d_z} + \dfrac{1}{r_{out}+(0.5-k)d_z} \right) + \sum_{i=1}^{2(N_z-k)-1} \dfrac{2d_x}{\delta d_y\left(r_{in}+\left(k+i-0.5\right)d_z\right)}} & k=1\cdots N_z-1 \\ G_{N_z} = arbitary \end{cases} \tag{3.14}$$

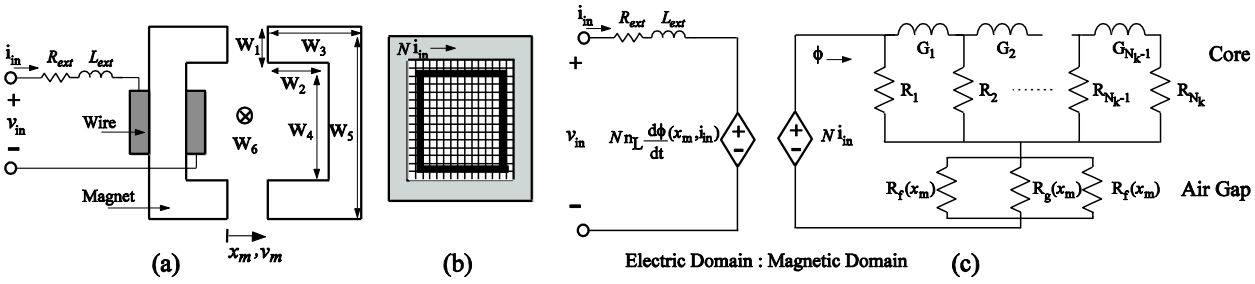

Fig. 3.18. Detailed MEC representation of an actuator: (a) Actuator with stationary and moving legs; (b) Detailed core cross-section meshing and associated flux tubes; (c) Position-dependent MEC model with a long R-L ladder structure, back EMF and fringing.

The full-order HFMEC model is constructed according to the methodology proposed in Section 3.2. It should be noted that the mechanical position is considered as a state variable in model formulation in order to facilitate the back EMF representation in the electric domain (Fig. 3.18(c)). The mechanical equations provide the moving leg location, taking into account the possible positional constraints (damper, spring, etc.). The position-dependent air-gap and fringing reluctances are given (3.15). The magnetic flux is not confined to the core area and an equivalent air gap is considered. Fringing effects are incorporated, as shown in Fig. 3.18(c), by considering the spatial relationship between the air-gap distance, x_m, and the core geometry

$$\begin{cases} R_g(x_m) = \dfrac{2x_m}{\mu_o w_1 w_6} \\ R_f(x_m) = \dfrac{2\pi x_m}{\mu_o w_1 w_6} \end{cases} \tag{3.15}$$

For a given position of the moving leg, x_m, the resulting HFMEC model defines a linear system. When the change in position is considered, the final model is time-varying (position and speed dependent). Using the magnetic flux and mechanical positions as state variables, **x**, input voltage as the input variable, **u**, and the input current as the output variable, *y*, the final full-order, state-space model is formulated as

$$\begin{cases} \dfrac{d\mathbf{x}}{dt} = \mathbf{A}(x_m, v_m)\mathbf{x} + \mathbf{b}(x_m, v_m)v_{in} \quad \mathbf{x} = [x_m, \phi_1 \cdots \phi_{N_Z}]^T \\ i_{in} = \mathbf{C}(x_m, v_m)\mathbf{x} + \mathbf{d}(x_m, v_m)v_{in} \end{cases}. \tag{3.16}$$

3.5.2 Order-reduction framework

A dense grid in Fig. 3.18(b) produces a large R-L ladder structure that implies a time-varying system with a large set of state variables in (3.16). However, for a fixed mechanical position and speed, the resulting state-space model is linear. Quasi pole/zero cancellation and fast state eliminations are used to reduce the model order as set forth in Chapter 2. The remaining modal equations constitute the final reduced-order model for the given mechanical position and speed.

For the position and speed range of interest, several input-admittance transfer functions are extracted numerically. This is easily implemented in an automated loop. The resulting gains, poles, and zeros are saved as numerical functions of the moving leg position and speed. These data are re-organized and stored as lookup tables with appropriate interpolation. The nonlinear order-reduction method is then represented by the block diagram shown in Fig. 3.19. For a given value of the mechanical position, x_m, and speed term, v_m, the corresponding gain, poles, and

zeros are extracted from previously developed lookup tables to form a transfer function valid for the vicinity of x_m and v_m:

$$\frac{i_{in}}{v_{im}} = \prod_{i=1}^{n} k(x_m, v_m) \frac{\{s - z_i(x_m, v_m)\}}{\{s - p_i(x_m, v_m)\}} \tag{3.17}$$

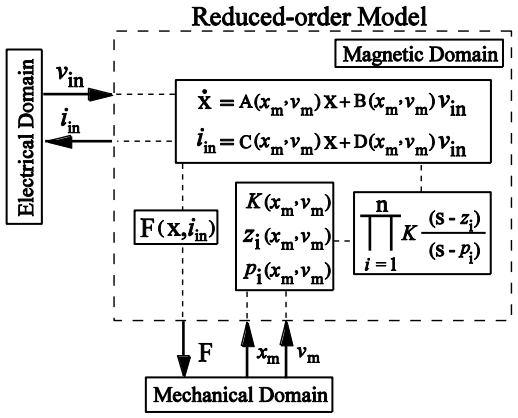

Fig. 3.19. Implementation of the proposed reduced-order model for an electromechanical system.

The model order is arbitrarily determined by *n*. The resulting transfer functions are converted to the state-space model in a controllable canonical form. For a given input voltage v_{in} and mechanical variables (x_m, v_m) at any time step, the input current, i_{in}, is obtained for the next time step of the transient simulation. The final nonlinear reduced-order model replaces the original nonlinear full-order model.

3.5.3 Model verification

The full-order MEC model of the plunger in Fig. 3.18(c) is constructed according to the state equations in (3.16). The resulting state-space model is of the order 300. The input-admittance transfer function of the actuator is attempted at several points on the movement path. As expected, eddy current losses become significant at higher frequencies and the magnetic core reveals some resistive behavior, predominantly in the phase-domain. Respective full-order

models are successfully reduced from 300 to only 5 state variables, using quasi pole-zero cancellation and fast state elimination, as explained in Chapter 2. The full- and reduced-order transfer functions for two extreme locations of the moving leg, $(x_m = 0)$ and $(x_m = 2mm)$, where the moving leg is at stop, are plotted in Fig. 3.20. Moreover, for a given position on the movement trajectory, $(x_m = 1\,\text{mm})$, and corresponding to different speed terms (accelerating $(v_m = 2\pi)$ and decelerating $(v_m = -2\pi)$), respective full- and reduced-order models are shown in Fig. 3.21. As seen in Figs. 3.20 and 3.21, excellent matches between corresponding full- and reduced-order models are reported in all cases.

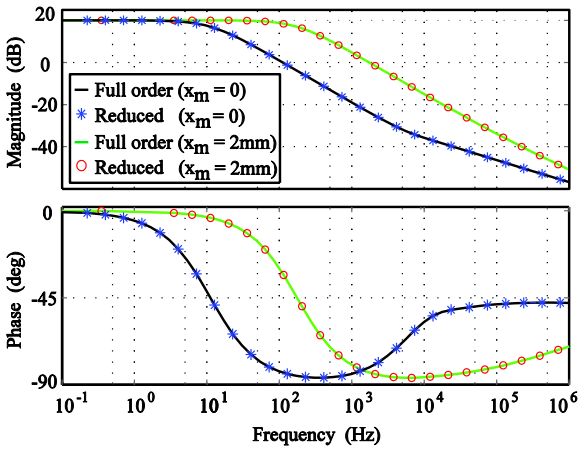

Fig. 3.20. Full- and reduced-order transfer functions for different locations $(x_m = 0)$ and $(x_m = 2\text{ mm})$ with zero speed.

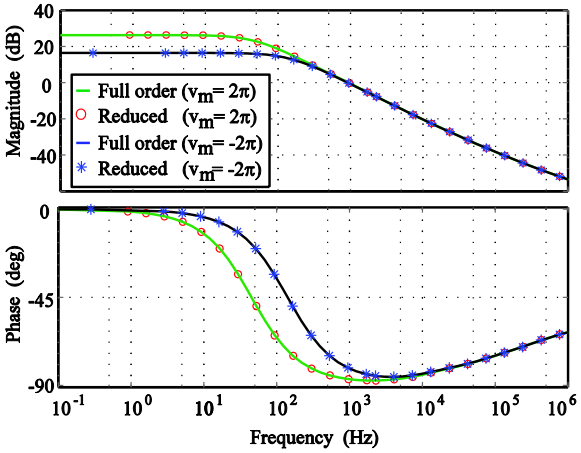

Fig. 3.21. Full- and reduced-order transfer functions for different speeds terms $(v_m = 2\pi)$ and $(v_m = -2\pi)$ corresponding to a given mechanical position $(x_m = 1\,\text{mm})$.

The nonlinear reduced-order model is constructed according to the methodology proposed in Chapter 2. A PWM input voltage and a sinusoidal varying mechanical position are considered, although the methodology is general and not restricted to any particular excitation/movement trajectory. As the moving leg leaves the stationary leg, the dominant air-gap reluctance is increased. This reduces the equivalent inductance magnitude, thereby increasing the current magnitude for a given input voltage. As seen in Fig. 3.22, the proposed reduced-order model accurately reproduces the input current predicted by the full-order model, while significantly reducing the model order and computational intensity.

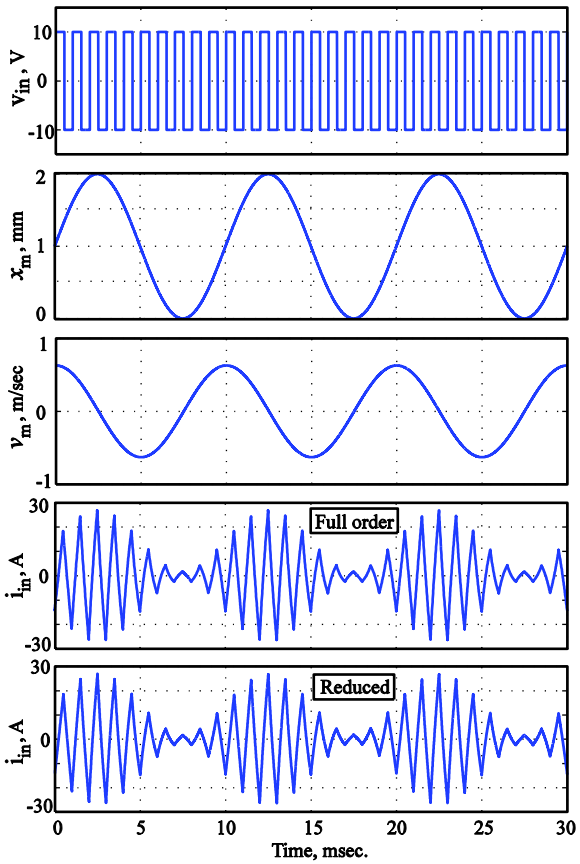

Fig. 3.22. Input voltage, mechanical position, mechanical speed, and resulting input current for full- and reduced-order models (300 and 5 state variables, respectively).

3.6 Order-reduction in HFMEC with Multiple Windings

Magnetic components in power and energy systems, e.g., transformers, almost always are multi-port magnetic systems with multiple windings. Early reduced-order modeling efforts in [173] apply Kron reduction on the detailed lumped-parameter model of a utility-scale transformer. This is not a first-principle design approach, as the fundamental laws of physics are not followed and the transformer model is linear and lossless. In [174], the higher-order model of the transformer winding structure is considered. Then, several series-connected turns are lumped to structurally reduce the model order. The magnetic core does not consider the eddy current dynamics or magnetic nonlinearity, and the structural reduction is not mathematically rigorous. High-order transformer models conventionally focus on the high-frequency effects in transformer windings (e.g., proximity, skin , and capacitive effects [175]). A very high frequency transformer FEM model in [176] includes individual representations of winding turns and corresponding turn-to-turn capacitances. The resulting multi-conductor transmission line model is later reduced using moment-matching methods. Likewise, in [177], the high-frequency distributed capacitive effects between coil insulations are expressed as an extended-π-equivalent transmission-line model. This model is later reduced by the compensated truncation of balanced realizations. Lumped equivalent circuits are extracted from reduced-order high-frequency transformer winding models [178]. Order-reduction of high-frequency eddy current dynamics in multiple-winding systems has received little attention.

3.6.1 Model formulation

An example of multiple-winding systems with w sets of windings is considered in Fig. 3.23(a). The external resistance and inductance of the k^{th} winding are shown as $r_{ext,k}$ and $L_{ext,k}$,

respectively. In our context, the terminal voltage, v_k, and current, i_k, of the magnetic subsystems are interface variables required to integrate the magnetic subsystem in the overall electrical systems. The electric and magnetic domains are coupled though a differential gyrator (Fig. 3.23(b)). The HFEMC model of the magnetic core that includes a large R-L ladder structure is considered in the magnetic domain (Fig. 3.23(c)).

The dynamic HFMEC model of the multi-winding structure shown in Fig. 3.23(a) is extracted here. The electric-domain dynamics are sets of w differential equations associated with the external winding variables and the magneto-electric differential gyrator as

$$v_k - r_{ext,k} i_k - L_{ext,k} \frac{di_k}{dt} = p_k N_k \frac{d\Phi_1}{dt} \quad , k = 1 \cdots w \tag{3.18}$$

where w is the number of windings. Magnetic-domain dynamics are extracted from Fig. 3.23(b)

$$\begin{cases} R_{j-1}\left(\Phi_{j-1} - \Phi_j\right) - R_j\left(\Phi_j - \Phi_{j+1}\right) = G_{j-1} \dfrac{d\Phi_j}{dt} \quad , j = 2 \cdots N_z \\ R_j = R_{j,1} \left\| R_{j,2} \right\| \cdots \left\| R_{j,k_j} \right. \\ G_j = G_{j,1} \left\| G_{j,2} \right\| \cdots \left\| G_{j,k_j} \right. \end{cases} \tag{3.19}$$

Assuming evenly distributed windings to minimize the leakage inductances, the algebraic relationship relating the electric and magnetic domains, based on Fig. 3.23(b), is

$$\sum_{k=1}^{w} p_k N_k i_k = R_{1,1} \left\| R_{1,2} \right\| \cdots \left\| R_{1,k_1} \right. \times \left(\Phi_1 - \Phi_2\right) \tag{3.20}$$

Here, p_k represents the polarity and direction of the k^{th} winding voltage and current determined by the winding taps and configuration, respectively. From (3.18)-(3.20), one may drive the standard state equations of the overall system:

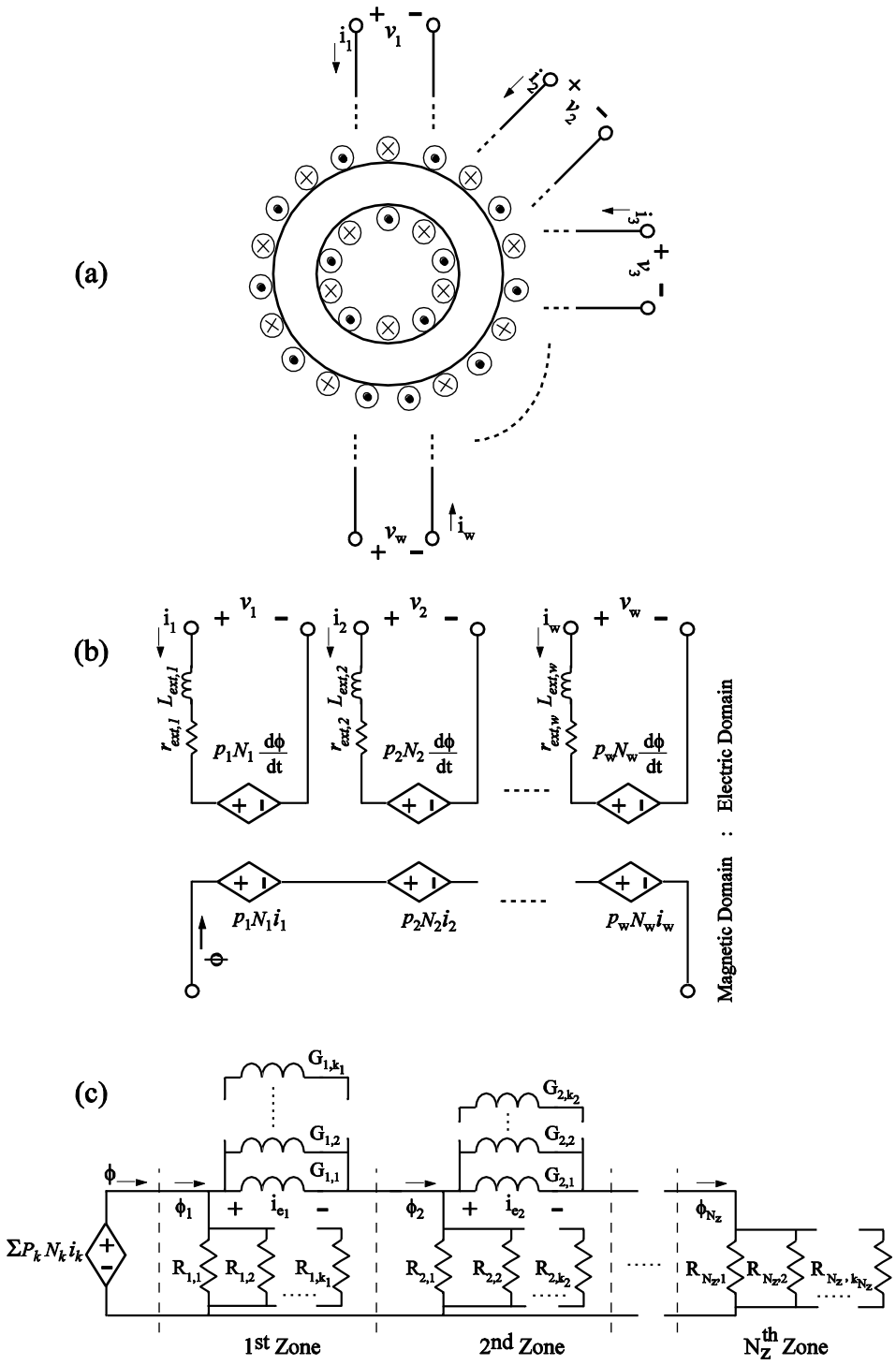

Fig. 3. 23. HFMEC model of a multiple-winding structure: (a) The multiple-winding structure; (b) Coupled electric-magnetic domain circuits; (c) Equivalent magnetic *R-L* structure resulting from detailed core cross-section meshing and associated flux tubes.

$$\begin{cases} \mathbf{E}\dot{\mathbf{x}} = \mathbf{A}\mathbf{x_f} + \mathbf{B}\mathbf{u} \\ \mathbf{y} = \mathbf{C}\mathbf{x_f} + \mathbf{D}\mathbf{u} \\ \mathbf{x}_f = \left[i_1, \cdots, i_w, \Phi_2, \cdots, \Phi_{N_z}\right]^T \\ \mathbf{u} = \left[v_1, \cdots, v_w\right]^T \\ \mathbf{C} = \left[\mathbf{I}_w \quad 0\right]_{w\times(w+N_z-1)} \\ \mathbf{D} = 0 \end{cases} \tag{3.21}$$

Matrices $\{\mathbf{A}, \mathbf{B}, \mathbf{C}, \mathbf{D}, \mathbf{E}\}$ define a standard state space form. Matrices $\mathbf{E}$ and $\mathbf{A}$ are large, sparse, and structured. The full state vector, $\mathbf{x_f}$, constitutes the external winding currents, i_k, and the zonal flux variables, Φ_k. The external winding input voltages, v_k, are considered as the input to the system, $\mathbf{u}$. The external winding currents, i_k, are the resulting system output, $\mathbf{y}$. The final model order is $w + N_z - 1$.

3.6.2 Model-order reduction

The proposed HFMEC is highly accurate but computationally expensive if a large set of magnetic zones, N_z, are required, e.g., for PWM excitations with rich frequency contents. The proposed HFMEC is a nonlinear system when saturation is considered in reluctance formulation. Iterative solvers required for accurate solution of nonlinear systems renders the full-order model impractical. This issue is addressed using MIMO order-reduction techniques.

3.6.2.1 Linearization based on steady-state solutions

Linear systems based on steady-state solutions are established. For stationary magnetic systems with fixed-coil winding distribution, the magnetic flux distribution and resulting effective permeability are determined by the steady-state input current level of all windings, $\left\{I_1^{ss}, I_2^{ss}, \cdots, I_w^{ss}\right\}$. The flux derivatives, and therefore the eddy currents, are zero in the steady state associated with dc current excitations. As seen in Fig. 3.23(b), the eddy currents are the MMF

drops over the transferences (magnetic inductances) in the magnetic domain circuit. In steady state, the *R-L* ladder structure of the magnetic domain circuit in Fig. 3.23(b) is simplified to a parallel combination of the nonlinear reluctances in Fig. 3.24. Then, corresponding permeability and reluctance terms are iteratively extracted by solving the nonlinear equations

$$\begin{cases} \sum_{k=1}^{w} p_k N_k I_k^{ss} = R_{j,1} \| \ldots \| R_{j,k_j} \times \left(\Phi_j - \Phi_{j+1} \right) & , j = 1 \cdots N_z \\ R_{j,1} \| \ldots \| R_{j,k_j} = R_j = \dfrac{l_j}{Area_j \mu_j \left(Area_j \times \left(\left(\Phi_j - \Phi_{j+1} \right) \right) \right)} \end{cases} \tag{3.22}$$

where p_k, N_k, I_k^{ss} are the polarity/direction, number of turns, and the given dc input current magnitude of the k^{th} winding. As shown in the reluctance formulation, the magnetic permeability, μ_j, is a function of the flux passing through the corresponding magnetic zone, $\left(\Phi_j - \Phi_{j+1} \right)$. The permeability, μ_j, is formulated as a polynomial function based on the B-H relationship shown in Fig. 3.25. The iterative solution of (3.22) at given dc current magnitudes provides the effective permeability in the j^{th} magnetic zone, μ_j. Thus, the saturated nonlinear model can be simplified to a simpler model around the steady state associated with given input currents $\left\{ I_1^{ss}, I_2^{ss}, \cdots, I_w^{ss} \right\}$. The small-signal parameters corresponding to different values of input dc currents are extracted and used to form appropriate transfer functions (dynamic admittance). It should be noted that the steady-state points are only used for model extraction, whereas the resulting final model is dynamic. The linear MIMO reduction techniques can now be applied.

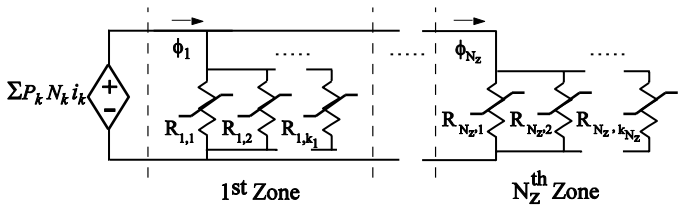

Fig. 3.24. Magnetic-domain circuit in steady state.

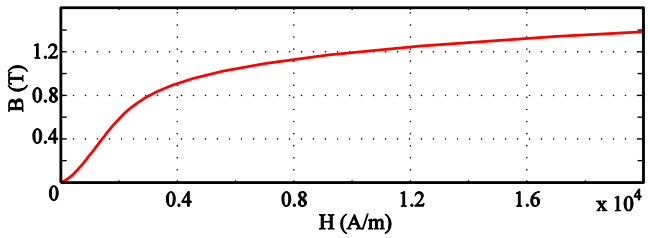

Fig. 3.25. Nonlinear magnetic charactersitics, B-H curve, for powdered iron [169] considered.

3.6.2.2 MIMO order-reduction procedure

The original model is of order *n*, i.e., it is described by *n* states. The goal is to generate a similar model with only *q* state variables $(n >> q)$, while preserving the original input-output relationship of the original model. Matrix Pade via Lanczos, PRIMA [53], block Arnoldi, global Lanczos [54], and global Arnoldi algorithms [55] are proposed for MIMO order reduction. The choice of order-reduction procedure is arbitrary and any linear MIMO method can be used. For the projection-type reduction techniques, an orthonormal projection matrix, $\mathbf{W}_{q\times n}$, can be generated from a p^{th}-order Krylov subspace:

$$\mathbf{K}_p\left(\mathbf{A}^{-1}\mathbf{E},\mathbf{A}^{-1}\mathbf{B}\right)=span\left\{\mathbf{A}^{-1}\mathbf{B},\cdots,\left(\mathbf{A}^{-1}\mathbf{E}\right)^{p-1}\mathbf{A}^{-1}\mathbf{B}\right\}\subseteq colsp\{\mathbf{W}\} \tag{3.23}$$

via the block Arnoldi method [79], where $q = p\cdot w$ and w is the number of inputs (i.e. number of winding sets). The reduced system matrices are extracted by applying the projection matix, $\mathbf{W}_{q\times n}$, in (3.23) to the original state matrices in (3.21) and modifying the state vector

$$\begin{cases}\mathbf{WE}\dot{\mathbf{z}}=\mathbf{WAW}'\mathbf{z}+\mathbf{WBu}=\mathbf{A}_r\mathbf{z}+\mathbf{B}_r\mathbf{u}\\ \mathbf{y}=\mathbf{CW}'\mathbf{z}=\mathbf{C}_r\mathbf{z}\\ \mathbf{z}_{q\times 1}=\mathbf{W}_{q\times n}\mathbf{x}_{n\times 1}\end{cases} \tag{3.24}$$

Equation (3.24) defines the new reduced-order (q^{th}-order) model. The resulting reduced-order transfer function will match the first p of the Taylor series expansion in the Laplace variable, s, of the original high-order system transfer function.

The order-reduction procedure is examined for a two-winding system, i.e., a transformer with geometrical data summarized in Appendix A.3. The magnetic core is a powdered iron core with material characteristics shown in Fig. 3.26. The high-order HFMEC model is linearized at the dc operating point $(i_1, i_2) = (2,1)$. The transfer functions from the first voltage to the first and second winding currents are extracted and shown in Fig. 3.26. The resistive effects of eddy current dynamics are obvious in higher frequency ranges. Linear order-reduction techniques are used to reduce the model order from 300 to only 4 state variables. The results are overlaid in Fig. 3.26, where an excellent match between corresponding reduced- and full-order models is observed. The condition numbers are 5.63×10^{6} and 3.33×10^{11}, and the fastest eigenvalues are -1.39×10^{9} and -1.04×10^{13} for reduced- and full-order models, respectively. Thus, the order reduction process greatly simplifies model execution and improves the accuracy of numerical integration for transient simulation.

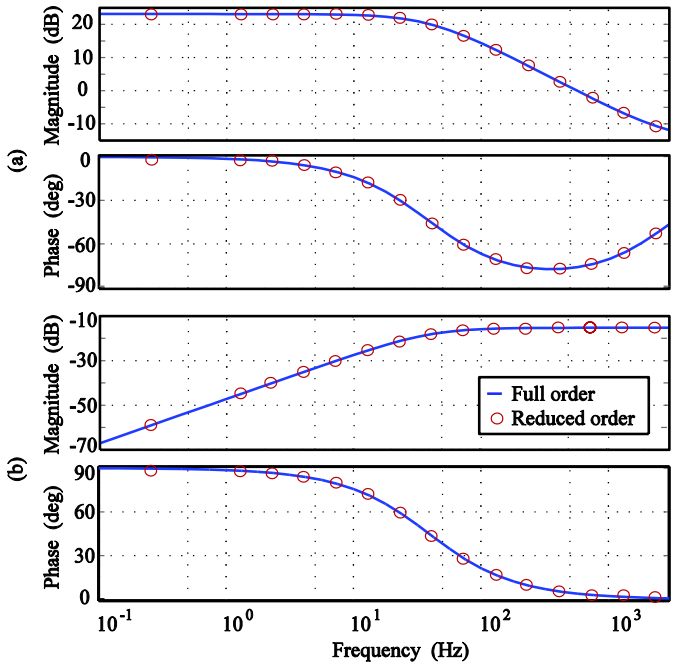

Fig. 3. 26. Full- and reduced-order transfer functions at operating point $i_1 = 2, i_2 = 1$ A: (a) From v_1 to i_1; (b) From v_1 to i_2.

3.6.2.3 Parameterization of reduced-order model

To facilitate nonlinear order reduction, reduced-order linear models are combined in a piecewise-linear fashion based on the winding current magnitudes. Trivially, for the multiple-winding case, the selection and combination of reduced-order linear models is based on the current level in each individual winding. This is a tedious process as the number of linearized systems increases on the order of m^w, where w is the number of windings and m is the number of linearized points required to sweep each current axis. For example, a 4-winding system with only 5 linearization points requires $5^4 = 625$ reduced-order models!

Certain winding configurations, material characteristics, and winding distributions in power electronics applications can alleviate the complexity of model formulation. First consider a Y-connected 3-phase transformer

$$\sum_{k=1}^{3} i_k = 0 \tag{3.25}$$

Thus only two independent currents are required. This shows how winding configurations can be used for structural reduction. A more elaborate discussion of structural reduction is given in [174]. Secondly, as seen in Fig. 3.25, the magnetic B-H curve can be well approximated with a few straight lines, i.e., only a few points along each current axis are required. Finally, in order to maximize the mutual inductance and minimize the leakage inductances, windings are evenly distributed over the magnetic core and are overlapped. This winding distribution implies that, in steady-state, the effective permeability of the magnetic reluctances in Fig. 3.23(b) can be solely determined by effective magneto-motive force $\sum_{k=1}^{w} p_k N_k i_k$. Thus, we use the total effective MMF to parameterize the reduced-order models

$$\xi = \sum_{k=1}^{w} p_k N_k i_k \tag{3.26}$$

Localized reduced-order models $\{\mathbf{A}_r, \mathbf{B}_r, \mathbf{C}_r, \mathbf{D}_r\}$, are formulated as numerical functions of ξ and are saved as lookup tables. The nonlinear order-reduction method is implemented, as shown in Fig. 3.27. In the transient simulation, for the given input voltage values, $(v_1(t_n), \cdots, v_w(t_n))$, and previously found $\xi(t_n)$, the corresponding system matrices are extracted from lookup tables to form a transfer function valid for the vicinity of $\xi(t_n)$:

$$[i_1(s), \cdots, i_w(s)]^T = \left[\mathbf{C}_r(\xi)[s\mathbf{I} - \mathbf{A}_r(\xi)]^{-1}\mathbf{B}_r(\xi) + \mathbf{D}_r(\xi)\right] * [v_1(s), \cdots, v_w(s)]^T \tag{3.27}$$

And the simulation proceeds to the next time step with updated current values, $(i_1(t_{n+1}), \cdots, i_w(t_{n+1}))$.

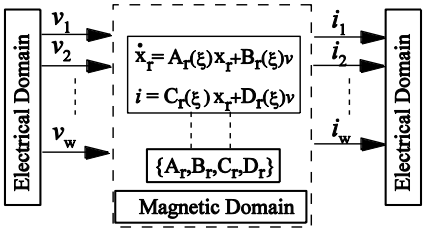

Fig. 3. 27. Implementation of the nonlinear order-reduction framework.

3.6.3 Model verification

The same two-winding system (e.g., a transformer) is discussed, although the proposed reduction framework is general and applicable to systems with an arbitrary number of windings. Two types of frequently encountered excitations in power electronics systems–PWM and sinusoidal excitations–are applied as the input voltage to the primary winding. The proposed full-order model has 300 state variables, and the reduced-order models have only 4 state variables.

First, a PWM input voltage with 12 V and 500 Hz frequency is applied to the primary winding. The measured current in Fig. 3.28(a) and the input current of the proposed nonlinear HFMEC model in Fig. 3.28(b) have an acceptable match. The slight difference can be attributed to the absence of magnetic hysteresis in the proposed HFMEC model, as well as the difference between the ideal voltage source used in the simulation study and the realistic voltage source used in the experimental setup. More importantly, as the study demonstrates, the input current waveform resulting from the reduced-order model (Fig. 3.28(c)) closely resembles that obtained from the full-order model (Fig. 3.28(b)), which verifies the reduction procedure. The induced secondary voltage and currents are extracted from the hardware measurement, full-order, and reduced-order models in Fig. 3.29(a), (b), and (c), respectively. The acceptable match among the respective model waveforms validates the accuracy of the original full-order HFMEC and verifies the proposed order-reduction process.

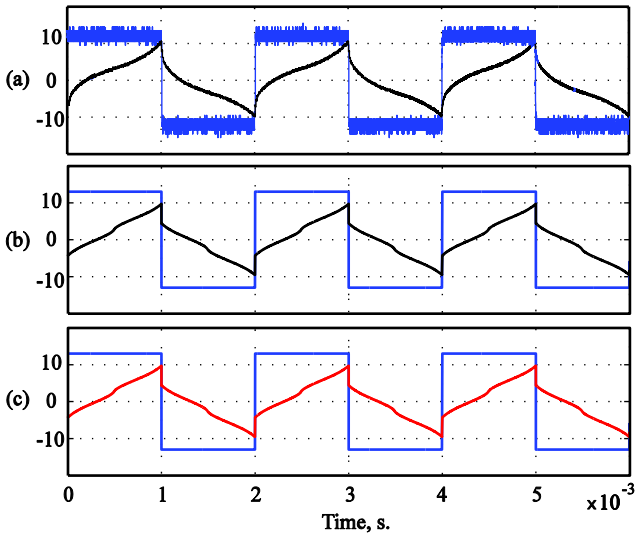

Fig. 3.28. PWM input voltage and resulting input current waveforms: (a) Hardware measurement; (b) Full-order HFMEC; (c) Reduced-order model.

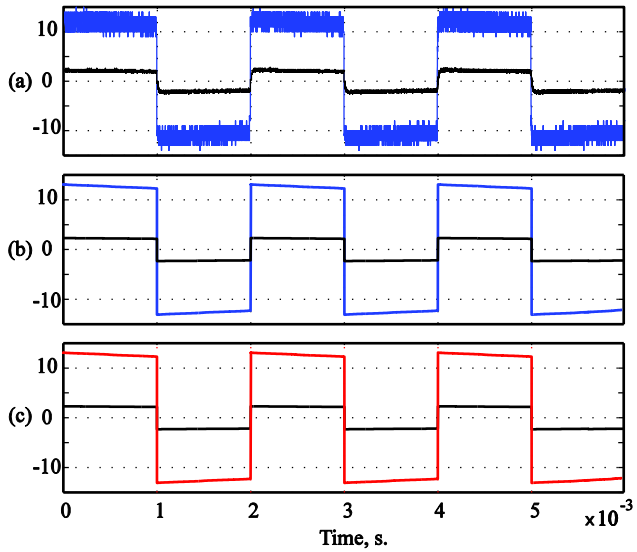

Fig. 3.29. Secondary voltage and current waveforms for a PWM excitation: (a) Measurement; (b) Full-order HFMEC; (c) Reduced-order model.

Next, a sinusoidal excitation with 18.5 V and 300 Hz frequency is applied to the primary winding. The primary and secondary winding waveforms are shown in Figs. 3.30 and 3.31, respectively. The primary and secondary current waveforms resulting from the proposed HFMEC model (Fig. 3.30(b) and 3.31(b)) closely resemble those extracted from the hardware setup. Moreover, respective current waveforms obtained from the reduced-order model match

those obtained from the hardware measurement and full-order HFMEC model. This verifies the reduction method.

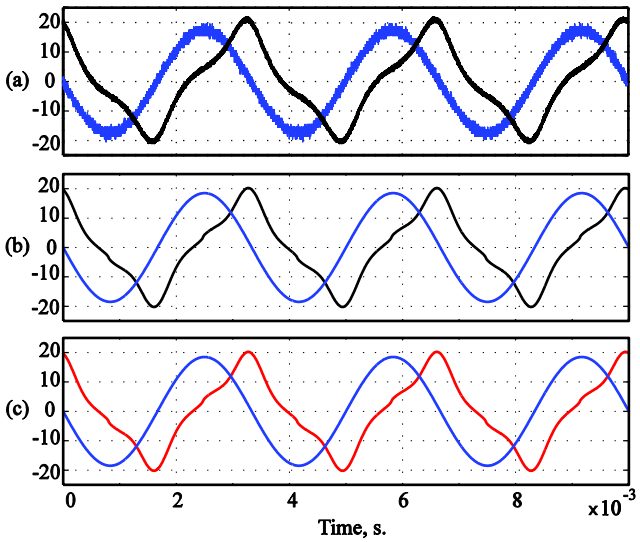

Fig. 3.30. Sinusoidal input voltage and resulting input current waveforms: (a) Measurement; (b) Full-order HFMEC; (c) Reduced-order model.

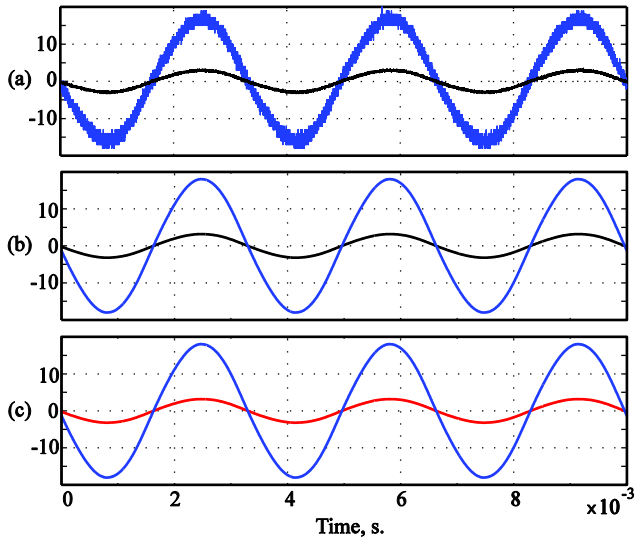

Fig. 3.31. Secondary winding waveforms for a sinusoidal excitation: (a) Measurement; (b) Full-order HFMEC; (c) Reduced-order model.

3.7 Summary

A general framework for accurate modeling of power electronics magnetic components is set forth. The proposed HFMEC model consists of modular flux tubes and a long *R-L* ladder structure in MEC to accurately represent the high-frequency eddy-current dynamics and 3-D and corner effects. The large number of state variables (typically several hundred) resulting from the HFMEC models is required to justify the assumption of uniform flux density in each cross segment/element. To obtain a more efficient reduced-order linear model that can be used for small-signal analysis, the quasi pole/zero cancellation, truncated balanced residuals, and fast state elimination are considered. To incorporate the nonlinearity introduced by saturation in the large-signal dynamic model, a piecewise linear order-reduction technique is set forth. For the two types of magnetic cores (powdered iron toroid and laminated steel toroid), the computational efficiency of the HFMEC models (with 400 and 300 state variables) is greatly improved by constructing the linear/nonlinear reduced-order models (with only 2 and 3 state variables) using the proposed order-reduction frameworks. The proposed models are verified in time and frequency domains with numerical simulation and hardware measurements.

Next, the proposed HFMEC model is extended to include relative motion and back EMF. The original high-order model is replaced with a piecewise linear reduced-order model that is a numerical function of the mechanical position and speed. The final reduced-order model is verified in both time and frequency domains. If this approach is to be employed as a design tool for electromechanical systems, force formulation is required. Direct Maxwell stress tensor [135] and virtual work methods based on the spatial derivatives of stored energy [131] are candidate approaches for force calculation, and are subjects of future work.

Finally, a technique for macro-modeling of a multiple-winding magnetic structure from physics-based HFMEC models is developed. Based on the effective magneto-motive force parameters in steady state, the nonlinear HFMEC model is linearized for different winding current combinations. As the model description is in state space form, many SISO reduction techniques can be generalized to the MIMO systems. The block Arnoldi method is used to reduce the resulting linear system in steady state. Then, a framework is provided to replace the original full-order model with a collection of parameterized reduced-order models. The final reduced-order model is verified in both time and frequency-domains for different excitation types using hardware measurements and the original full-order HFMEC.

CHAPTER 4

FINITE ELEMENT MODELS WITH RELATIVE MOTION

4.1 General Framework

Conventional reduced-order modeling of electromechanical systems is model-specific and depends on expert knowledge (e.g., lumped-parameter extraction by FEA [179]). Alternatively, an automated methodology is sought where the mathematics are rigorous yet transparent to the end user. A conceptual schematic for automated low-order model extraction of electro-mechanical systems is shown in Fig. 4.1(a). The basic principle of electromechanical systems requires three sets of equations (electromagnetic field, electric circuit, and mechanical laws) to be solved simultaneously [180]. The electrical and mechanical subsystems provide the input voltage, v_{in}, and mechanical position, x_p, to the magnetic subsystem. Although external and mechanical systems can be accurately modeled with a few state variables, the magnetic domain, where the diffusion and force components are coupled, significantly increases the system order. Thus, our order-reduction efforts are concentrated on physics-based models of the magnetic domain with interface variables from external electrical and mechanical domains (Fig. 4.1(b)). In this chapter, using a unified grid, magnetic field equations are modeled by FEM and later reduced.

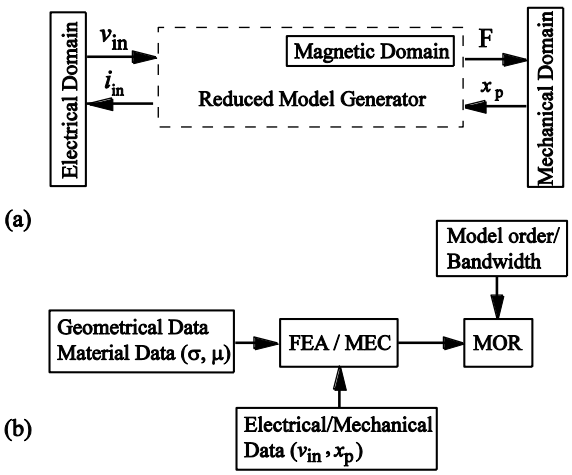

Fig. 4.1. Reduced-order modeling of electromechanical systems: (a) Hybrid electromechanical system representation; (b) Magnetic domain, reduced-model generator block diagram.

4.2 Mesh Generation for Incorporating Relative Motion

Mesh generation, domain discretization, and element assignment are the first steps in FEM formulation. Relative motion necessitates updating the original mesh (conventionally obtained through Delauney triangularization) or applying an adaptive rotation mesh in system dynamics. State variables are represented by magnetic vector potentials, **A**, associated with nodes generated in meshing process. In the partial or full re-meshing process, some nodes are removed or renumbered, and the mesh integrity is disturbed when the nodes in the mesh cross edges. As a consequence, corresponding magnetic vector potentials may not act as state variables. In other words, state equations describing the system dynamics at each time step are of different dimensions. One may use hybrid approaches that combine Laplace equations in an adaptive macro-element of the moving part, with a fixed-size FEM model of the ferromagnetic parts [181]. This imposes heavy restrictions on the geometry of the studied models, is heavily analytical, and relies on expert knowledge.

To address the above-mentioned issues, a fixed grid is considered for the linear plunger shown in Fig. 4.2. A unified grid is implemented where the movement path is discretized along the x-axis according to the device structure. The extension to the y-axis is straightforward. Also, rotary magnetic devices can be accommodated by considering the finite-element formulation in polar coordinates (r,θ). The magnetic domain is divided into two regions R_1 and R_2, where the second region contains the moving leg, as shown in Fig. 4.2. The movement path is discretized with fine grid resolution in R_2 to accurately incorporate relative movement. Moreover, a fine mesh facilitates accurate representation of magnetic fields in the air gap, where energy transfer occurs. Special attention is paid to the nodes on the boundary of R_1 and R_2, when both grids are overlaid. This is to meet the boundary conditions when using first-order elements in finite-element formulations [182]. Using fixed grid generation for the plunger shown in Fig. 4.2, 3577 nodes are created. Once elemental coordinates are extracted, state-space models can be generated by FEM.

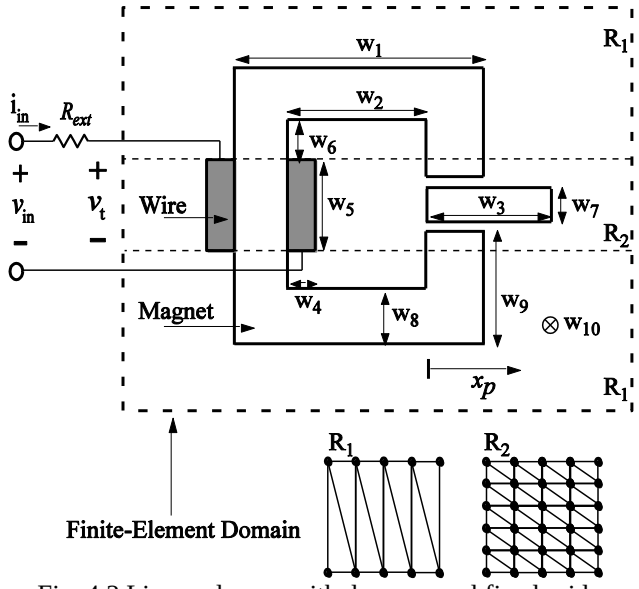

Fig. 4.2 Linear plunger with decomposed fixed grids.

4.3 State Space Model Formulation

A linear plunger, with geometrical and material data summarized in Appendix A.4, is considered in Fig. 4.2. The moving leg position is externally determined (through force formulation and mechanical constraint). A slow variation in mechanical position is considered and, therefore, the back EMF is neglected. FEM formulation of stationary inductors is described in the literature, e.g. [163], and is extended to the resulting position-dependent inductor. Starting from Gauss's law,

$$\nabla \cdot \mathbf{B} = 0 \tag{4.1}$$

, where B is the magnetic flux density, one can define a magnetic vector potential, **A**, such that

$$\nabla \times \mathbf{A} = \mathbf{B} \tag{4.2}$$

The gauge condition (Coulomb gauge)

$$\nabla \cdot \mathbf{A} = 0 \tag{4.3}$$

uniquely defines **A** and leads to better conditioned system matrices. One may formulate the magnetic field equations using (4.2), Ampere's law, Faraday's law, and material characteristics as

$$\begin{cases} \nabla \times \mathbf{A} = \mathbf{B} \\ \nabla \times \mathbf{E} = \dfrac{-\partial \mathbf{B}}{\partial t} \\ \nabla \times \mathbf{H} = \mathbf{J} \\ \mathbf{B} = \mu \mathbf{H} \\ \mathbf{J} = \sigma \mathbf{E} \end{cases} \Rightarrow \nabla \times \frac{1}{\mu} \nabla \times \mathbf{A} = \sigma \left(\frac{v_{b_i}}{w_{10}} - \frac{\partial \mathbf{A}}{\partial t} \right), \; i = 1,2 \tag{4.4}$$

where **H** and **E** are magnetic and electric field intensities, **J** is the current density, and w_{10} is the depth into the page. Electric conductivity σ and magnetic permeability μ vary in the x-axis and y-axis directions. There are three regions—air, magnet, and copper—with different material

characteristics—$(\sigma = 0; \mu_r = 1)$, $(\sigma = 200; \mu_r = 4000)$ and $(\sigma = 5 \times 10^7; \mu_r = 1)$, respectively. The terms v_{b1} and v_{b2} are the bar voltages over the left and right wires, respectively. The eddy-current contribution is denoted by $\sigma \frac{\partial \mathbf{A}}{\partial t}$. In the 2-D case considered, flux density **B** and field intensity **H** have x-axis and y-axis components

$$\begin{cases} \mathbf{B} = B_x \vec{a}_x + B_y \vec{a}_y \\ \mathbf{B} = B_x \vec{a}_x + B_y \vec{a}_y \end{cases} \tag{4.5}$$

Thus, magnetic vector potentials **A** and current density **J** have only z-axis components

$$\begin{cases} \mathbf{A} = A_z \vec{a}_z \\ \mathbf{J} = J_z \vec{a}_z \end{cases} \tag{4.6}$$

This simplifies the vector-based partial differential equations into a scalar-based ODE for magnetic vector potentials in the z-axis, $\mathbf{A}_z$(x,y), as

$$-\nabla \cdot \frac{1}{\mu} \nabla A = \sigma \left(\frac{v_{b_i}}{w_{10}} - \frac{\partial A}{\partial t} \right), i = 1,2 \tag{4.7}$$

Applying the Galerkin method [182] to first-order linear elements and patching the elemental equations into a global system of equations yields the global state equations

$$\mathbf{S}\mathbf{A} = \mathbf{P} i_{in} + (\mathbf{C} - \mathbf{T}) \frac{d\mathbf{A}}{dt} \tag{4.8}$$

where matrices $\mathbf{S}_{n \times n}$, $\mathbf{C}_{n \times n}$, and $\mathbf{T}_{n \times n}$, and vector $\mathbf{P}_{n \times 1}$ are standard notations found in all classic finite element textbooks [182-183]. $\mathbf{A}_{n \times 1}$ constitutes the global vector of the magnetic vector potential where *n* is the number of nodes after the redundant coincident elemental nodes are eliminated. Matrix **C** is a function of electric conductivity and thus zero outside the wire regions. Matrix **S** is a function of permeability and thus varies by the position of the moving leg. Matrix

T and vector **P** are constant. Moreover, over the wire regions, the FEM formulation leads to [163]

$$i_{b_i} = \frac{\sigma_{copper}\left(w_4 \times w_5\right)}{w_{10}} v_{b_i} - \mathbf{b}_i' \frac{d\mathbf{A}}{dt} \quad i = 1,2 \tag{4.9}$$

Vector **b** is a standard FEA vector that is a function of electrical conductivity and thus is zero outside the wire regions. The details of model formulation are given in full in [163], and are omitted here for brevity. The finite element region and external circuit variables are coupled via

$$\begin{cases} v_{in} = v_{b_1} - v_{b_2} + R_{ext} i_{in} \\ i_{in} = i_{b_1} = -i_{b_2} \end{cases} \tag{4.10}$$

Equations (4.8)-(4.10) define the final full-order differential-algebraic equations. The original model is of order 3577, and is reduced to only 3 state variables in the next section.

4.4 Order Reduction and Model Verification

For a given position of the moving leg, x_p, the resulting FEM is linear. The linear state-space model at each discreet point in the movement path is of order 3577, and includes both algebraic and state variables. The state variables are associated with the induced eddy current, $\sigma \frac{\partial \mathbf{A}}{\partial t}$, corresponding to nodes in the magnet and copper regions. The electric conductivity of air is zero, and corresponding entries in matrices C and **T** in (4.8) are zero. Thus nodes in the air have associated algebraic variables. They can be algebraically related to the nodes in the magnet and copper and can be removed from the state equations. Kron reduction, as set forth in Chapter 2, is used to eliminate the algebraic variables associated with the nodes in the air. The system equation in (4.8) is partitioned to

$$\begin{bmatrix} \mathbf{S}_{mm} & \mathbf{S}_{mb} & 0 \\ \mathbf{S}_{bm} & \mathbf{S}_{bb} & \mathbf{S}_{ba} \\ 0 & \mathbf{S}_{ab} & \mathbf{S}_{aa} \end{bmatrix} \mathbf{A} = \begin{bmatrix} \mathbf{p}_m \\ \mathbf{p}_b \\ 0 \end{bmatrix} i_{in} + \begin{bmatrix} \mathbf{T}_{mm} - \mathbf{C}_{mm} & \mathbf{T}_{mb} - \mathbf{C}_{mb} & 0 \\ \mathbf{T}_{bm} - \mathbf{C}_{bm} & \mathbf{T}_{mm} - \mathbf{C}_{mm} & 0 \\ 0 & 0 & 0 \end{bmatrix} \frac{d\mathbf{A}}{dt} \tag{4.11}$$

where vector nodes are associated with metal/magnet, air, and metal/magnet-air boundaries, denoted by subscripts *m*, *a*, and *b*, respectively. The magnetic vector potential, **A**, is partitioned as

$$\mathbf{A} = \begin{bmatrix} \mathbf{A}_m & \mathbf{A}_b & \mathbf{A}_a \end{bmatrix}'. \tag{4.12}$$

By applying Kron reduction to the symmetric equations in (4.11), one may have

$$\begin{cases} \begin{bmatrix} \mathbf{S}_{mm} & \mathbf{S}_{mb} \\ \mathbf{S}_{bm} & \mathbf{S}_{bb} - \mathbf{S}_{ba}\mathbf{S}_{aa}^{-1}\mathbf{S}_{ab} \end{bmatrix} \mathbf{A}_r = \begin{bmatrix} \mathbf{p}_m \\ \mathbf{p}_b \end{bmatrix} i_{in} + \begin{bmatrix} \mathbf{T}_{mm} - \mathbf{C}_{mm} & \mathbf{T}_{mb} - \mathbf{C}_{mb} \\ \mathbf{T}_{bm} - \mathbf{C}_{bm} & \mathbf{T}_{mm} - \mathbf{C}_{mm} \end{bmatrix} \frac{d\mathbf{A}_r}{dt} \\ \mathbf{A}_r = \begin{bmatrix} \mathbf{A}_m & \mathbf{A}_b \end{bmatrix}' \end{cases} \tag{4.13}$$

where nodes in the air are eliminated, but can be retrieved algebraically from the state equations

$$\mathbf{A}_a = -\mathbf{S}_{aa}^{-1}\mathbf{S}_{ab}\mathbf{A}_b \tag{4.14}$$

Equations (4.9) also will be modified accordingly. This reduces the model order from 3577 to 1638. Equations (4.9) and (4.13) now define a new state equation after primary Kron reduction

$$\begin{cases} \dfrac{d\mathbf{A}_r}{dt} = \mathbf{A}_{ss}(x_p)\mathbf{A}_r + \mathbf{B}_{ss}(x_p)v_{in} \\ i_{in} = \mathbf{C}_{ss}(x_p)\mathbf{A}_r + \mathbf{D}_{ss}(x_p)v_{in} \end{cases} \tag{4.15}$$

where $\{\mathbf{A}_{ss}(x_p), \mathbf{B}_{ss}(x_p), \mathbf{C}_{ss}(x_p), \mathbf{D}_{ss}(x_p)\}$ are position-dependent state matrices. The input-impedance transfer function is formulated at each point on the path, where a small set of transfer functions is extracted. Respective full-order models are reduced using quasi pole-zero cancellation and fast state elimination, as explained in Chapter 2, corresponding to several points on the movement path. The full- and reduced-order transfer functions for two extreme locations of the moving leg

(all in and all out) are plotted in Fig. 4.3, where an acceptable match between respective models is observed. For the plunger at x_p = 0, the condition numbers of full- and reduced-order models are 1.56×10^9 and 735, respectively. For the plunger at x_p = 4 cm, the condition numbers of the full- and reduced-order models are 1.76×10^9 and 270, respectively.

The resulting reduced-order models are incorporated in a position-dependent, piecewise-linear reduced-order model as described in Chapter 2 and shown in the block diagram in Fig. 4.4. A PWM input voltage with a 1 V amplitude, 10 kHz switching frequency, and a sinusoidally varying position, $x_p = 2 + 2\sin(2000\pi t)$ cm, are applied to the electromechanical system in Fig. 4.2. The input current predicted by the reduced-order model is portrayed in Fig. 4.5. As expected, as the leg moves outward, the resulting air gap reluctance is increased. This, in turn, reduces the equivalent dynamic inductance magnitude, which increases the current magnitude for a given input voltage.

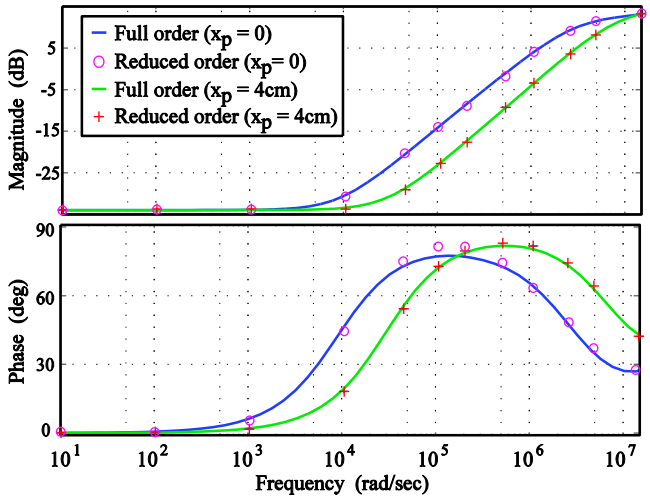

Fig. 4.3 Reduced- and full-order transfer functions for different locations $(x_p = 0)$ and $(x_p = 4cm)$ of the moving leg in FEM.

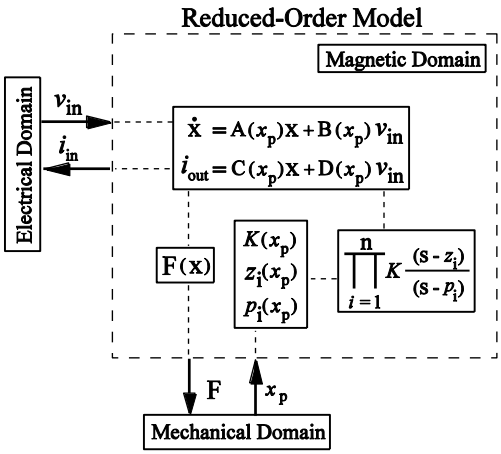

Fig. 4.4. Implementation of the proposed reduced-order model.

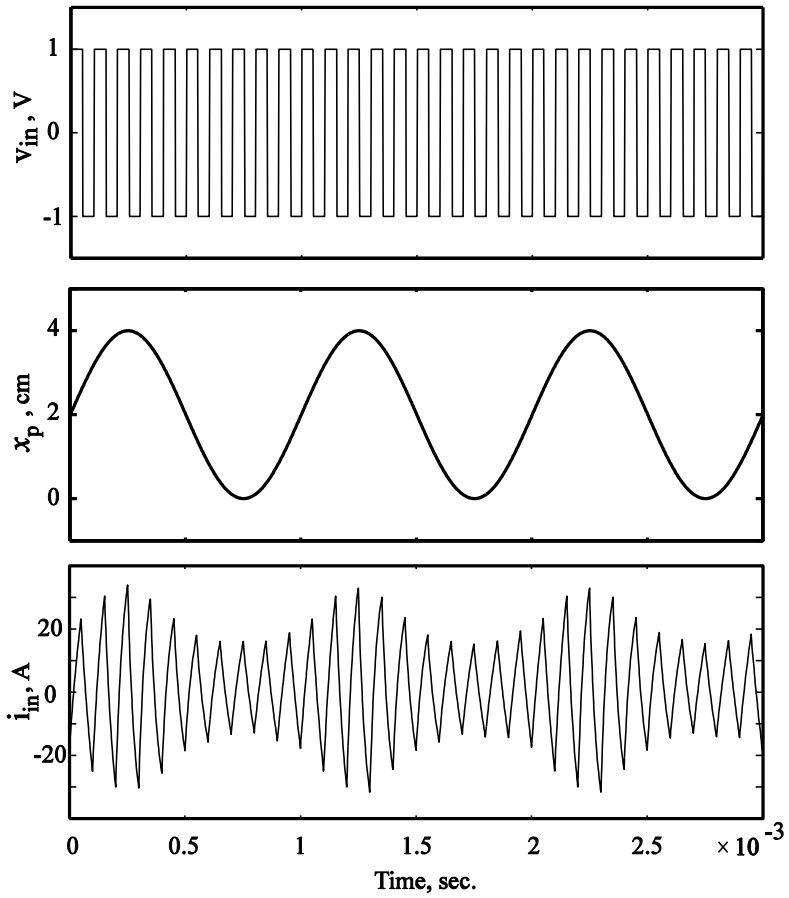

Fig. 4.5 Input voltage, moving leg position, and the input current in the reduced-order FEA model.

4.5 Summary

A general framework for reduced-order finite-element modeling of magnetic devices in electromechanical systems is set forth. The relative movement in FEM is facilitated by discretizing the movement path. For each discrete point on the movement path, the state vector dimension is preserved. FEM is formulated as a position-dependent inductor. Kron reduction, quasi pole/zero cancellation, and fast-state elimination are considered to reduce the linear system order in a small-signal sense. Next, a piecewise linear order-reduction technique is set forth to dynamically incorporate the relative motion. Computational efficiency is greatly improved as the system order is reduced to only 3, starting from 3577 state variables originally introduced by the FEM. The proposed order-reduction framework is verified in time and frequency domains. The provided rapid-to-simulate magnetic-domain components are then integrated into the hybrid simulation environment, as shown in Fig. 4.1(b).

CHAPTER 5

MULTIRESOLUTION SIMULATION OF CONVERTERS

5.1 Switching Converter Simulation Overview

Accurate and fast simulation environments are required for dynamic characterization and transient studies of switching converters [4, 184-187]. Accuracy and fidelity of simulation depends on the level of detail considered in model formulation. Thus, highly accurate models that incorporate high-frequency effects are inevitably slow to simulate and ill-conditioned. This is further pronounced in higher frequency cascaded converters, or in the presence of nonlinear components that require iteration. Simulation acceleration techniques are mainly geared toward a fast periodic steady-state characterization (e.g., shooting methods [188-189]), or a fast solution of differential equations (e.g., Chebyshev series expansion [186, 190] and envelope following [191]). Model restructuring may also improve simulation speed and accuracy (e.g., the voltage-behind-reactance model of grid-interconnected electrical machines [192], [193]).

Although power electronics systems can be simulated as purely continuous models (e.g., using bond graph formalism [194-196] or generalized state-space averaging [197-200]), they are often represented as a hybrid system that combines discrete transition conditions with continuous differential equations [201]. This requires accurate switching-event detection, solvers for (possibly stiff) piecewise-linear ordinary differential equations (ODE), and proper initialization of solution segments. Although some references have discussed numerically efficient switching-event implementation [202-203], the main research thrust has been to find appropriate ODE solvers.

If one uses a fixed-step explicit solver (e.g., Euler, Runge-Kutta, Adams-Bashforth, etc.), fast state variables demand small step sizes to ensure numerical stability. This makes the simulation computationally intensive even though fast dynamics subside quickly. If one uses variable-step stiff solvers (e.g., Gear's BDF or NDF, Adams-Moulton, etc.), the integration step size is adjusted to conform to system dynamics as simulation proceeds [204], [205]. The implicit ODE solvers may require solution of nonlinear equations, evaluation of Jacobian matrix (e.g. Rosenbrock formula), and iterations which add to the overall calculations. The periodic excitation of the switching transients prevents the integration step size from increasing significantly. This puts an additional challenge on the use of single-rate ODE solvers for high-frequency switching converters [206-208]. Parallel computation, wherein computational tasks are executed on remote computer nodes, often leads to only a linear speedup. Alternative approaches are multirate/multiscale simulation techniques.

In multirate/multiscale simulation schemes, using time-scale separation techniques, the overall system is decoupled into two [188, 208] or more [209-210] fast and slow subsystems. Likewise, the power-electronic circuit can be divided into subcircuits with different time constants [211]. Once partitioned, individual subsystems could be solved with different ODE solvers and integration step sizes. Multi-rate simulation usually requires modifying the built-in integration algorithms available in commercial simulation packages. The resynchronization of the different subroutines may occur at the largest step size. Fixed step-time solvers are used to simulate fast and slow subsystems in [212]. There, the step size used in the slow subsystem is an integer multiple of the step size of the fast subsystem. A zero-order hold is used to keep the output of the slow subsystem constant, and to transfer data between slow and fast subsystems at communication intervals. This imposes severe restrictions on communication intervals between

fast/slow subsystems and may potentially introduce sampling and aliasing errors [208]. The multi-rate method introduced in [208] requires a predictor step, an interpolation of the slow state variables within the fast subsystems, and an averaging of the fast variables within the slow subsystems. A mixture of multirate and parallel simulation (distributed heterogeneous simulation) is used to further speed up the simulation process [213]. Despite appreciable improvements in simulation speed, in general, multi-rate approaches can only be effectively realized for a carefully partitioned system and provide a single resolution. Thus, flexible resolution simulation frameworks are indispensible.

Available multiresolution simulation (MRS) environments manually switch between two levels of pre-fixed simulation complexity. Switch-level model waveforms can be analytically constructed from an average-value model [214-215]. A combination of two diode models—a behavioral model based on Shockley equations and a physical model based on lumped charge theory—is considered in [216]. A multi-order model of super capacitors is presented by switching between different equivalent RLC ladder structures [217]. Reference [206] utilizes two models of a surface-mounted PMSM, a low-frequency model based on classic Park equations and a high-frequency model based on operating impedance matrix. Despite their relative accuracy, in all the above examples, only two levels of resolution are intuitively provided, and the transition from one resolution to another is neither clear nor mathematically rigorous.

It seems intuitive to utilize order reduction and extract an arbitrary level of simulation resolution. The concepts of time-scale separation, integral manifold, and singular perturbation are used to extract the reduced-order models of interconnected multi-machine power systems [218-220], induction machines [221], and power-factor correction circuits [222]. Coherency [223-224] and synchrony [225-226] are common concepts in reduced-order modeling of power

systems. Order reduction has been widely used in power systems but has a small presence in power electronics. It is used to eliminate all but dominant eigenvalues in control-to-output transfer functions of a Cuk converter [227]. Black-box terminal characterization of multi-converter systems is formed based on frequency responses, and is later reduced [228], [229]. Krylov subspace-based methods are used to extract compact thermal models of the IGBT modules from finite-element models [230]. Reduced-order models are also gaining interest in real-time simulation of power systems with power-electronics-based protection systems [231].

This chapter investigates the application of order reduction in variable-resolution simulation of switching converters. Several models with different resolution levels are numerically extracted using order-reduction techniques. The technique is examined on a switched linear system, and then extended to cascaded, nonlinear, and closed loop converters. MRS is also applied to the continuous representation of switching converters using generalized state-space averaging.

5.2 Detailed Model Development

Power-converter model synthesis consists of component models and control laws. First, high-order detailed models of switching-converter components, shown in Fig. 5.1, are set forth. A wide-bandwidth inductor model includes equivalent series resistance, r_L, and lumped shunt parasitic capacitance, c_L [232]. Alternatively, the inductor macromodel developed in Chapter 4 can be fit into second-order circuit parameters. The equivalent series resistance, r_C, and inductance, L_C, of the capacitor are extracted from the hardware prototype using impedance characterization. Switching-component modeling is more challenging, as the resulting model should predict accurately both steady-state characterizations as well as fast dynamics. The MOSFET is represented as a switching-state-dependent resistance $\{r_{sw}(off), r_{sw}(on)\}$ with

appropriate drain-to-source parasitic capacitance, C_{sw}, and wiring inductance, L_{sw}. These values can be found in MOSFET data sheets [233], [234]. The static V-I characteristics of the diode can be modeled as a diode state-dependent series resistance $\{r_d(off), r_d(on)\}$ and an offset voltage source $\{V_d(off), V_d(on)\}$. The capacitance exhibited by semiconductor-metal junctions plays a dominant role in turn-on/-off transients [235]. Therefore, the switching transient dynamics, such as reverse recovery, are accounted for by a diode state-dependent linear capacitor, C_d. The capacitance is higher when the diode is off. A series resistance is considered with this capacitor, r_{C_d}, to damp the reverse-recovery current [236]. Wiring inductance and resistance of the diode (L_d and r_{L_d}) are also considered. A different variation of this diode model is presented in [237]. It should be noted that proposed models in Fig. 5.1 are just one form of model development; one can also use alternative piecewise-linear high-fidelity component models.

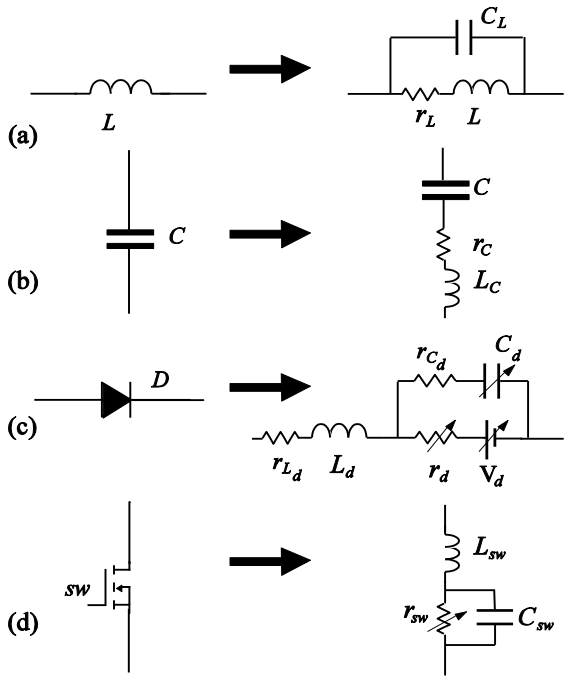

Fig. 5.1. Highly detailed behavioral component models: (a) Inductor; (b) Capacitor; (c) Diode; (d) MOSFET.

As seen in Fig. 5.1, switching component models and, subsequently, the final converter model depend on the state of switching components. Switching state and timing are either externally determined by a command signal (transistors turn on/off), or internally resolved by meeting appropriate threshold conditions (e.g., diodes). Mathematically, the switching time constraint equation can be expressed as [238]

$$c^j\left(\mathbf{x}^j\left(t_f^j\right),\mathbf{u}\left(t_f^j\right),t_f\right)=0 \tag{5.1}$$

where t_f^j is the time to exit the j^{th} topological instance. If the gate-drive dynamics are neglected, the MOSFET switching state and timing are determined solely by the duty cycle as

$$sw(MOSFET)=\begin{cases}1 & 0\le t<dT_s\\ 0 & dT_s\le t<T_s\end{cases} \tag{5.2}$$

where d is the MOSFET duty cycle and T_s is the switching interval. The diode is implemented as a module with autonomous control [239] that depends only on the terminal characteristics and previous switching state of the diode:

$$sw_+(diode)=\begin{cases}1 & \left(\left(sw\_(diode)=0\right)\wedge\left(v_{diode}\rangle V_d(on)\right)\right)\vee\left(\left(sw\_(diode)=1\right)\wedge\left(i_{diode}\rangle 0\right)\right)\\ 0 & otherwise\end{cases} \tag{5.3}$$

where $sw_+(diode)$ and $sw\_(diode)$ are current and previous switching stages of the diode, respectively. The variables v_{diode} and i_{diode} are the diode voltage and current, respectively. In a system with N_s switches, the topological instance, **S**, of the converter is an N_s-tuple of the switching states [240-242]

$$\mathbf{S}\in\{0,1\}^{N_s} \tag{5.4}$$

where 0 and 1 indicate that the corresponding switch is off or on. There are potentially 2^{Ns} different topological instances, some leading to undesirable/unreachable topologies. The switching cycle is defined as a periodically repeated sequence of topologies observed in steady state:

$$\{\mathbf{S}\}_i^{i+p-1} = \left(\mathbf{S}_i, \mathbf{S}_{i+1}, \cdots, \mathbf{S}_{i+p-1}\right) \quad , \mathbf{S}_{i+p} = \mathbf{S}_i \tag{5.5}$$

The converter model is represented as a hybrid system. The state-space model of the converter in the k^{th} topological instance, $\mathbf{S_k}$, is

$$\begin{cases} \dot{\mathbf{x}}_k = F_k\left(\mathbf{x}_k, \mathbf{u}, t\right) & , t \in [t_k^o, t_k^f\ ] \\ \mathbf{y}_k = g_k\left(\mathbf{x}_k, \mathbf{u}, t\right) \end{cases} \tag{5.6}$$

which can be simplified to (5.7) for a converter with linear time-invariant (LTI) elements

$$\begin{cases} \dot{\mathbf{x}} = \mathbf{A}_k \mathbf{x} + \mathbf{B}_k \mathbf{u} & , t \in \left[t_k^o, t_k^f\ \right] \\ \mathbf{y} = \mathbf{C}_k \mathbf{x} + \mathbf{D}_k \mathbf{u} \end{cases} \tag{5.7}$$

where $\{\mathbf{A}_k, \mathbf{B}_k, \mathbf{C}_k, \mathbf{D}_k\}$ are the system matrices in the k^{th} subinterval. Initial conditions of (5.6) and (5.7) are established from the final state values $\mathbf{x}_{k-1}\left(t_{k-1}^f\right)$ in the previous topological instance, $\mathbf{S}_{k\text{-}1}$,

$$\mathbf{x}_k\left(t_k^0\right) = \mathbf{T}_{k-1}^k \mathbf{x}_{k-1}\left(t_{k-1}^f\right) \tag{5.8}$$

where $\mathbf{T}_{k-1}^k$ is the boundary transformation matrix [241] relating two topological instances based on the continuity of capacitor voltages and inductor currents. In the cases considered here, there exists a global state vector independent of the switching instance. Thus, when a switching event is detected, the terminal value of the state vector in the previous topological instance is set as the initial condition of the state variables for the next topological instance. The time at which the switching converter leaves the topological instance, $\mathbf{S}_k$, is found through the switching constraint

$$c_k\left(\mathbf{x}_k\left(t_k^f\right),\mathbf{u}\left(t_k^f\right),t_k^f\right)=0 \tag{5.9}$$

The continuous state-space model is determined by partitioning the circuit graph to the spanning tree and link branches, and choosing the inductive link currents and capacitive tree voltages as the state variable [240, 243-244]. This process is automated in available numerical toolboxes (e.g., automated state model generator [241-242]). Based on the component models in Fig. 5.1, the state vector consists of inductor currents and capacitor voltages of both bulky and parasitic components

$$\mathbf{x}=\left[i_L^1,\cdots,i_L^{k_L},v_C^1,\cdots,v_C^{k_C},i_{L_{sw}}^1,\cdots,i_{L_{sw}}^{k_{sw}},v_{C_{sw}}^1,\cdots,v_{C_{sw}}^{k_{sw}},i_{L_d}^1,\cdots,i_{L_d}^{k_d},v_{C_d}^1,\cdots,v_{C_d}^{k_d},i_{L_C}^1,\cdots,i_{L_C}^{k_C},v_{C_L}^1,\cdots,v_{C_L}^{k_L}\right]' \tag{5.10}$$

where k_L,k_C,k_{sw},k_d are the number of inductors, capacitors, active switches, and diodes. The input vector is composed of the input voltage sources, load currents, and the diode voltage drop

$$\mathbf{u}=\left[v_g^1,\cdots,v_g^{k_g},i_{Load}^1,\cdots,i_{Load}^{k_{i_{Load}}},V_d^1(on),\cdots,V_d^{k_d}(on)\right]' \tag{5.11}$$

System dynamics (5.6), (5.7), initial and final conditions in (5.8) and (5.9), and switching logic (5.9) thus define the high-order model of the converter with the switching cycle in (5.5), and state and input variables in (5.10) and (5.11).

5.3 MRS Frameworks for Switched Linear Systems

Several model order/simulation resolutions of LTI systems in each topological instance (5.7) are achievable via linear order-reduction techniques of Chapter 2. Moment-matching, SVD-based, and generic reduction schemes are adopted from Chapter 2 and corresponding MRS environments are developed. Each reduced-order model will have different system matrices and state vectors. The latter do not necessary refer to the same physical variables. This complicates

model derivation as the state continuity should be insured across both different simulation resolutions and different switching events. The state continuity across different switching events is accounted for in (5.8). The state continuity across different resolutions is ensured with careful initialization of the new resolution. As the reduction is applied in each topological instance, the system matrix subscripts of (5.7) are dropped for brevity.

5.3.1 Krylov-subspace methods

Krylov subspace-based methods are projection-based moment-matching order-reduction techniques that project a higher order state space into a lower order space. An orthonormal projection matrix, $\mathbf{W}$, is generated from a qth-order Krylov subspace,

$$\mathbf{K}_q\left(\mathbf{A}^{-1},\mathbf{B}\right)=span\left\{\mathbf{B},\mathbf{A}^{-1}\mathbf{B},\cdots,\left(\mathbf{A}^{-1}\right)^{q-1}\mathbf{B}\right\} \tag{5.12}$$

using the Arnoldi method, where $q<n$ and n is the original system order. The full-order state vector is projected into a lower order state vector by a similarity transform:

$$\mathbf{z}=\mathbf{W}\mathbf{x} \quad ,\mathbf{z}\in\Re^{q_1} \quad ,\mathbf{x}\in\Re^{n} \quad ,\mathbf{W}\in\Re^{q_1\times n} \tag{5.13}$$

Likewise the reduced system matrices are extracted by applying the projection matix (5.12) to the original state matrices in (5.7) and modifying the state vectors

$$\begin{cases}\dot{\mathbf{z}}=\mathbf{W}\mathbf{A}\mathbf{W}'\mathbf{z}+\mathbf{W}\mathbf{B}\mathbf{u}=\mathbf{A}_r\mathbf{z}+\mathbf{B}_r\mathbf{u}\\ \mathbf{y}=\mathbf{C}\mathbf{W}'\mathbf{z}+\mathbf{D}\mathbf{u}=\mathbf{C}_r\mathbf{z}+\mathbf{D}_r\mathbf{u}\end{cases} \tag{5.14}$$

Switching between two arbitrary resolution levels is facilitated using different projection matrices. For example, two simulation resolution levels, q_1, q_2, can be extracted using two

orthonormal projection matrices, $\mathbf{W}_1, \mathbf{W}_2$. The resulting system equations are

$$\begin{cases} \dot{\mathbf{x}}_1 = \mathbf{W}_1\mathbf{A}\mathbf{W}_1'\mathbf{x}_1 + \mathbf{W}_1\mathbf{B}\mathbf{u},\ \mathbf{x}_1 = \mathbf{W}_1\mathbf{x},\ \mathbf{x}_1 \in \Re^{q_1} \\ \mathbf{y} = \mathbf{C}\mathbf{W}_1'\mathbf{x}_1 + \mathbf{D}\mathbf{u},\ \mathbf{x} = \mathbf{W}_1'\mathbf{x}_1,\ \mathbf{x} \in \Re^{n} \end{cases} \tag{5.15}$$

$$\begin{cases} \dot{\mathbf{x}}_2 = \mathbf{W}_2\mathbf{A}\mathbf{W}_2'\mathbf{x}_2 + \mathbf{W}_2\mathbf{B}\mathbf{u},\ \mathbf{x}_2 = \mathbf{W}_2\mathbf{x},\ \mathbf{x}_2 \in \Re^{q_2} \\ \mathbf{y} = \mathbf{C}\mathbf{W}_2'\mathbf{x}_2 + \mathbf{D}\mathbf{u},\ \mathbf{x} = \mathbf{W}_2'\mathbf{x}_2,\ \mathbf{x} \in \Re^{n} \end{cases} \tag{5.16}$$

where $\mathbf{x}_1, \mathbf{x}_2$ and $\mathbf{x}_2$ are the full-order, q_1-order, and q_2-order state vectors. Then, if the simulation resolution needs to change from q_1 to q_2 at an arbitrary time t_s, one may re-initialize the state vector in (5.16) by applying a similarity transform to the state variables in (5.15):

$$\mathbf{x}_2(t_s) = \mathbf{W}_2\mathbf{W}_1'\mathbf{x}_1(t_s) \tag{5.17}$$

The simulation engine proceeds with the system matrices shown in (5.16) and the initial values determined according to (5.17).

5.3.2 Balanced reduction methods

Balanced reduction methods are SVD-based methods used to eliminate state variables with the least contribution to the input-output relationship (e.g., [65]). The full-order system is first balanced using a balancing matrix, **T**, found in (2.20) and sorting the state vector based on the associated Hankel singular values:

$$\begin{cases} \dfrac{d\tilde{\mathbf{x}}}{dt} = \tilde{\mathbf{A}}\tilde{\mathbf{x}} + \tilde{\mathbf{B}}\mathbf{u} & ,\tilde{\mathbf{A}} = \mathbf{T}\mathbf{A}\mathbf{T}^{-1}, \tilde{\mathbf{B}} = \mathbf{T}\mathbf{B} \\ \mathbf{y} = \tilde{\mathbf{C}}\tilde{\mathbf{x}} + \tilde{\mathbf{D}}\mathbf{u} & ,\tilde{\mathbf{C}} = \mathbf{C}\mathbf{T}^{-1}, \tilde{\mathbf{D}} = \mathbf{D} \\ \tilde{\mathbf{x}} = \mathbf{T}\mathbf{x} = \begin{bmatrix} \tilde{\mathbf{x}}_1 \\ \cdots \\ \tilde{\mathbf{x}}_2 \end{bmatrix} & \end{cases} \tag{5.18}$$

where $\tilde{\tilde{\mathbf{x}}}_1$ and $\tilde{\tilde{\mathbf{x}}}_2$ are state variables associated with significant and small Hankel singular values, respectively. The system matrices are partitioned accordingly:

$$\begin{cases} \dot{\tilde{\tilde{\mathbf{x}}}} = \begin{bmatrix} \dot{\tilde{\tilde{\mathbf{x}}}}_1 \\ \dot{\tilde{\tilde{\mathbf{x}}}}_2 \end{bmatrix} = \tilde{\tilde{\mathbf{A}}}\tilde{\tilde{\mathbf{x}}} + \tilde{\tilde{\mathbf{B}}}\mathbf{u} = \begin{bmatrix} \tilde{\tilde{\mathbf{A}}}_{11} & \tilde{\tilde{\mathbf{A}}}_{12} \\ \tilde{\tilde{\mathbf{A}}}_{21} & \tilde{\tilde{\mathbf{A}}}_{22} \end{bmatrix} \begin{bmatrix} \tilde{\tilde{\mathbf{x}}}_1 \\ \tilde{\tilde{\mathbf{x}}}_2 \end{bmatrix} + \begin{bmatrix} \tilde{\tilde{\mathbf{B}}}_1 \\ \tilde{\tilde{\mathbf{B}}}_2 \end{bmatrix} \mathbf{u} \\ \mathbf{y} = \tilde{\tilde{\mathbf{C}}}\tilde{\tilde{\mathbf{x}}} + \mathbf{D}\mathbf{u} = \begin{bmatrix} \tilde{\tilde{\mathbf{C}}}_1 & \tilde{\tilde{\mathbf{C}}}_2 \end{bmatrix} \begin{bmatrix} \tilde{\tilde{\mathbf{x}}}_1 \\ \tilde{\tilde{\mathbf{x}}}_2 \end{bmatrix} + \mathbf{D}\mathbf{u} \end{cases} \tag{5.19}$$

From this point, one can use either the state-truncation or state-residualization approach. In the state-truncation method, a reduced-order model is extracted by eliminating the state variables with small Henkel singular values, $\tilde{\tilde{\mathbf{x}}}_2$, and truncating (5.19):

$$\begin{cases} \dot{\tilde{\tilde{\mathbf{x}}}}_1 = \underbrace{\tilde{\tilde{\mathbf{A}}}_{11}}_{\mathbf{A}_r}\tilde{\tilde{\mathbf{x}}}_1 + \underbrace{\tilde{\tilde{\mathbf{B}}}_1}_{\mathbf{B}_r}\mathbf{u} \\ \mathbf{y} = \underbrace{\tilde{\tilde{\mathbf{C}}}_1}_{\mathbf{C}_r}\tilde{\tilde{\mathbf{x}}}_1 + \underbrace{\mathbf{D}}_{\mathbf{D}_r}\mathbf{u} \end{cases} \tag{5.20}$$

In the state-residualization method, the reduced-order model is extracted by setting the derivative of the state variables with small Henkel singular values, $\dot{\tilde{\tilde{\mathbf{x}}}}_2$, to zero and modifying (5.19) accordingly:

$$\begin{cases} \dot{\tilde{\tilde{\mathbf{x}}}}_1 = \underbrace{\left(\tilde{\tilde{\mathbf{A}}}_{11} - \tilde{\tilde{\mathbf{A}}}_{12}\left(\tilde{\tilde{\mathbf{A}}}_{22}\right)^{-1}\tilde{\tilde{\mathbf{A}}}_{21}\right)}_{\mathbf{A}_r}\tilde{\tilde{\mathbf{x}}}_1 + \underbrace{\left(\tilde{\tilde{\mathbf{B}}}_1 - \tilde{\tilde{\mathbf{A}}}_{12}\left(\tilde{\tilde{\mathbf{A}}}_{22}\right)^{-1}\tilde{\tilde{\mathbf{B}}}_2\right)}_{\mathbf{B}_r}\mathbf{u} \\ \mathbf{y} = \underbrace{\left(\tilde{\tilde{\mathbf{C}}}_1 - \tilde{\tilde{\mathbf{C}}}_2\left(\tilde{\tilde{\mathbf{A}}}_{22}\right)^{-1}\tilde{\tilde{\mathbf{A}}}_{21}\right)}_{\mathbf{C}_r}\tilde{\tilde{\mathbf{x}}}_1 + \underbrace{\left(\mathbf{D} - \tilde{\tilde{\mathbf{C}}}_2\left(\tilde{\tilde{\mathbf{A}}}_{22}\right)^{-1}\tilde{\tilde{\mathbf{B}}}_2\right)}_{\mathbf{D}_r}\mathbf{u} \end{cases} \tag{5.21}$$

Consider two simulation resolution levels, q_1, q_2, and the corresponding reduced models in either (5.20) or (5.21):

$$\begin{cases} \dot{\tilde{\tilde{\mathbf{x}}}}_1^{q_1} = \mathbf{A}_r^{q_1}\tilde{\tilde{\mathbf{x}}}_1^{q_1} + \mathbf{B}_r^{q_1}\mathbf{u}, \tilde{\tilde{\mathbf{x}}}^{q_1} = \mathbf{T}^{q_1}\mathbf{x}, \mathbf{x} \in \Re^n \\ \mathbf{y} = \mathbf{C}_r^{q_1}\tilde{\tilde{\mathbf{x}}}_1^{q_1} + \mathbf{D}_r^{q_1}\mathbf{u}, \tilde{\tilde{\mathbf{x}}}^{q_1} = \begin{bmatrix} \tilde{\tilde{\mathbf{x}}}_1^{q_1} \\ \tilde{\tilde{\mathbf{x}}}_2^{q_1} \end{bmatrix}, \tilde{\tilde{\mathbf{x}}}_1^{q_1} \in \Re^{q_1} \end{cases} \tag{5.22}$$

$$\begin{cases} \dot{\tilde{\mathbf{x}}}_1^{q_2} = \mathbf{A}_r^{q_2}\tilde{\mathbf{x}}_1^{q_2} + \mathbf{B}_r^{q_2}\mathbf{u}, \tilde{\mathbf{x}}^{q_2} = \mathbf{T}^{q_2}\mathbf{x}, \mathbf{x} \in \Re^n \\ \mathbf{y} = \mathbf{C}_r^{q_2}\tilde{\mathbf{x}}_1^{q_2} + \mathbf{D}_r^{q_2}\mathbf{u}, \tilde{\mathbf{x}}^{q_2} = \begin{bmatrix} \tilde{\mathbf{x}}_1^{q_2} \\ \cdots \\ \tilde{\mathbf{x}}_2^{q_2} \end{bmatrix}, \tilde{\mathbf{x}}_1^{q_2} \in \Re^{q_2} \end{cases} \tag{5.23}$$

If the simulation resolution needs to change from q_1 to q_2 at t_s, one needs to consider proper initial values for (5.23). It should be noted that the state matrices in (5.23), $\{\mathbf{A}_r^{q_2}, \mathbf{B}_r^{q_2}, \mathbf{C}_r^{q_2}, \mathbf{D}_r^{q_2}, \mathbf{T}^{q_2}\}$, are already available via either (5.20) or (5.21). First the full-order state vector at time t_s is determined from the reduced-order state vector in (5.22) and the reduction methodology

$$\mathbf{x}(t_s) = \left(\mathbf{T}^{q_1}\right)' \begin{bmatrix} \tilde{\mathbf{x}}_1^{q_1}(t_s) \\ \cdots \\ \mathbf{w}(t_s) \end{bmatrix} \tag{5.24}$$

where vector **w** depends on the reduction methodology used

$$\mathbf{w}(t_s) = \begin{cases} [0]_{q_1 \times n}, (5.20) \\ -\left(\mathbf{A}_{22}^{q_1}\right)^{-1}\mathbf{A}_{12}^{q_1}\tilde{\mathbf{x}}_1^{q_1}(t_s) - \left(\mathbf{A}_{22}^{q_1}\right)^{-1}\tilde{\mathbf{B}}_2^{q_1}\mathbf{u}, (5.21) \end{cases} \tag{5.25}$$

Once the full state vector, $\mathbf{x}(t_s)$, is found at time t_s, the reduced state vector in (5.23), $\tilde{\mathbf{x}}_1^{q_2}(t_s)$, can be initialized by applying the balancing transformation, $\mathbf{T}^{q_2}$:

$$\tilde{\mathbf{x}}^{q_2}(t_s) = \begin{bmatrix} \tilde{\mathbf{x}}_1^{q_2}(t_s) \\ \cdots \\ \tilde{\mathbf{x}}_2^{q_2}(t_s) \end{bmatrix} = \mathbf{T}^{q_2}\mathbf{x}(t_s) \tag{5.26}$$

The simulation engine proceeds with the system matrices shown in (5.23) and the initial values, $\tilde{\mathbf{x}}_1^{q_2}(t_s)$, determined according to (5.26).

5.3.3 General reduction methods

Sections (5.3.1) and (5.3.2) are suited to their specific reduction techniques. Here we develop a more general MRS framework for an arbitrary reduction scheme. The full-order model is modified to augment its state vector, **x**, in the output vector, **y**, by

$$\begin{cases} \dot{\mathbf{x}} = \mathbf{A}\mathbf{x} + \mathbf{B}\mathbf{u} \quad , \mathbf{C} = \begin{bmatrix} \mathbf{I}_n \\ \cdots \\ \hat{\mathbf{C}} \end{bmatrix} \quad , \mathbf{x} \in \Re^n \\ \mathbf{y} = \mathbf{C}\mathbf{x} + \mathbf{D}\mathbf{u} \quad , \mathbf{D} = \begin{bmatrix} 0_n \\ \cdots \\ \hat{\mathbf{D}} \end{bmatrix} \quad , \mathbf{y} = \begin{bmatrix} \mathbf{x} \\ \cdot\cdot \\ \hat{\mathbf{y}} \end{bmatrix} \end{cases} \tag{5.27}$$

where $\hat{\mathbf{C}}, \hat{\mathbf{D}}$ are the original matrices in (5.7). Consider two resolution levels, q_1, q_2, and corresponding reduced models extracted from (5.27) via any reduction method in Chapter 2:

$$\begin{cases} \dot{\mathbf{x}}_r^{q_1} = \mathbf{A}_r^{q_1}\mathbf{x}_r^{q_1} + \mathbf{B}_r^{q_1}\mathbf{u} \quad , \mathbf{x}_r^{q_1} \in \Re^{q_1} \\ \mathbf{y}^{q_1} = \mathbf{C}_r^{q_1}\mathbf{x}_r^{q_1} + \mathbf{D}_r^{q_1}\mathbf{u} \quad , \mathbf{y} = \begin{bmatrix} \hat{\mathbf{x}} \\ \cdots\cdots \\ \hat{\mathbf{y}}^{q_1} \end{bmatrix} \end{cases} \tag{5.28}$$

$$\begin{cases} \dot{\mathbf{x}}_r^{q_2} = \mathbf{A}_r^{q_2}\mathbf{x}_r^{q_2} + \mathbf{B}_r^{q_2}\mathbf{u} \quad , \mathbf{x}_r^{q_2} \in \Re^{q_2} \\ \mathbf{y}^{q_2} = \mathbf{C}_r^{q_2}\mathbf{x}_r^{q_2} + \mathbf{D}_r^{q_2}\mathbf{u} \quad , \mathbf{y} = \begin{bmatrix} \hat{\mathbf{x}} \\ \cdots\cdots \\ \hat{\mathbf{y}}^{q_2} \end{bmatrix} \end{cases} \tag{5.29}$$

By preserving the input-output response in the reduction process, the output of the reduced-order models in (5.28) and (5.29) contains an approximation of the full-order state vector, $\hat{\mathbf{x}}$. This enables the simulator engine to maneuver between different simulation resolutions by resorting to the full-order state vector and reinitiating the reduced state vector in (5.29). In particular, if the simulation resolution needs to change from q_1 to q_2 at t_s, the reduced-order system matrices are already available in (5.29). One can retrieve an approximation of the full-order vector, $\hat{\mathbf{x}}(t_s)$, from the output of (5.28) at transition time

$$\mathbf{y}^{q_1}(t_s)=\begin{bmatrix}\hat{\mathbf{x}}(t_s)\\ \cdots\cdots\\ \hat{\mathbf{y}}^{q_1}(t_s)\end{bmatrix} \tag{5.30}$$

and use that to initialize the reduced-order state model in (5.29):

$$\mathbf{x}_r^{q_2}(t_s)=\Gamma(\hat{\mathbf{x}}(t_s)) \quad ,\Gamma:\Re^n\rightarrow\Re^{q_2} \tag{5.31}$$

Operator Γ is the reduction that yields (5.29). The simulation engine can proceed after t_s with the dynamic equations in (5.29) and the initial conditions in (5.31).

5.3.4 Model verification using a boost converter

The boost converter shown in Fig. 5.2 with parameters summarized in Appendix B.1 is considered. A detailed model is constructed according to the methodology given in Section 5.2. The full-order model (5.1)–(5.11) is formulated based on the system matrices given in Appendix C.1. The eigenvalues corresponding to each topological instance (see $\mathbf{S}_j$ in (5.4) and (5.5)) in Fig. 5.2(b) are shown in Table 5.1. As indicated by large condition numbers, full-order models represent stiff differential equations, and eigenvalues cover several orders of magnitude. The model order is reduced from 8 to 2 in each topological instance. The resulting eigenvalues are shown in Table 5.2. The computational intensity is significantly reduced due to the elimination of the fast eigenvalues. The condition number of the system's state matrix (see Table 5.1 and 5.2) is also significantly improved from that of the full-order model (far exceeding 10^9) to the reduced-order model (from 10^1 to 10^5, depending on topology). It should be noted that the third topological instance ($\mathbf{S}_3$: both MOSFET and diodes are off) corresponds to the discontinuous conduction mode, and thus the model order can be further reduced to a first-order system.

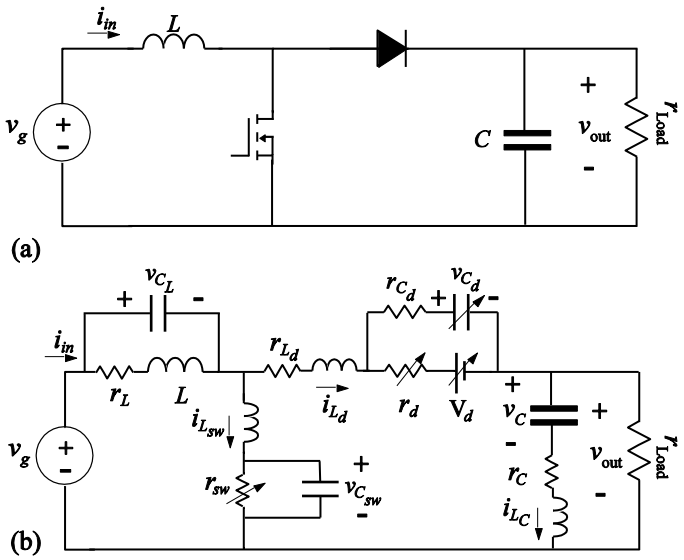

Fig. 5.2. Boost converter: (a) Circuit schematic; (b) Detailed high-order model.

TABLE 5.1
Full-order model eigenvalues and condition numbers

Switching Instance, $\mathbf{S}_j$	$\mathbf{S}_1$ MOSFET: On Diode: On	$\mathbf{S}_2$ MOSFET: On Diode: Off	$\mathbf{S}_3$ MOSFET: Off Diode: Off	$\mathbf{S}_4$ MOSFET: Off Diode: On
λ_1	-1.1×10^{11}	-1.1×10^{11}	-1.1×10^{11}	-1.1×10^{11}
λ_2	-5×10^{7} $+j\ 1.57\times10^{10}$	-4.4×10^{8} $+j\ 1.57\times10^{10}$	-4.4×10^{8} $+j\ 1.57\times10^{10}$	-4.9×10^{7} $+j\ 1.57\times10^{10}$
λ_3	-5×10^{7} $-j\ 1.57\times10^{10}$	-4.4×10^{8} $-j\ 1.57\times10^{10}$	-4.4×10^{8} $-j\ 1.57\times10^{10}$	-4.9×10^{7} $-j\ 1.57\times10^{10}$
λ_4	-2.5×10^{10}	-2.5×10^{10}	-1.1×10^{8} $+j\ 7.65\times10^{10}$	-1.32×10^{10}
λ_5	-1.32×10^{10}	-1.1×10^{8} $+j\ 6.2\times10^{8}$	-1.1×10^{8} $-j\ 7.65\times10^{10}$	-1.1×10^{8} $-j\ 7.65\times10^{10}$
λ_6	-2.45×10^{7}	-1.1×10^{8} $-j\ 6.2\times10^{8}$	-1×10^{3} $+j\ 1.6\times10^{6}$	-8.34×10^{6} $-j\ 4.46\times10^{8}$
λ_7	-256	-256	-1×10^{3} $-j\ 1.6\times10^{6}$	-1.3×10^{3} $+j\ 4\times10^{3}$
λ_8	-3.8×10^{4}	-2.2×10^{3}	-2.9×10^{3}	-1.3×10^{3} $-j\ 4\times10^{3}$
$K(\mathbf{A}_{mat})$	9.77×10^{9}	9.76×10^{9}	3.97×10^{9}	3.9×10^{9}

TABLE 5.2
Reduced-order model eigenvalues and condition numbers

Switching Instance, $\mathbf{S}_j$	$\mathbf{S}_1$ MOSFET: On Diode: On	$\mathbf{S}_2$ MOSFET: On Diode: Off	$\mathbf{S}_3$ MOSFET: Off Diode: Off	$\mathbf{S}_4$ MOSFET: Off Diode: On
$\hat{\lambda}_1$	-256	-258	-2.2×10^3	-1.3×10^3 $+j4\times10^3$
$\hat{\lambda}_2$	-3.8×10^4	-2.2×10^3	-1.6×10^9	-1.3×10^3 $-j4\times10^3$
$K(\mathbf{A}_{mat})$	155	8.5	7.5×10^5 (2^{nd} order) 1 (1^{st} order)	-4.9×10^7 $-j\ 1.57\times10^{10}$

To verify the order-reduction process, several transfer functions from the input voltage to the original state variables of the detailed model are considered in several topological instances. Corresponding transfer functions from the input voltage to the "pseudo-full-order" state variables ($\hat{\mathbf{x}}$ in (5.28) and (5.29)), projected by the reduced-order model outputs, are also considered. As seen in Figs. 5.3–5.6, the reduced-order models closely resemble the frequency-domain characteristics of the full-order models within the frequency range of interest (up to ten times the switching frequency). Different levels of accuracy and/or bandwidths are achievable by adjusting the model order.

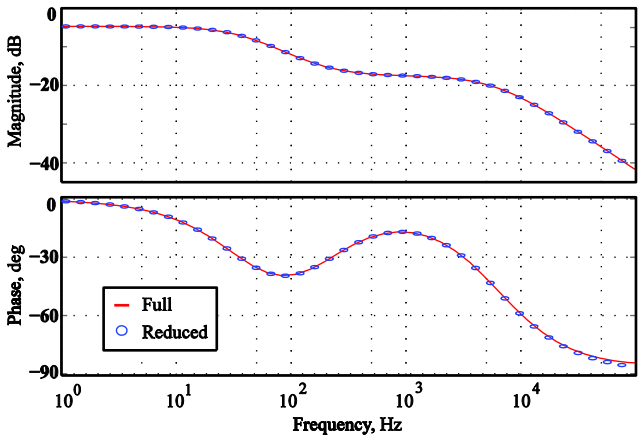

Fig. 5.3. Audio susceptibility transfer functions, $\hat{v}_{out}(s)/\hat{v}_g(s)$, in the first topological instance, $\mathbf{S}_1$.

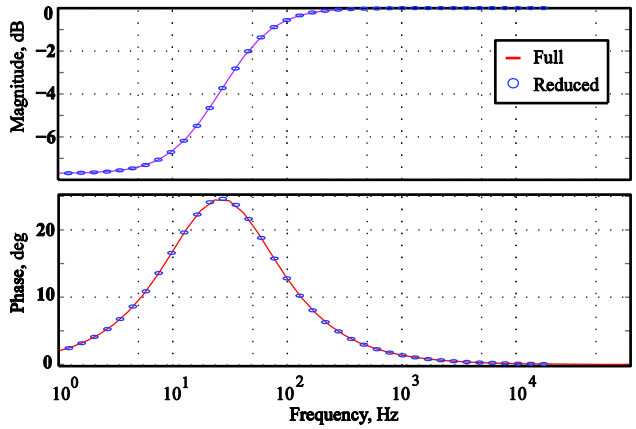

Fig. 5.4. Input voltage to inductor voltage transfer functions, $\hat{v}_{C_L}(s)/\hat{v}_g(s)$, in the second topological instances, $\mathbf{S}_2$.

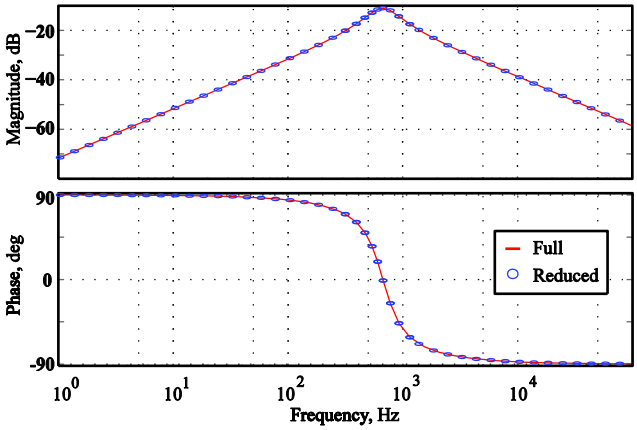

Fig. 5.5. Input voltage to capacitor current transfer functions, $\hat{i}_{L_C}(s)/\hat{v}_g(s)$, in the fourth topological instance, $\mathbf{S}_4$.

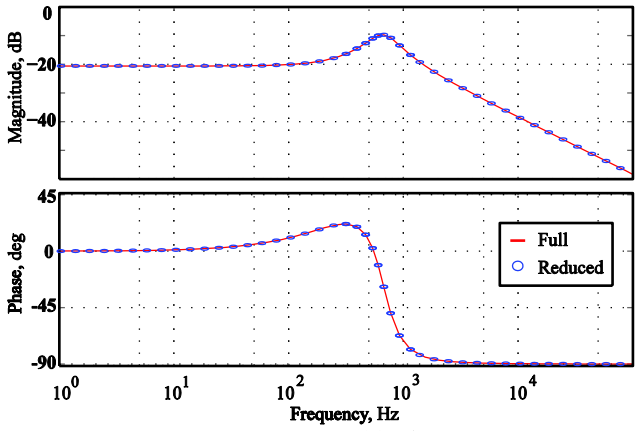

Fig. 5.6. Input voltage to diode current transfer functions, $\hat{i}_{L_d}(s)/\hat{v}_g(s)$, in the fourth topological instance, $\mathbf{S}_4$.

Next, a large-signal time-domain transient of the boost converter with a 50% duty cycle is considered. The computer simulations are carried out using Matlab/Simulink run on a personal computer with a T7700 Intel Core2 Duo processor (2.4 GHz). To achieve numerical stability and accuracy, a variable step-size solver, ODE23tb [245], is considered for both simulation resolutions with a maximum allowable step size of 10^{-4} seconds. The steady state of the converter is reached in 5×10^{-4} seconds of simulation time. The full resolution simulation takes 205.23 seconds of CPU time and 326514 time steps. Alternatively, the low resolution simulation takes only 0.48 seconds and requires only 332 time steps. This demonstrates approximately two orders of magnitude improvement in simulation speed and three orders of magnitude reduction of time steps. It should be noted that the factor by which the simulation is accelerated is case dependent, but a very significant improvement can be expected in general.

The corresponding system waveforms, for two switching cycles in steady state, are shown in Figs. 5.7 – 5.11. The hardware measurements (a) are used to verify the high-fidelity full-order model (b) which, in turn, is used to verify the reduced-order model (c). The ringing, reverse recovery effects, switching edge transients, and high-frequency dynamics of the high-order model are absent in the low-resolution simulation, while the overall long-term behaviors are successfully captured. Finally, a similar study is conducted using an MRS environment (d). The simulation startup is conducted using the low-order model to reach steady state. Then, to study the switching transients, the system resolution is increased in the middle of a switching cycle (shown darker in Figs. 5.7–5.11, (d)). The pseudo-full-state vector, $\hat{\mathbf{x}}$, projected by the reduced-order model in (5.28), is fed as the initial condition to the full-order model in (5.29). Thus, the need to run the entire high-order model to reach steady state is eliminated. As seen in Figs. 5.7-5.11, the MRS employs both low- and high-order models accurately. While the overall long-term

behavior is precisely captured by the low-resolution simulation of the proposed multiresolution model, the high-resolution simulation part successfully predicts the fast dynamics as verified in comparison with the detailed model and hardware measurements.

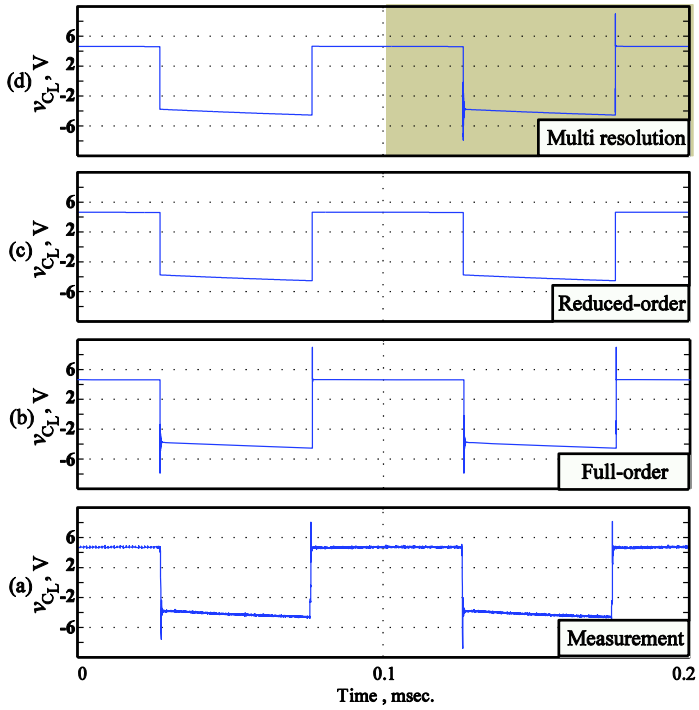

Fig. 5.7. Inductor voltage, $v_{C_L}(t)$, waveforms extracted from hardware measurements, predicted by the reduced- and full-order models, and resulting from MRS.

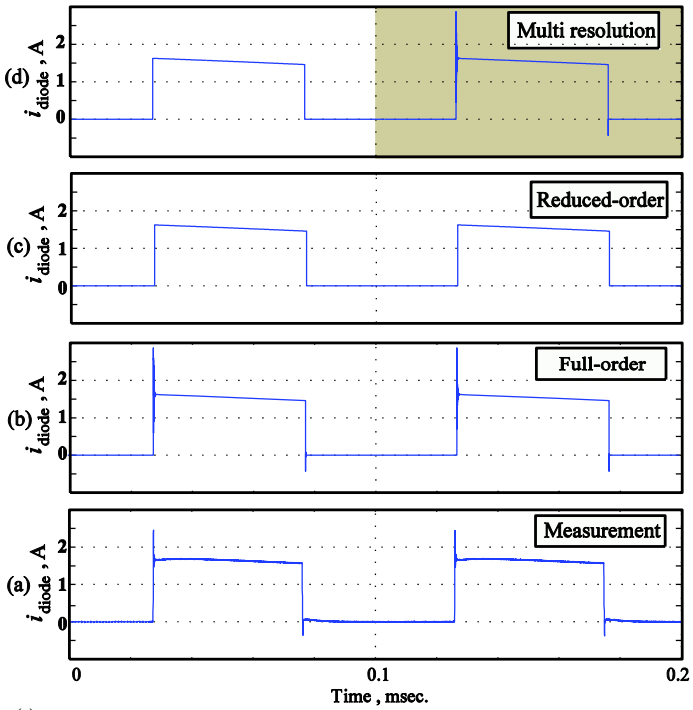

Fig. 5.8. Diode current, $i_{L_d}(t)$, waveforms extracted from hardware measurements, predicted by the reduced- and full-order models, and resulting from MRS.

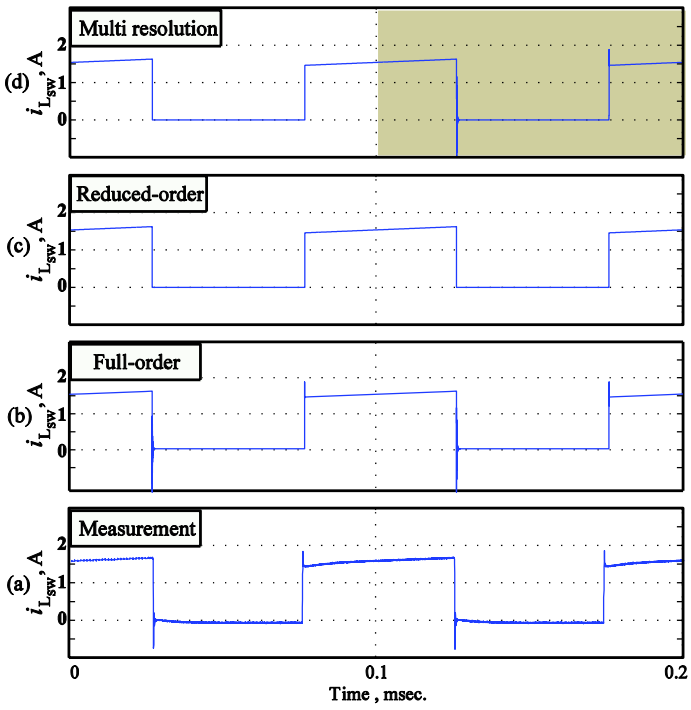

Fig. 5.9. MOSFET current, $i_{L_{sw}}(t)$, waveforms extracted from hardware measurements, predicted by the reduced- and full-order models, and resulting from MRS.

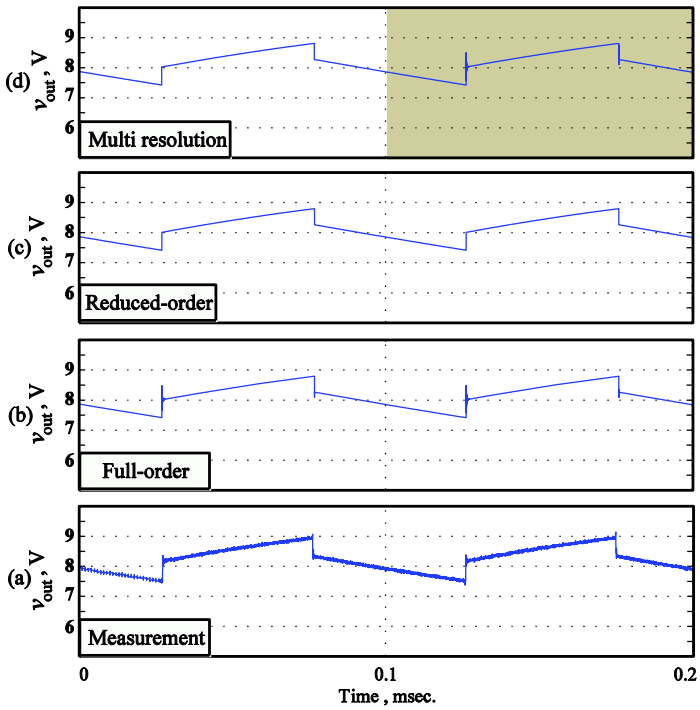

Fig. 5.10. Output voltage, $v_{out}(t)$, waveforms extracted from hardware measurements, predicted by the reduced- and full-order models, and resulting from MRS.

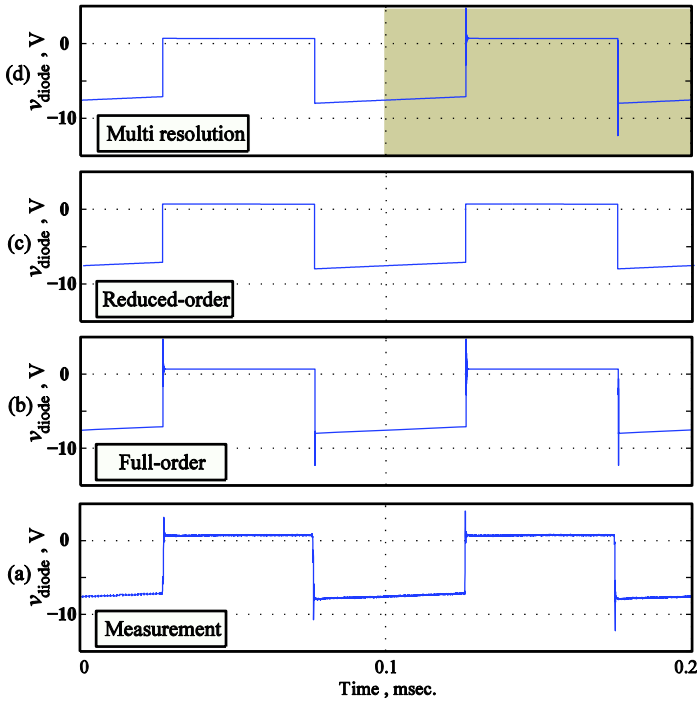

Fig. 5.11. Diode voltage, $v_g(t) - v_{C_L}(t) - v_{out}(t)$, waveforms extracted from hardware measurement, predicted by the reduced- and full-order models, and resulting from MRS.

5.3.5 Model verification using a class-E amplifier

A 4 MHz, Class-E amplifier shown in Fig. 5.12 with parameters summarized in Appendix B.2 is considered. The amplifier is in an off-nominal, zero-voltage switching mode of operation. The design procedure for resonant operation of Class-E amplifiers has been discussed in the literature (e.g., [246-249]). The full-order model is established based on the 10^{th}-order circuit representation in Fig. 5.12(b). This is a single-switch system, and there are two possible topological instances ($\mathbf{S}_1$,$\mathbf{S}_2$). System eigenvalues for both instances are shown in Fig. 5.13, which indicates that eigenvalues span a wide frequency range (ten orders of magnitude). Several model orders (6^{th}, 4^{th}, and 2^{nd}) and corresponding MRS environments are developed according to methodologies set forth in Section 5.3. As the simulation speed and accuracy are directly related to the fastest eigenvalue and system condition number, respectively, corresponding parameters are shown in Table 5.3 for each model order.

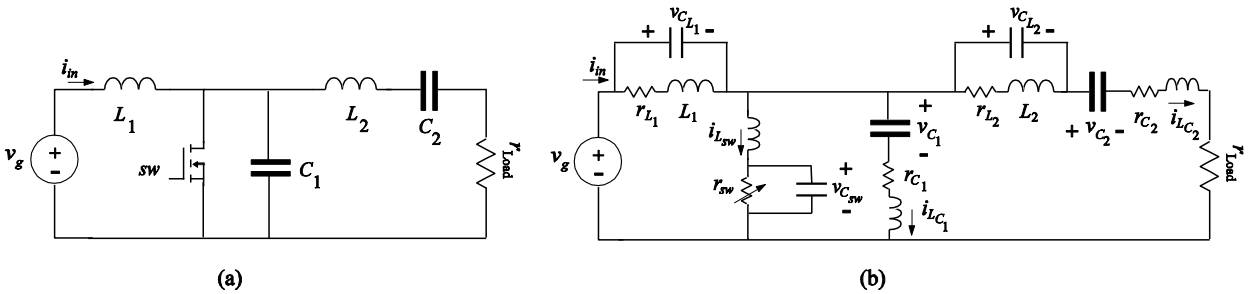

Fig. 5.12. Class-E amplifier: (a) Circuit schematic; (b) Detailed high-order representation.

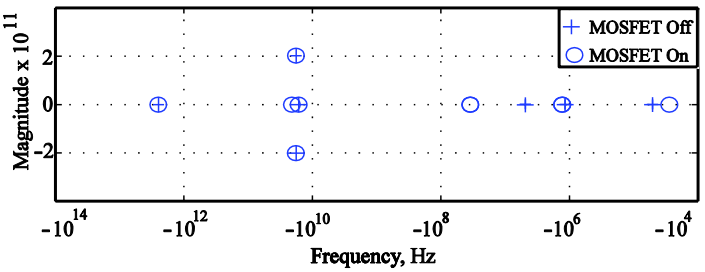

Fig. 5.13. System eigenvalues for both topological instances (on and off states of the MOSFET).

TABLE 5.3
Fastest eigenvalues and condition numbers for different model orders

	Fastest Eigen-value	Condition Number
Full(10^{th})-order Model MOSFET: On	-2.49×10^{12}	1.7×10^{8}
Full(10^{th})-order Model MOSFET: Off	-2.49×10^{12}	1.12×10^{8}
6^{th}-order Model MOSFET: On	-2.1×10^{10}	1.5×10^{6}
6^{th}-order Model MOSFET: Off	-1.21×10^{9}	4.84×10^{5}
4^{h}-order Model MOSFET: On	-3.23×10^{9}	2×10^{5}
4^{th}-order Model MOSFET: Off	-3.26×10^{7}	1.2×10^{5}
2^{nd}-order Model MOSFET: On	-3.23×10^{9}	1.6×10^{5}
2^{nd} -order Model MOSFET: Off	-1×10^{7}	4.95×10^{4}

The startup transients are considered for each simulation resolution. The same computational platforms and ODE solver algorithms as in Section 5.3.4 are used. The maximum allowable step size is set to 10^{-7} second, and the relative error tolerance is set to 10^{-4}. Steady-state operation is reached in 15 μs simulation time. Table 5.4 summarizes the actual CPU times and number of integration steps used in different simulation resolutions. As expected, both a significant improvement in simulation speed and noticeable reduction in the number of integration steps are observed as the model order is reduced.

TABLE 5.4
Transient simulation CPU times and integration steps for different model orders

	Elapsed CPU Time	Number of Integration Steps
Full(10^{th})-order Model	74 s	73000
MRS	68.5 s	36630
6^{th}-order Model	71 s	67000
4^{th}-order Model	5.8 s	5260
2^{nd}-order Model	3.2 s	2255

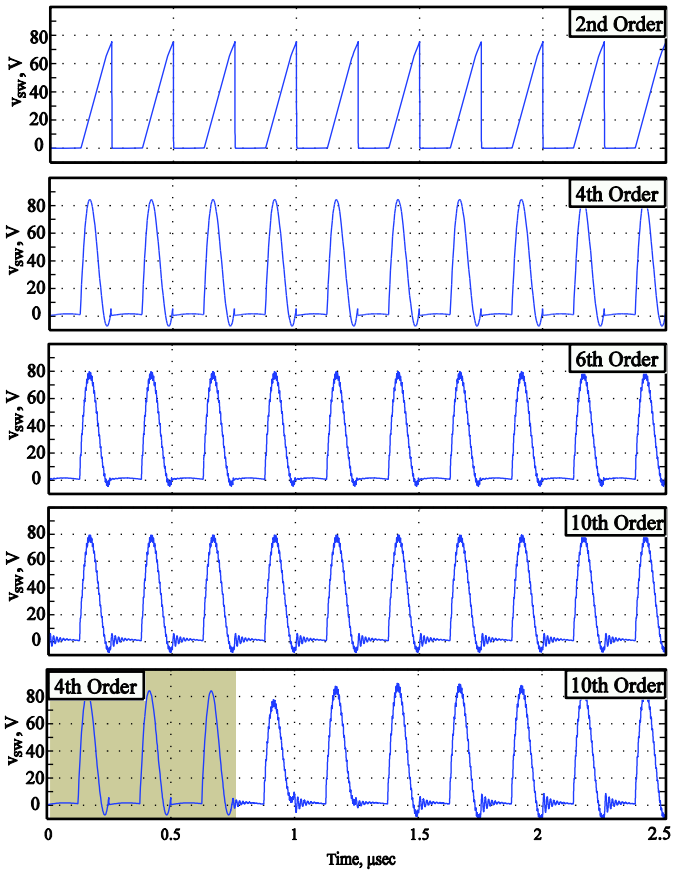

Fig. 5.14. MOSFET voltage waveforms in different simulation resolutions as well as MRS environment.

The MOSFET voltage waveforms for the respective simulation resolutions are shown in Fig. 5.14 for the amplifier in steady state. As the model order and, subsequently, the simulation resolution increases, higher frequency dynamics (ringing, switching edges, etc.) are more apparent in the transient waveforms. This is expected given the distribution of dynamic modes in Fig 5.13. In particular, the MOSFET voltage waveform for the full (10^{th})-order model shows an acceptable match with the experimental results in the literature (refer to Fig. 20 in [246]).

Finally, a similar study is conducted in an MRS environment (see the bottom plot). The simulation resolution is increased from a 4^{th}-order model to a 10^{th}-order model at t_s=0.74 μs. The change in the simulation resolution occurs in the middle of a switching transient, where some

fast dynamics have not yet subsided. As seen in Fig. 5.14, the MRS employs both 4^{th}- and 10^{th}-order models successfully.

5.4 MRS of Cascaded Switching Converters

5.4.1 Conceptual framework

Multi-converter systems, e.g., cascaded converters, are commonly found in power electronics applications. MRS can be implemented modularly, where each converter is independently simulated with arbitrary resolution and communicates with other converters using exchange variables (see y_1 and y_2 in Fig. 5.15). To facilitate that, the exchange variable is formulated in the output vector of the source converter, and in the input vector of the destination converter. Since the order-reduction procedure preserves the input-output relationship, the output vectors of reduced-order source converters include an approximation of exchange variables (y_1^*, y_2^* in Fig. 5.15). These variables are then fed into the reduced-order models of the respective destination converters as input variables. As opposed to the existing nested simulations, this approach does not require adaptive algorithms for communication or synchronization.

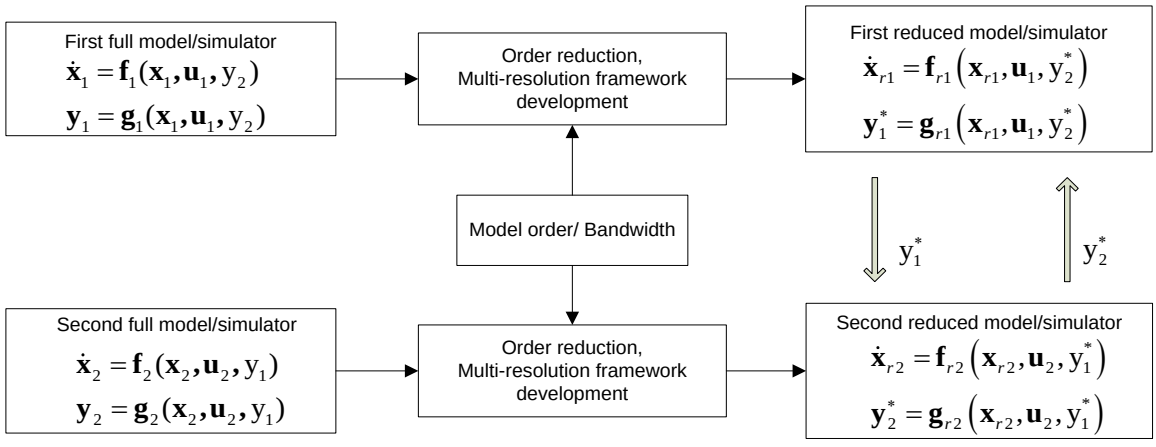

Fig. 5.15. Modular MRS framework.

5.4.2 Model verification

A cascaded boost/buck-boost converter system is considered in Fig. 5.16. Model parameters are summarized in Appendix B.3 and system matrices for both converters are given in Appendix C.3. Each converter is modeled in full as a 7^{th}-order system. The model order of each converter is reduced from 7 to 2. The fastest eigenvalue and condition numbers in each topological instance of boost and buck-boost converters are shown in Table 5.5 and Table 5.6, respectively. As expected, the condition number has improved and the fastest eigenvalue is significantly slower for the reduced-order models.

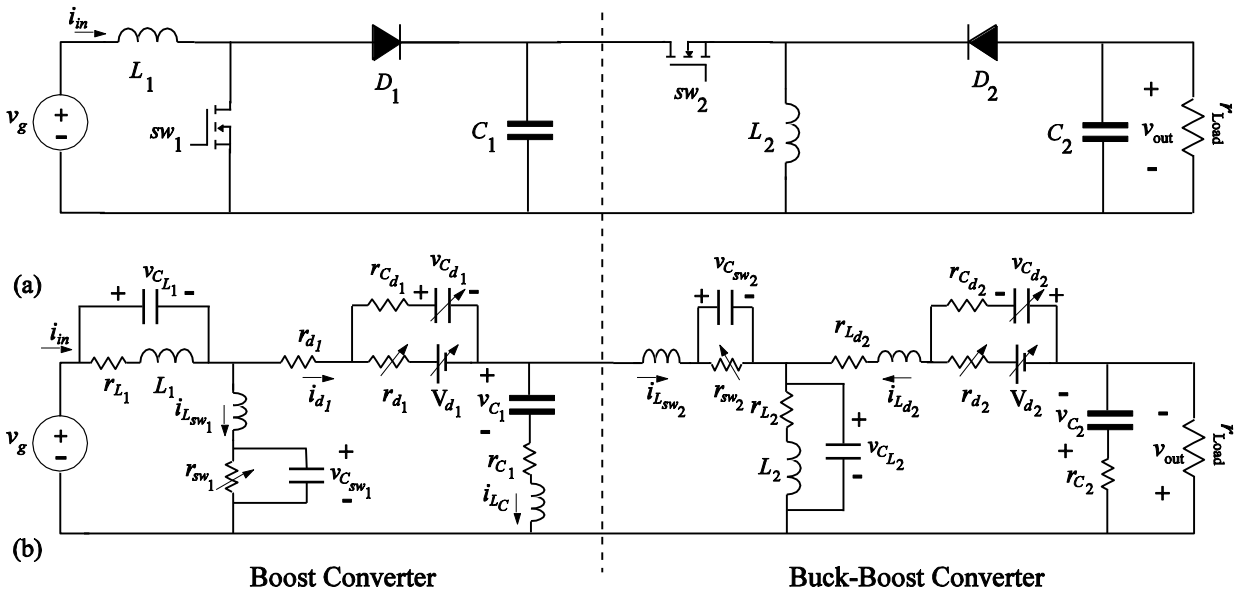

Fig. 5.16. Cascaded boost/buck-boost converter system: (a) Circuit schematic; (b) High-fidelity model representation.

TABLE 5.5
Fastest eigenvalues and condition numbers for the full- and reduced-order models of the boost converter

	Fastest Eigenvalue	Condition Number
Full-order Boost Model MOSFET : On , Diode: On	-4.999×10^{9}	3.82×10^{8}
Full-order Boost Model MOSFET : On , Diode: Off	-4.999×10^{9}	6.82×10^{12}
Full-order Boost Model MOSFET : Off , Diode: Off	$-1.64\times10^{8}\pm j5.266\times10^{8}$	2.4×10^{12}
Full-order Boost Model MOSFET : Off , Diode: On	-2.73×10^{9}	1.21×10^{7}
Reduced-order Boost Model MOSFET : On , Diode: On	-18.52	967
Reduced-order Boost Model MOSFET : On , Diode: Off	-18.52	1.78×10^{4}
Reduced -order Boost Model MOSFET : Off , Diode: Off	-1×10^{-3} (1^{st} order) -3.1×10^{9} (2^{nd} order)	1 (1^{st} order) 2.97×10^{12} (2^{nd} order)
Reduced -order Boost Model MOSFET : Off , Diode: On	$-1.34\times10^{2}\pm j2.19\times10^{3}$	22.5

TABLE 5.6
Fastest eigenvalues and condition numbers for the full- and reduced-order models of the buck-boost converter

	Fastest Eigenvalue	Condition Number
Full-order Buck-boost Model MOSFET : On , Diode: On	-4.99×10^{9}	8×10^{8}
Full-order Buck-boost Model MOSFET : On , Diode: Off	-4.99×10^{9}	8×10^{8}
Full-order Buck-boost Model MOSFET : Off , Diode: Off	-1.35×10^{8}	3.52×10^{6}
Full-order Buck-boost Model MOSFET : Off , Diode: On	-2.99×10^{9}	5.97×10^{7}
Reduced-order Buck-boost Model MOSFET : On , Diode: On	-163	19
Reduced-order Buck-boost Model MOSFET : On , Diode: Off	-162	18.3
Reduced -order Buck-boost Model MOSFET : Off , Diode: Off	-162 (1^{st} order) -1.48×10^{9}	1 (1^{st} order) 9.1×10^{6} (2^{nd} order)
Reduced -order Buck-boost Model MOSFET : Off , Diode: On	-152	4

To verify the efficacy of the modular MRS framework, a 1 ms startup transient of the cascaded system is considered. The same computational platform and ODE solver setup as in Section 5.3.4 is used. Four possible combinations of model orders (mixture of full or reduced-order models of

either converter) are considered. To avoid an algebraic loop in the "reduced-reduced" combination, data exchange between individual reduced-order blocks is facilitated using sample-and-hold that introduces extra time delay. Despite this, two orders of magnitude increments in simulation speed, and an order of magnitude reduction in the number of integration steps are reported in Table 5.7.

TABLE 5.7
Transient simulation CPU times and integration steps for modular combination of model orders

	Simulation Run Time	Number of Integration steps
Full-order Boost Model Full-order Buck-boost Model	212 s	115000
Full-order Boost Model Reduced-order Buck-boost Model	142 s	78400
Reduced-order Boost Model Full-order Buck-boost Model	120 s	65440
Reduced-order Boost Model Reduced-order Buck-boost Model	15 s	10200

The MOSFET voltage waveform of the boost converter is shown in Fig. 5.17 for different simulation resolution combinations. When labeling plots in Fig. 5.17, the first model-order/simulation-resolution refers to that of the boost converter. First, the experimental results (a) are used to verify that the "full-full" combination ((b), both boost and buck-boost converters are represented by full-order models) accurately resembles existing hardware setup. It should be noted that those converters have different switching frequencies ($f_{sw,boost}$ = 50 kHz and $f_{sw,buck\text{-}boost}$ = 30 kHz), and thus it is hard to match all the switching spikes of the measurement snapshots with simulations. In the remaining plots ((c) "full-reduced," (d) "reduced-full," and (e), (f) "reduced-reduced" combinations), the higher frequency dynamics are absent in the reduced-order representation of the corresponding converter, while the overall waveform behaviors are accurately portrayed.

In the proposed modular MRS framework (see Fig. 5.17 (f)), both converters are first simulated at low resolutions. At t = 25 μs, the boost converter simulation resolution is increased while the buck-boost converter is still in a lower resolution mode (shown darker in the bottom plot of Fig. 5.17). Finally, at t = 55 μs, both converter simulation resolutions are switched to higher resolution modes and the simulation proceeds. As verified with the original resolution combinations in Fig. 5.17, the modular MRS framework accurately portrays the underlying cascaded converter dynamics for arbitrary resolution levels.

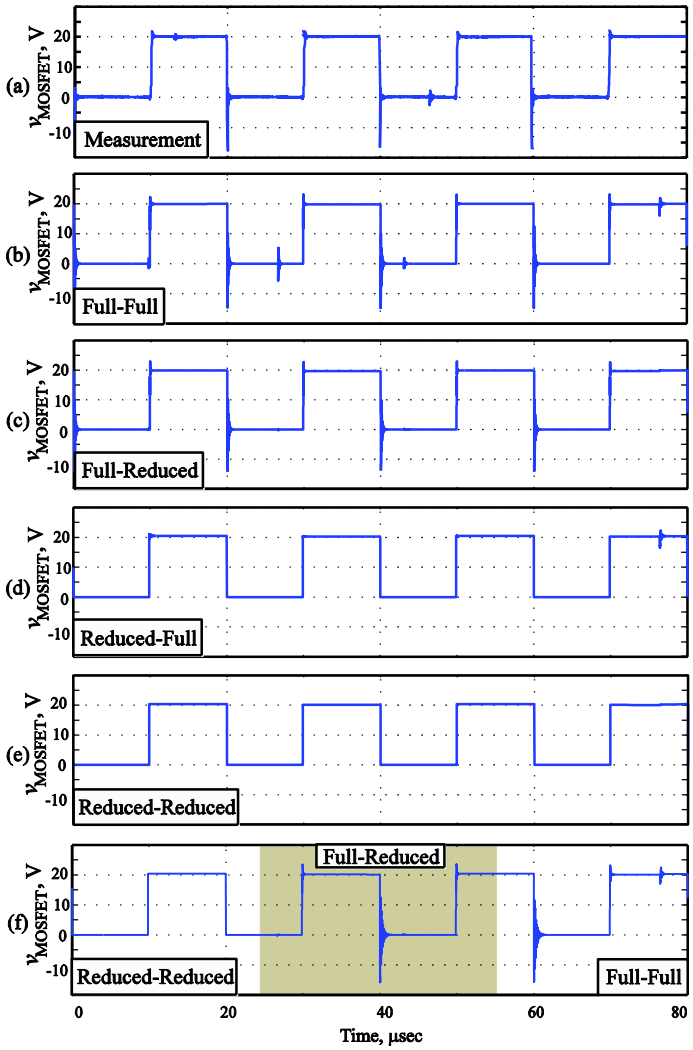

Fig. 5.17. MOSFET voltage waveforms for different combinations of model order and resulting modular simulation resolutions, as well as a modular MRS environment.

To demonstrate the effect of appropriate initialization when the resolution changes, an MRS study is considered in Fig. 5.18. The boost converter is in high resolution mode and the resolution of the buck-boost converter changes from low to high at t = 20 μs. Figure 5.18(a) shows an accurate initialization of the buck-boost converter at higher resolution, according to the methodology in Section 5.3. In Fig. 5.18(b), the final values of the state vector in the boost converter model are *intentionally* used to initialize the buck-boost converter model in high-resolution mode. Although the dynamic equations of the buck-boost converter in the higher resolution mode are correct, the wrong initialization process leads to a 5 V offset in the MOSFET voltage waveform in steady state (Fig. 5.18(b) compared to Fig. 5.18(a)). This demonstrates the importance of appropriate initialization of the new simulation resolution.

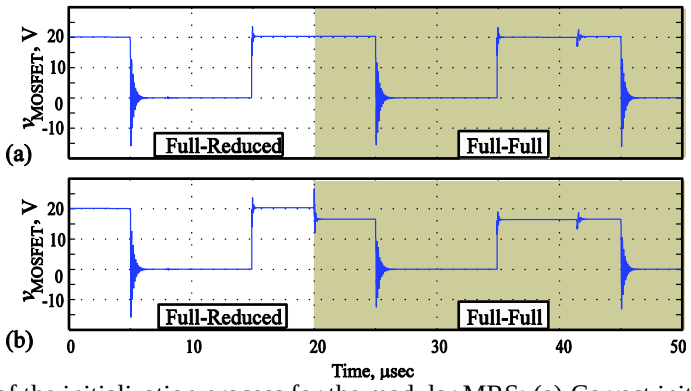

Fig. 5.18. Demonstration of the initialization process for the modular MRS; (a) Correct initializations; (b) Incorrect initialization.

5.5 MRS of Switching Converters with Nonlinear Components

5.5.1 Conceptual framework

Switching converters are often described with nonlinear equations (5.6) due to the presence of magnetic saturation. A general framework for MRS of nonlinear systems is shown in Fig. 5.19. First, the nonlinear full-order system is represented as a piecewise-linear model. The output vector of the full-order model, **y**, is augmented to include the full-order state vector, $\mathbf{x}_f$. Since the

order reduction preserves the input-output relationship, the output of the reduced-order model approximates the state vector of the full-order model, $\mathbf{x}_f^*$. This estimation, $\mathbf{x}_f^*$, is then used to select the appropriate subinterval, *k*. The final model is a dual-nested switched linear system with two event detections. One is indicated by *k* in Fig. 5.19 that represents the structural change caused by the existing switching components. Another, indicated by *j* in Fig. 5.19, points to an appropriate linear segment within the k^{th} structural interval.

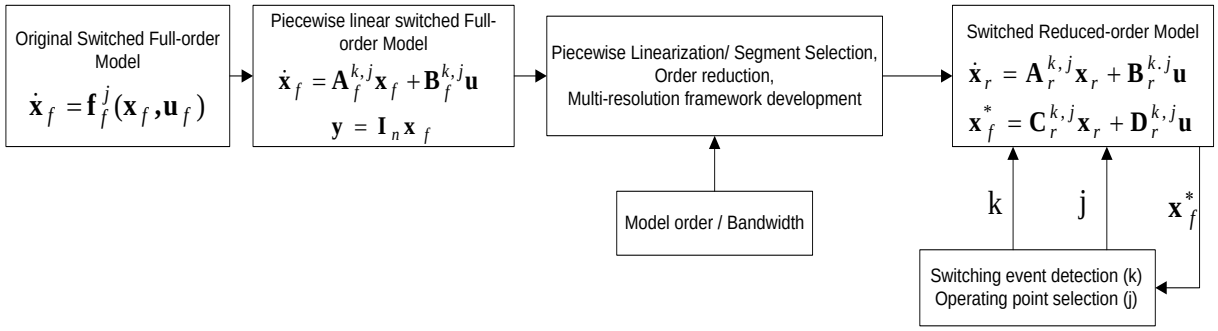

Fig. 5.19 Nonlinear MRS diagram.

5.5.2 Piecewise representation of saturated inductors

The nonlinear flux linkage-current relationship incorporates saturation effects (Fig 5.20(a)). The effective inductance is defined as the slope of the flux-linkage current curve $(\lambda - i)$ at the desired inductor current. Typical nonlinear $\lambda - i$ relationships of power magnetic cores can be accurately replaced with several constant inductors corresponding to different current profiles:

$$L_{eff} = \partial\lambda / \partial i \approx L_k, i \in \left[\mathrm{I}_{\mathrm{tr}_{k-1}}, \mathrm{I}_{\mathrm{tr}_k}\right] \tag{5.32}$$

This concept is shown in Fig. 5.20(a), where the nonlinear inductor is approximated with three effective inductances $L_{eff_1}, L_{eff_2}, L_{eff_3}$ using two current thresholds, $\mathrm{I}_{tr_1}, \mathrm{I}_{tr_2}$. The nonlinear inductor is presented as a current-controlled switched combination of linear inductors (Fig. 5.20(b)). Thus, the original nonlinear system in (5.6) is replaced with a switched linear system

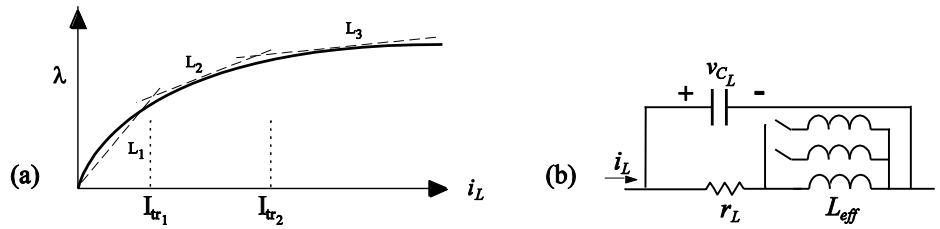

Fig. 5.20. Piecewise linear representation of a saturated inductor: (a) Flux linkage-current relationship; (b) Current-dependent switched representation of the nonlinear inductor.

$$\begin{cases} \dot{\mathbf{x}} = \mathbf{A}^{k,j}\mathbf{x} + \mathbf{B}^{k,j}\mathbf{u} \quad k = 1\cdots p,\ j = 1\cdots 3 \\ \mathbf{y} = \mathbf{C}^{k,j}\mathbf{x} + \mathbf{D}^{k,j}\mathbf{u} \end{cases} \tag{5.33}$$

where $\left\{\mathbf{A}^{k,j}, \mathbf{B}^{k,j}, \mathbf{C}^{k,j}, \mathbf{D}^{k,j}\right\}$ are system matrices. The set $\{k, j\}$ defines a combinational topological instance, where k is determined by the switching logics in (5.1)–(5.3) and (5.9), and j is determined by the inductor current magnitude and refers to the topological subinterval due to the switched-linear representation of the nonlinear inductor in (5.32) and Fig. 5.20(b).

5.5.3 Order reduction and MRS framework development

The Krylov-subspace methods [79] are used to extract several reduced-order models and respective simulation resolutions. For each topological instance $\{k, j\}$, an orthonormal projection matrix, $\mathbf{W}^{k,j}$, is generated from a q^{th}-order Krylov subspace of system matrices:

$$\mathbf{K}_q\left(\left(\mathbf{A}^{k,j}\right)^{-1}, \mathbf{B}^{k,j}\right) = Span\left\{\mathbf{B}^{k,j}, \left(\mathbf{A}^{k,j}\right)^{-1}\mathbf{B}^{k,j}, \cdots, \left(\left(\mathbf{A}^{k,j}\right)^{-1}\right)^{q-1}\mathbf{B}^{k,j}\right\} \tag{5.34}$$

using the Arnoldi method. Order $q < n$, and n is the original system order. The reduced system matrices, $\left\{\mathbf{A}_r^{k,j}, \mathbf{B}_r^{k,j}, \mathbf{C}_r^{k,j}, \mathbf{D}_r^{k,j}\right\}$, are extracted by applying the projection matix, $\mathbf{W}^{k,j}$, to the original state matrices in (5.33):

$$\begin{cases} \dot{\mathbf{z}} = \mathbf{W}^{k,j}\mathbf{A}^{k,j}\left(\mathbf{W}^{k,j}\right)'\mathbf{z} + \mathbf{W}^{k,j}\mathbf{B}^{k,j}\mathbf{u} = \mathbf{A}_r^{k,j}\mathbf{z} + \mathbf{B}_r^{k,j}\mathbf{u} \\ \mathbf{y} = \mathbf{C}^{k,j}\left(\mathbf{W}^{k,j}\right)'\mathbf{z} + \mathbf{D}^{k,j}\mathbf{u} = \mathbf{C}_r^{k,j}\mathbf{z} + \mathbf{D}_r^{k,j}\mathbf{u} \end{cases} \tag{5.35}$$

As the full-order state vector, **x**, is projected into a lower order state vector, **z**, by a similarity transform:

$$\mathbf{z} = \mathbf{W}^{k,j}\mathbf{x},\ \mathbf{x} \in \Re^n,\ \mathbf{z} \in \Re^q,\ \mathbf{W}^{k,j} \in \Re^{n\times q} \tag{5.36}$$

Equations (5.35) and (5.36) define the new reduced-order (q^{th}-order) model.

Since the order-reduction process in (5.35) preserves the input-output response (while reducing the system dimension), the output of any reduced order model in (5.35) contains an approximation of the original state vector, $\mathbf{x}_f^*$. This "psudo-state vector" is used to determine the switching in (5.1)–(5.3) and (5.9), and the effective inductance value in Fig. 5.20(b), thus obtaining the topological instance set $\{k, j\}$.

When switching between any two arbitrary resolution levels, q_1, q_2, at time t_s, the projection matrix, $\mathbf{W}_{q_1}^{k,j}$, used in the reduction process in (5.35), is replaced with a new-order projection matrix, $\mathbf{W}_{q_2}^{k,j}$. Moreover, the initial values of the new resolution state vector, $\mathbf{x}_{q_2}(t_s)$, are obtained from the previous resolution state variables, $\mathbf{x}_{q_1}(t_s)$:

$$\mathbf{x}_{q_2}(t_s) = \mathbf{W}_{q_2}^{k,j}\left(\mathbf{W}_{q_1}^{k,j}\right)'\mathbf{x}_{q_1}(t_s) \tag{5.37}$$

5.5.4 Model verification

The boost converter shown in Fig. 5.21, with parameters summarized in Appendix B.4, is considered. The model order is reduced from eight to two in each topological instance based on

the switching state and effective inductance value. The computational intensity is significantly reduced due to the elimination of the fast eigenvalues (exceeding 10^{11} in the full-order model). The condition number of the system's state matrix is also significantly improved from those of the full-order model (exceeding 10^{9}) to the reduced-order models (around 10^{2}).

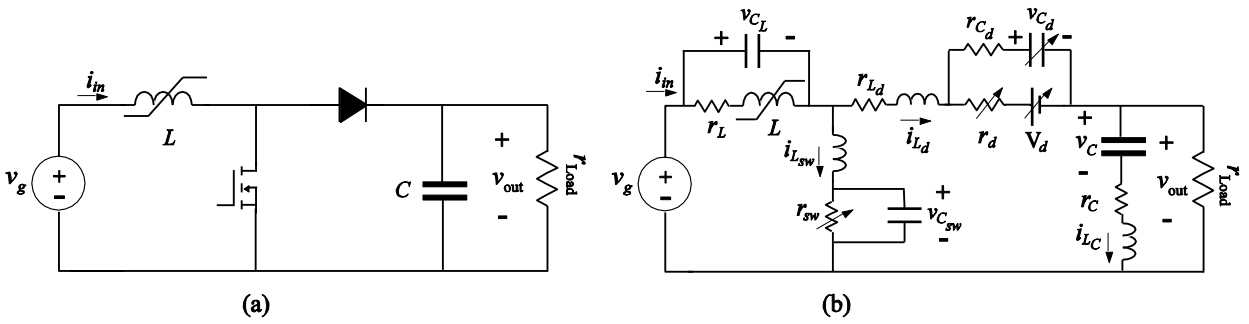

Fig. 5.21. High-fidelity model of a boost converter with a nonlinear inductor: (a) Circuit schematic; (b) Detailed high-order model.

To verify the order-reduction procedure, the transfer functions from the input voltage to the diode current are considered for both full-order and several reduced-order models. In the example topological instance, the MOSFET is on, the diode is off, and the inductor is in the first piecewise linear region $(k, j) = (2,1)$. As seen in Fig. 5.22, the 2nd-order models closely resemble the frequency-domain characteristics of the full-order models within the lower frequency range (up to 10 MHz). Higher order models can be utilized to achieve more fidelity in a higher frequency range. For example, as shown in Fig. 5.23, 4th-order and 6th-order models can accurately represent the dynamic characteristics up to 100 MHz and 10 GHz, respectively.

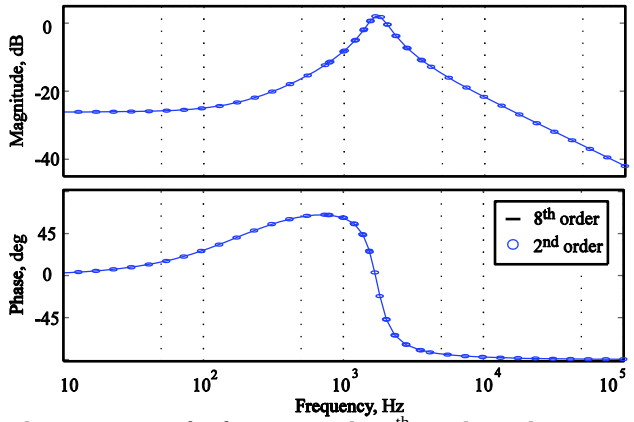

Fig. 5.22. Input voltage to diode current transfer function in the 4th topological instance and first inductor region (lower frequency range).

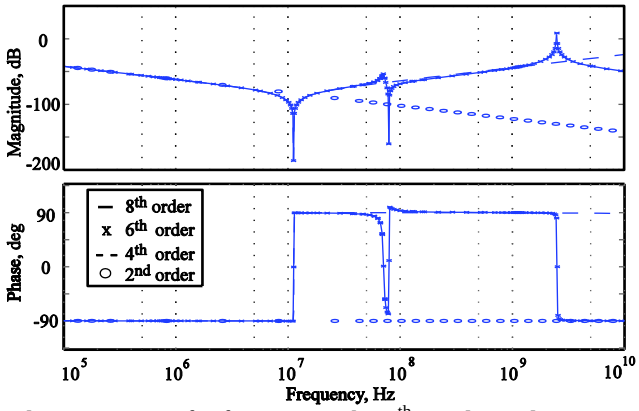

Fig. 5.23. Input voltage to diode current transfer function in the 4th topological instance and first inductor region (higher frequency range).

Next, a 1 ms setup transient of the boost converter with a 50% duty is considered. Similar computational platform and ODE solver settings are used. The full resolution simulation takes 386 seconds of CPU time and 332,585 time steps. Alternatively, the low-resolution simulation of the reduced 2nd-order model takes only 11 seconds and requires only 1,356 time steps. This demonstrates orders of magnitude improvement in simulation speed and reduction in the number of time steps.

The inductor current shown in Fig. 5.24 clearly indicates saturation. The MOSFET and diode currents for two switching cycles in steady state are shown in Figs. 5.25 and 5.26, respectively. The simulation resolution is increased at t_s = 20 ms in the middle of a switching cycle (shown

darker in Figs. 5.25 and 5.26). While the overall long-term behavior is precisely captured by the low-resolution mode of the proposed MRS, the high-resolution simulation part successfully predicts the fast dynamics.

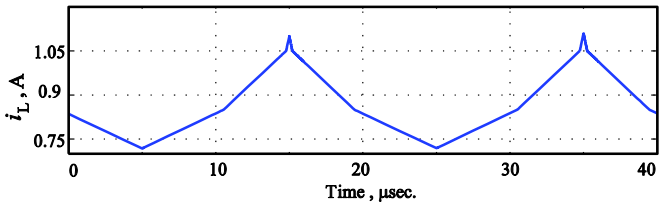

Fig. 5.24 Inductor current indicating saturation.

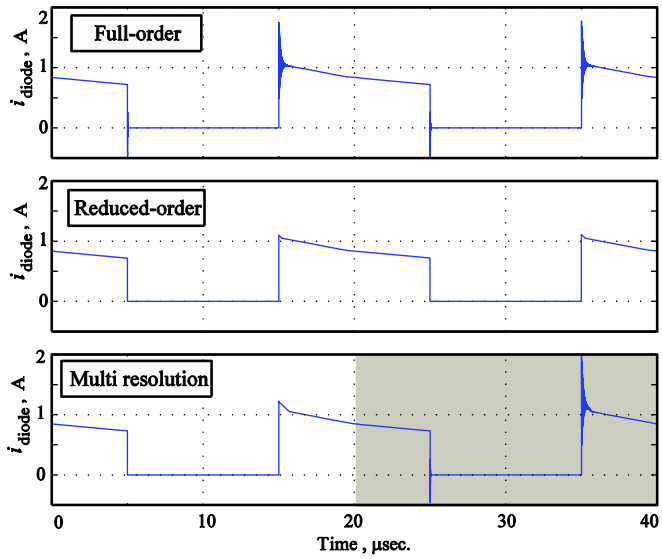

Fig. 5.25 Diode current waveforms predicted by the reduced- and full-order models, and resulted from MRS.

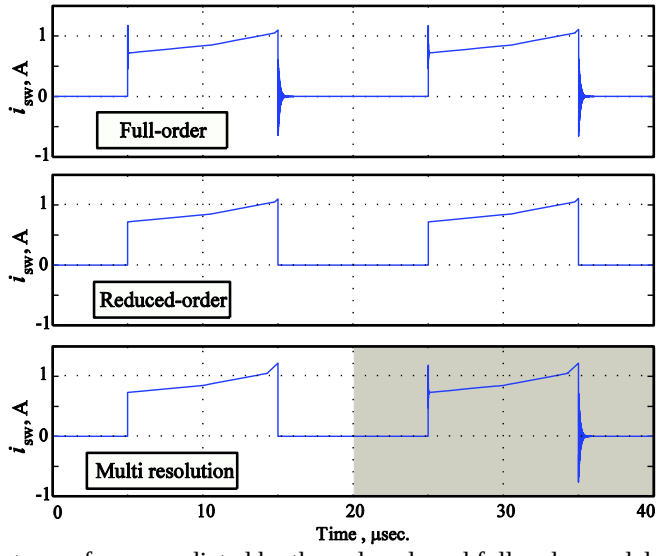

Fig. 5.26 MOSFET current waveforms predicted by the reduced- and full-order models, and resulted from MRS.

5.6 MRS of Controlled Switching Converters

5.6.1 Conceptual framework

Switching converters require feedback and feedforward control loops to regulate the output voltage or the input current. The full-order state feedback determines the switching timing in (5.9). The candidate MRS environment is shown in Fig 5.27. The pseudo-full-order state vector, $\mathbf{x}_f^*$, is retrieved from the reduced-order model and is fed into the controller which, in turn, determines the topological instance, $\mathbf{S}_j$, (switching state j in Fig. 5.27) and adopts the corresponding reduced-order model. It should be noted that the controller bandwidth is typically less than the converter's cut-off frequency (and implicitly the fast dynamics within each topological instance). Thus, incorporating the controller dynamics should not affect the order-reduction process and MRS environment development.

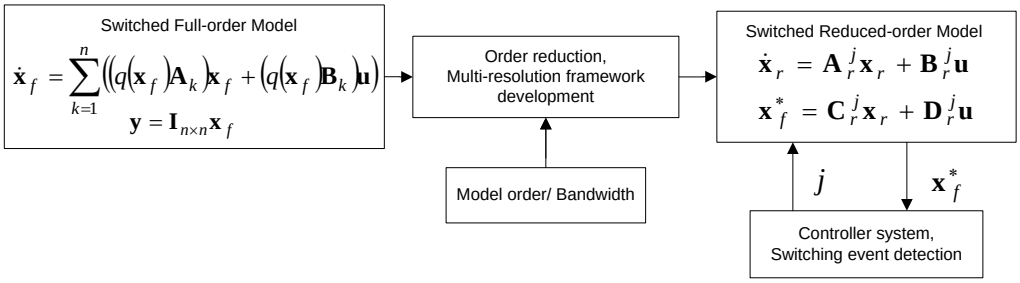

Fig. 5.27. MRS framework for switching converters with state feedback loops.

5.6.2 Model verification

A synchronous buck converter shown in Fig. 5.28, with parameters summarized in Appendix B.5 and system matrices given in Appendix C.4, is considered. The full-order models in each topological instance are 8^{th}-order, and are later reduced to 2^{nd} and 1^{st}-order models. Condition numbers and fastest eigenvalues are shown in Table 5.8 for different loading conditions and

topological instances. As expected, reduced-order models are better conditioned and exhibit more manageable dynamics.

A 5 ms transient startup study is conducted for different model orders and simulation resolutions. The input voltage is 6.5 V and the output voltage is regulated to 1.3 V. The same computational platform and ODE solver settings as in previous studies are used. The actual CPU time and the number of integration steps are shown in Table 5.9, where orders of magnitude improvement in simulation speed and number of integration steps is reported for the reduced-order models.

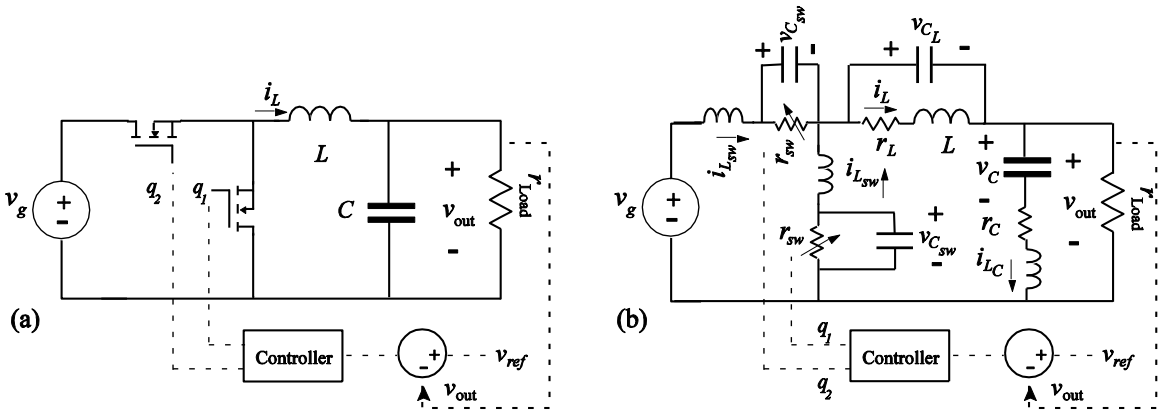

Fig. 5.28. High-fidelity model of a synchronous buck converter with a feedback loop: (a) Circuit schematic; (b) Detailed high-order model.

TABLE 5.8
Condition numbers and fastest eigenvalues for different loading

	Fastest Eigen-value R_{Load}=0.65 Ω	Condition Number R_{Load}=0.65 Ω	Fastest Eigen-value R_{Load}=0.13 Ω	Condition Number R_{Load}=0.13 Ω
Full-order Buck Model MOSFET-1 : On	-6.5×10^{8}	7.52×10^{5}	-1.56×10^{8}	3.18×10^{5}
Full-order Buck Model MOSFET-1 : Off	-6.5×10^{8}	8.73×10^{5}	-1.54×10^{8}	3.2×10^{5}
2nd -order Buck Model MOSFET-1 : On	-7.12×10^{4}	41	-6.4×10^{4}	16
2nd-order Buck Model MOSFET-1 : Off	-3.44×10^{5}	139	-1.4×10^{5}	20
1st -order Buck Model MOSFET-1 : On	-2.12×10^{5}	1	-1.1×10^{5}	1
1st-order Buck Model MOSFET-1 : Off	-2.12×10^{5}	1	-1.1×10^{5}	1

TABLE 5.9
Transient simulation CPU times and integration steps for different model orders

	Simulation Run Time	Number of Integration steps
Full(8^{th})-order Model	320 s	331000
MRS	305 s	151000
2^{nd}-order Model	15 s	11100
1^{st}-order Model	14 s	11300

A 400% step change in load, from 0.65 Ω to 0.15 Ω, is considered to study the transient behavior of the closed-loop system. The output voltage waveforms in Fig. 5.29, for different simulation resolutions, verify that the output voltage is accurately regulated despite the 400% increase in the load current. A zoomed-in view of the first MOSFET voltage and current waveforms, around the load step change, are also shown in Figs. 5.30 and 5.31, respectively. The switching spikes and fast transients are apparent in the full-order model, while the 2^{nd}-order model portrays only the dominant dynamical modes. Although the 1^{st}-order model accurately represents converter dynamics in an "average" sense, one can see that the 2^{nd}-order model provides a better simulation resolution to study dominant dynamical modes. It should be noted that even the 1^{st}-order model includes switching ripples, as the converter model is represented as a hybrid (switched) linear system (it is not averaged!). The MRS of time-invariant models is discussed in the next Section. In an MRS environemnt, the simulation resolution is increased from a low (2^{nd}-order model) to a high resolution mode (8^{th}-order model) at t_s = 0.2 ms. As seen in Figs. 5.29-5.31, the MRS environment successfully employs both low and high resolution modes.

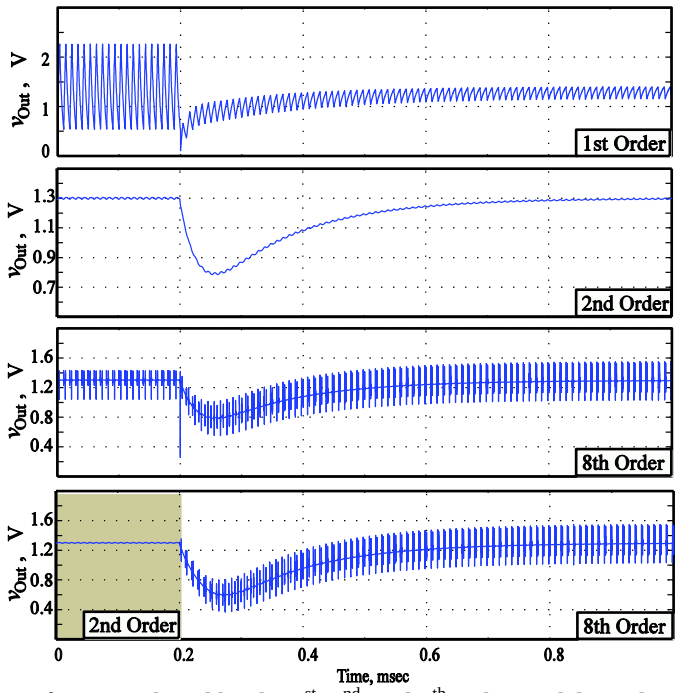

Fig. 5.29 Output voltage waveforms predicted by the 1st, 2nd, and 8th-order models, and resulting from MRS.

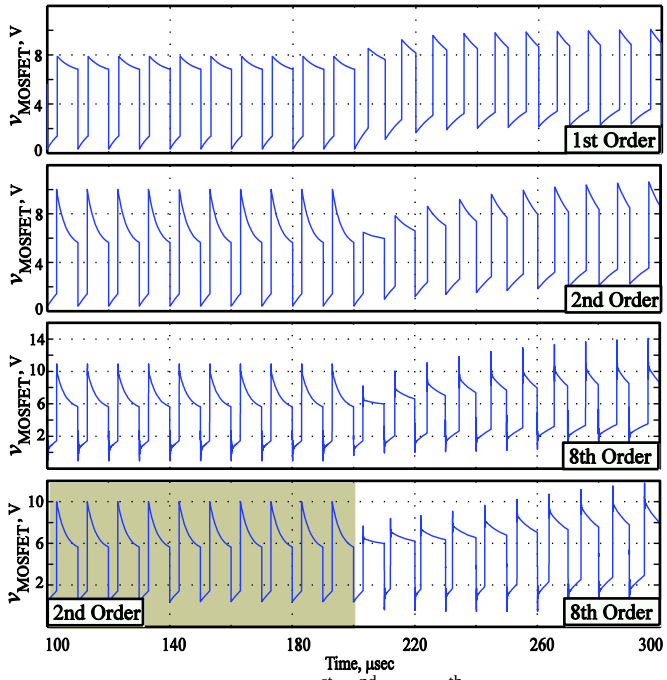

Fig. 5.30 MOSFET voltage waveforms predicted by the 1st, 2nd, and 8th-order models, and resulting from MRS.

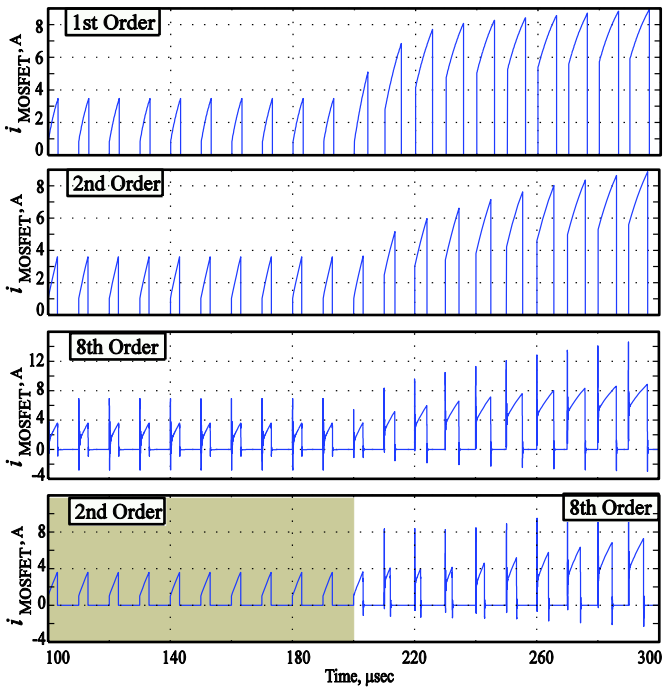

Fig. 5.31 MOSFET current waveforms predicted by the 1st, 2nd, and 8th-order models, and resulted from MRS.

5.7 MRS for Time-invariant Modeling of Switching Converters

5.7.1 Model formulation

So far, switching converters have been modeled as hybrid systems using (5.1)–(5.11), and order reduction has been applied to the LTI systems within each topological instance, $\mathbf{S}_i$. Alternatively, switching-function equations can be incorporated in system formulation leading to a multiple-frequency time-invariant model that does not explicitly involve structural variation. There exist different variations of conceptually similar approaches, namely generalized state-space/multi-frequency averaging [197-199,250], Krylov–Bogoliubov–Mitropolsky [222], dynamic phasors [251-253], and multi-frequency modeling [24]. The multi-frequency averaging (MFA) of an open-loop system is adopted from [200]. Time-invariant models of open-loop systems are periodic (closed-loop systems are aperiodic and a subject of further discussion). MFA is based on the Fourier series expansion of a signal, $x(\tau)$:

$$x(\tau)=\sum_{k=-\infty}^{\infty}\langle x\rangle_k(t)e^{jk\omega_s\tau}=\langle x\rangle_0+2\sum_{k=1}^{\infty}\left(\Re\{\langle x\rangle_k\}\cos(k\omega_s\tau)-\Im\{\langle x\rangle_k\}\sin(k\omega_s\tau)\right),\ \tau\in[t-T,t],\ \omega_s=2\pi/T \tag{5.38}$$

$\langle x\rangle_k(t)$ are the complex Fourier coefficients,[1] referred to as *index-k* average or the *k-phasor*, and are given by

$$\langle x\rangle_k(t)=\frac{1}{T}\int_{t-T}^{T}x(\tau)e^{-jkw_s\tau}d\tau=\Re\{\langle x\rangle_k\}+j\Im\{\langle x\rangle_k\} \tag{5.39}$$

using (5.39), the time derivative of $\langle x\rangle_k(t)$ can be calculated as

$$\frac{d\langle x\rangle_k(t)}{dt}=\left\langle\frac{dx}{dt}\right\rangle_k(t)-jk\omega_s\langle x\rangle_k(t) \tag{5.40}$$

Moreover, the *index-k* average of the product of signals $x(t)$ and $q(t)$ is computed by a discrete evolution

$$\langle qx\rangle_k=\sum_{j=-\infty}^{\infty}\langle q\rangle_{k-j}\langle x\rangle_j \tag{5.41}$$

Equation (5.41) will be used to include the effects of switching function, *q*, in the time-invariant model formulation. Consider the original switched state-space model of a converter

$$\begin{cases}\dot{\mathbf{x}}=\sum_{s=1}^{p}q_s\mathbf{A}_s\mathbf{x}+\sum_{s=1}^{p}q_s\mathbf{B}_s\mathbf{u} & ,\mathbf{x}=[x_1,\cdots x_n]'\\ \mathbf{y}=\sum_{s=1}^{p}q_s\mathbf{C}_s\mathbf{x}+\sum_{s=1}^{p}q_s\mathbf{D}_s\mathbf{u}\end{cases} \tag{5.42}$$

where q_s and $\{\mathbf{A}_s,\mathbf{B}_s,\mathbf{C}_s,\mathbf{D}_s\}$ are the switching signals and state matrices in topological instance, **s**, and **x**, **u**, and **y** are the state, input, and output vectors. The switching function, q_s,

[1] Technically, they are time-varying (except in steady state) which violates the definition of Fourier series coefficients.

and state vector **x** signals are expanded using (5.38). Then, using (5.38)–(5.42), the switched state-space model of (5.42) is replaced with a frequency-dependent time-invariant model

$$\begin{cases} \dot{\widehat{\mathbf{x}}} = \mathbf{A}(\omega_s)\widehat{\mathbf{x}} + \mathbf{B}(\omega_s)\mathbf{u} \\ \mathbf{y} = \mathbf{C}(\omega_s)\widehat{\mathbf{x}} + \mathbf{D}(\omega_s)\mathbf{u} \end{cases} \tag{5.43}$$

The new state vector is

$$\widehat{\mathbf{x}} = \left[\langle x_1\rangle_0, \cdots, \langle x_n\rangle_0, \Re\{\langle x_1\rangle_1\}, \cdots, \Re\{\langle x_n\rangle_m\}, \Im\{\langle x_1\rangle_1\}, \cdots, \Im\{\langle x_n\rangle_m\}\right]' \tag{5.44}$$

where *n* is the order of the physical state vector in (5.42), and *m* is the number of harmonics considered in signal expansion of (5.38). The Fourier series coefficients of the switching function, *q*, are absorbed in the frequency-dependent system matrices $\{\mathbf{A}(\omega_s), \mathbf{B}(\omega_s), \mathbf{C}(\omega_s), \mathbf{D}(\omega_s)\}$. The resulting model order is $2\times m + n$. The time-domain trajectory of the physical state vector $\mathbf{x}(t)$ is calculated using the Fourier expansion of (5.38) and coefficients $\widehat{\mathbf{x}}(t)$ of (5.44)

$$x_i(t) = \langle x_i\rangle_0(t) + 2\sum_{k=1}^{m}\left(\Re\{\langle x_i\rangle_k(t)\}\cos(k\omega_s t) - \Im\{\langle x_i\rangle_k(t)\}\sin(k\omega_s t)\right) \quad , i = 1\cdots n \tag{5.45}$$

As the MFA in (5.43) is an LTI system, linear order-reduction techniques in Chapter 2 and the MRS framework in Section 5.3 are directly applicable. This is explained using the following example.

5.7.2 Model verification

An ideal boost converter shown in Fig. 5.32, with parameters adopted from [200] and summarized in Appendix B.6, is considered. The switched state-space model representation, (5.42), is

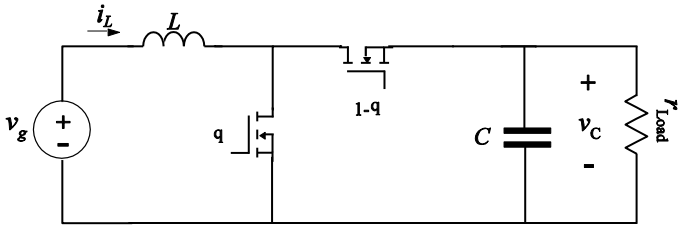

Fig. 5.32 Ideal boost converter with state variables and switching functions (q).

$$\begin{cases} \dfrac{di_L(t)}{dt} = \dfrac{1}{L}\left(v_g - [1-q(t)]v_C(t)\right) \\ \dfrac{dv_C(t)}{dt} = \dfrac{1}{C}\left([1-q(t)]i_L(t) - \dfrac{v_C(t)}{r_{Load}}\right) \end{cases} \tag{5.46}$$

Applying (5.38)–(5.41), the MFA model of (5.46) is

$$\begin{cases} \dot{\hat{\mathbf{x}}} = \mathbf{A}(\omega_s)\hat{\mathbf{x}} + \mathbf{B}(\omega_s)\mathbf{u} \\ \mathbf{y} = \mathbf{I}_6\hat{\mathbf{x}} \end{cases} \tag{5.47}$$

The output vector **y** includes the full-order state vector, $\hat{\mathbf{x}}$, to facilitate the MRS framework in Section 5.3. System state matrices, $\mathbf{A}(\omega_s), \mathbf{B}(\omega_s)$, are given in Appendix C.5. The dc term and first harmonics of switching function, *q*, and physical state variables, i_L, v_C, are considered in the Fourier expansion of (5.38). Thus, the 6th-order state vector, $\hat{\mathbf{x}}$, is

$$\hat{\mathbf{x}} = \left[\langle i_L\rangle_0, \langle v_C\rangle_0, \Re\{\langle i_L\rangle_1\}, \Im\{\langle i_L\rangle_1\}, \Re\{\langle v_C\rangle_1\}, \Im\{\langle v_C\rangle_1\}\right]^T \tag{5.48}$$

Higher order models are achievable by incorporating more harmonics or higher order component models (see Fig. 5.1). Here, we only consider the first harmonics (which leads to a 6th-order model) for simplicity of model formulation and proof of concept.

Time-domain trajectories of the original state variables (inductor current and capacitor voltage) resulting from the switched state-space model in (5.46) and the MFA model in (5.47) show an acceptable match in Figs. 5.33–5.34(a). Accurate dc terms (index-zero average) of the respective variables, that incorporate the large-ripple effects, are shown in Figs. 5.33–5.34(a). Using order-reduction techniques, a 2nd-order model is extracted from (5.48):

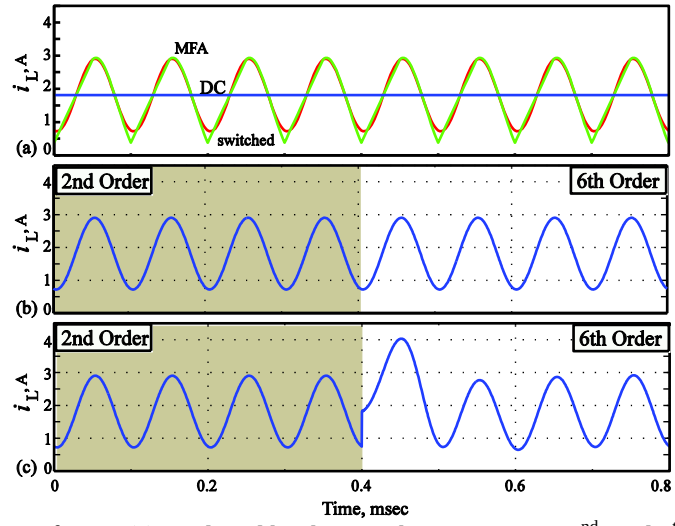

Fig. 5.33 Inductor current waveforms: (a) Predicted by the switching converter, 2nd- and 6th-order MFA models; (b) Resulting from MRS with appropriate initialization; (c) Resulting from MRS with incorrect initialization.

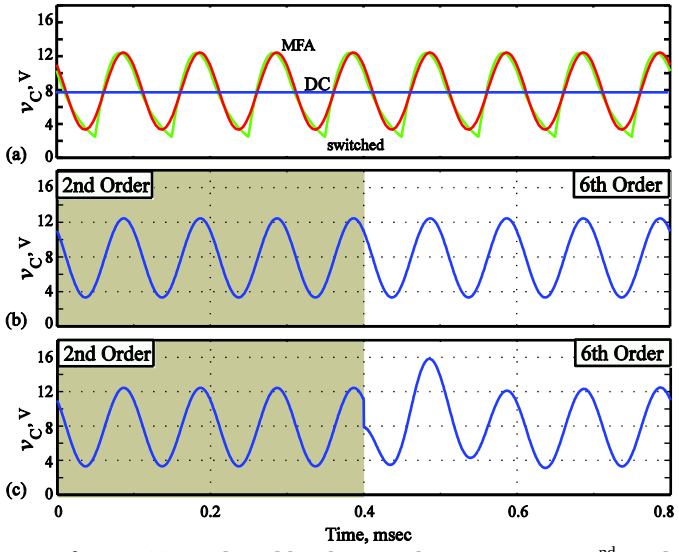

Fig. 5.34 Capacitor voltage waveforms: (a) Predicted by the switching converter, 2nd- and 6th-order MFA models; (b) Resulting from MRS with appropriate initialization; (c) Resulting from MRS with incorrect initialization.

$$\begin{cases} \dot{\hat{\mathbf{x}}}_r = \mathbf{A}_r \hat{\mathbf{x}}_r + \mathbf{B}_r \mathbf{u} \quad , \hat{\mathbf{x}}_r \in \Re^2 \\ \mathbf{y} = \mathbf{C}_r \hat{\mathbf{x}}_r + \mathbf{D}_r \mathbf{u} \end{cases} \tag{5.49}$$

Eigenvalues of both reduced-(2nd)- and full-(6th)-order models are shown in Table 5.10. It should be noted that the resulting 2nd-order model is not the same as the conventional state-space averaged model. In particular, since the output vector of (5.47) carries the full state vector, $\hat{\mathbf{x}}$, and the reduction process preserves the input-output relationship, one can retrieve the full-order state vector from the 2nd-order model. This is not feasible in conventional state-space averaging.

TABLE 5.10
Eigenvalues of the reduced- and full-order models

Reduced 2nd-order model	$-1.62\times10^4 \pm j\ 2.3\times10^4$		
Full 6th-order model	$-1.42\times10^4 \pm j\ 8.62\times10^4$	$-1.42\times10^4 \pm j\ 2.22\times10^4$	$-1.42\times10^4 \pm j\ 4.46\times10^4$

The MRS environment of the MFA model in (5.47) is constructed according to the methodology given in Section 5.3. The output of the 2nd-order model in (5.49) projects an approximation of the full-order state in (5.48), $\hat{\mathbf{x}}$, which is used to construct the trajectories of physical variables of (5.46):

$$\begin{cases} i_L(t) = y_1(t) + 2\left(y_3(t)\cos(\omega_s t) - y_4(t)\sin(\omega_s t)\right) \\ v_C(t) = y_2(t) + 2\left(y_5(t)\cos(\omega_s t) - y_6(t)\sin(\omega_s t)\right) \end{cases} \tag{5.50}$$

The inductor current and capacitor voltage waveforms constructed from the 2nd-order model (shown darker in Figs. 5.33–34(b) and Figs. 5.33–34(c)) closely resemble those of the original switching model of (5.46) and the 6th-order model of (5.47) in Fig. 5.33-34(a).

The simulation resolution has changed from low to high at t_s = 400 μs. The output vector of the reduced-order model in (5.49) is used to initialize (5.47). This makes the simulation transition appear seamless in Figs. 5.33–34(b). If one initiates the state vector in (5.48) with actual dc terms while initial values of the harmonics terms are *intentionally* left at zero, then change in simulation resolution at t_s = 400 μs will lead to a transition spike (Fig. 5.33-34(c)).

5.8 Summary

MRS provides an alternative method to analyze power converters by providing an appropriate amount of detail based on the time scale and phenomenon being considered. A framework for MRS of switched linear systems is developed. First, a detailed full-order model of the converter is built that accounts for the system parasitics, switching nonlinearity, and switching event detection. This model includes higher order effects such as stray capacitance of the inductor, equivalent series resistance and inductance of the capacitor, diode reverse-recovery phenomenon, wiring parasitics, and MOSFET dynamics. Efficient order-reduction techniques are then used to extract several lower order models for the desired resolution of the simulation. This results in different state matrices and state vectors for a given topological instance of the converter circuit, whereas the state variable continuity is insured across the switching events taking into account different levels of modeling resolutions. This methodology is demonstrated on switched linear systems, cascaded converters, converters with nonlinear elements, and closed-loop systems. MRS environments for time-invariant representation of switching converters are also discussed. Significant improvement (orders of magnitude) in simulation speed and reduction in the number of integration steps is reported.

CHAPTER 6

CONCLUSION AND FUTURE WORK

6.1 Contributions

An effort is undertaken to break the compromise between modeling fidelity and simulation speed and realize an ideal computational prototyping environment for power electronics analysis and design. It is shown that a static MEC model can be extended, using modular conductive flux tubes, to incorporate eddy current dynamics while avoiding crude geometrical assumptions. The resulting HFMEC model is extended to saturated inductors, transformers, and linear plungers. In all cases, automated order-reduction tools are successfully applied to extract the essential system dynamics and thus ease the computational burden while preserving model accuracy. In particular, nonlinear reduced-order systems are constructed by applying reduction techniques on locally linearized systems and composing a parametric reduced-order model. Order reduction techniques are used in a hybrid fashion and are extended to time-varying and MIMO systems. Proposed models are verified for different magnetic materials (powdered iron and laminated steel) and various excitations (small and large signals), where the model orders have been reduced from several hundreds to a few state variables.

As another subset of physics-based models, reduced-order modeling of FEA models with relative motion is studied. It is shown that an appropriate movement-path discretization conserves the state vector dimension and thus the consistency of the order-reduction process. The original 3577^{th}-order model has been reduced to a 3^{rd}-order model and dynamically incorporated the relative motion.

At the circuit level, wide-bandwidth component models are introduced to form high-fidelity models of switching converters. Both time-invariant and hybrid model formulations of switching converters are examined. Several model-order/simulation-resolutions are extracted from the high-fidelity converter model, and appropriately assembled in an MRS environment. In particular, proper initialization of hybrid models based on the underlying reduction technique are discussed. Moreover, state continuity across different switching events and simulation resolution is preserved. This simulation framework is extended to resonant converters, converters with nonlinear elements, and controlled systems. In all cases, several orders of magnitude improvement in simulation speed and reduction in the number of integration steps is reported, enhancing simulation accuracy, stability, and speed.

6.2 Future Work

HFMEC models can be improved by including magnetic hysteresis effects [16]. Early work in reduced-order modeling of FEA-based models has shown promise [254]. Similar approaches may be used to include the memory effects of magnetic hysteresis in the reduced-order model in Section 3.4. Moreover, force and torque formulations are required in order to employ reduced-order FEA/HFMEC models as design tools for electrical machinery. Direct Maxwell stress tensor [135] and virtual work methods [131] are candidate approaches for force formulation.

The MRS framework can be extended to more complex power electronics-based systems, e.g., machine-inverter combinations. High-fidelity models of electrical machines that account for distributed effects of rotor circuitry or drive harmonics are readily available in the literature (induction machines [255], synchronous machines [256-258] and permanent magnet machines

[206, 259]). In these models, the main challenge is to tackle nonlinearities due to the presence of speed terms (i.e., back EMF) in Park equations.

APPENDIX A

MAGNETIC CORE DIMENSIONS

Tables A.1 to A.4 show the material properties of considered magnetic cores.

TABLE A.1
Toroidal core characteristics

DIMENSIONS\CORE TYPE	T400-26 [260]	M19-26	T200-26 [261]
Inner radius, r_{in}	28.6 mm	46.75 mm	15.82 mm
Outer radius, r_{out}	51 mm	61.5 mm	25.72 mm
Height, h	33 mm	0.475 mm	14.19 mm
Conductivity, σ	20 $s.m^{-1}$ [163]	2×10^{6} $s.m^{-1}$ [262]	20 $s.m^{-1}$
Number of laminations, n_L	1	50	1
Number of turns, N	9	76	60
External resistance, R_{ext}	23 mΩ	85.76 mΩ	70 mΩ

TABLE A.2
U93/76/30 data

Parameter	Value
w_1	28 mm
w_2	48 mm
w_3	76 mm
w_4	36 mm
w_5	93 mm
w_6	30 mm
N	15 turns
R_{ext}	100 m Ω
δ	200 $s.m^{-1}$
μ_r	2200
$r_{in} = 4w_2 + 2w_4$	264 mm
$r_{out} = 4w_3 + 2w_5$	490 mm

TABLE A.3
Transformer specifications

Parameter	Value
h	14.19 mm
N_1,N_2	60 turns
r_{ext1}, r_{ext2}	70 mΩ
σ	20 $s.m^{-1}$
r_{in}	15.82 mm
r_{out}	25.72 mm

TABLE A.4
FEM-plunger data

Parameter	Value
w_1	13 cm
w_2	5 cm
w_3	6 cm
w_4	1 cm
w_5	4 cm
w_6	2.5 cm
w_7	3 cm
w_8	4 cm
w_9	6.8 cm
w_{10}	10 cm
σ_{copper}	5×10^{7}
δ	200
μ_r	4000
r_{ext}	20 mΩ

APPENDIX B

CIRCUIT PARAMETERS

Tables B.1 to B.6 show circuit parameters of switching converters.

TABLE B.1
Boost converter

Parameter	Value
v_g	5 volt
L	1.316 mH
r_L	0.14 Ω
C_L	1 pF
L_{sw}	20 nH
C_{sw}	200 pF
r_{sw} (on)	0.2 Ω
r_{sw} (off)	2.3 M Ω
L_d	5 nH
r_{L_d}	1 m Ω
V_d (on)	0.61 volt
V_d (off)	0 volt
r_d (on)	50 m Ω
r_d (off)	40 M Ω
C_d (on)	15 pF
C_d (off)	100 pF
r_{C_d}	5 m Ω
C	42 μF
L_C	100 pH
r_C	0.38 Ω
R_{load}	10.5 Ω
f_{sw}	10 KHz
Duty	0.5

TABLE B.2
Class-E Amplifier

Parameter	Value
v_g	20 volt
L_1	21.9 μH
L_2	4.97 μH
r_{L_1}	10 m Ω
r_{L_2}	2 m Ω
C_{L_1}	5 pF
C_{L_2}	5 pF
L_{sw}	10 nH
C_{sw}	80 pF
r_{sw} (on)	0.6 Ω
r_{sw} (off)	2 M Ω
C_1	442 pF
C_2	357 pF
L_{C_1}	5 pH
L_{C_2}	5 pH
r_{C_1}	0.1 Ω
r_{C_2}	0.1 Ω
R_{load}	12.5 Ω
f_{sw}	4 MHz
Duty	0.5

TABLE B.3
Cascaded converter

Parameter	Value
v_g	10 volt
L_1	2.16 mH
L_2	4.54 mH
r_{L_1}, r_{L_2}	20 m Ω
C_{L_1}, C_{L_2}	5 nF
L_{sw_1}, L_{sw_2}	20 nH
C_{sw_1}, C_{sw_2}	10 nF
r_{sw_1}, r_{sw_2} (on)	20 m Ω
r_{sw_1}, r_{sw_2} (off)	20 M Ω
r_{d_1}, r_{d_2} (on)	220 m Ω
r_{d_1}, r_{d_2} (off)	10 MΩ
V_{d_1}, V_{d_2} (on)	0.58 Volt
C_{d_1}, C_{d_2} (on)	1.5 nF
C_{d_1}, C_{d_2} (off)	10 nF
r_{L_d}	1 m Ω
L_d	50 nH
C_1, C_2	96 μF
L_{C_1}, L_{C_2}	1 nF
r_{C_1}, r_{C_2}	345 m Ω
R_{load}	64.5 Ω
f_{sw_1}	50 KHz
f_{sw_2}	30 KHz
$duty_1$, $duty_2$	0.49

TABLE B.4
Nonlinear boost converter

Parameter	Value
v_g	5 V
L_{eff_1}	200 μH
L_{eff_2}	100 μH
L_{eff_3}	20 μH
I_{tr_1}	0.85 A
I_{tr_1}	1.05 A
r_L	0.1 Ω
C_L	1 pF
L_{sw}	20 nH
C_{sw}	200 pF
r_{sw} (on)	0.2 Ω
r_{sw} (off)	2 M Ω
L_d	5 nH
r_{L_d}	10 m Ω
r_d (on)	50 m Ω
r_d (off)	40 M Ω
V_d (on)	0.61 V
V_d (off)	0 V
C_d (on)	15 pF
C_d (off)	100 pF
r_{C_d}	5 m Ω
C	42 μF
L_C	100 pH
r_C	0.4 Ω
R_{load}	20 Ω
f_{sw}	50 kHz
Duty	0.5

TABLE B.5
Closed-loop synchronous buck converter

Parameter	Value
v_g	6.5 V
V_{ref}	1.3 V
L	5 μH
r_L	10 m Ω
C_L	10 nF
L_{sw}	10 nH
C_{sw}	20 nF
r_{sw} (on)	0.4 Ω
r_{sw} (off)	20 M Ω
r_C	1 m Ω
C	288 μF
L_C	1 nF
f_{sw}	100 kHz
R_{Load1}	0.65 Ω
R_{Load2}	0.13 Ω

TABLE B.6
Ideal boost converter

Parameter	Value
v_g	5 V
duty	0.5
L	100 μH
R	8 Ω
C	4.4 μF
f_{sw}	10 kHz

Controller: $\frac{1}{1\times10^{-5}s+1}\cdot\left(5\times10^{3}\frac{1}{s}+0.3\right)$. The first transfer function is to avoid an algebraic loop due to the presence of the proportional gain.

APPENDIX C

SYSTEM EQUATIONS

C.1 Boost Converter

$$\mathbf{A}=\begin{bmatrix}
-\frac{r_L}{L} & 0 & \frac{1}{L} & 0 & 0 & 0 & 0 & 0 \\
0 & 0 & 0 & 0 & 0 & 0 & 0 & \frac{1}{C} \\
-\frac{1}{C_L} & 0 & 0 & \frac{1}{C_L} & 0 & \frac{1}{C_L} & 0 & 0 \\
0 & 0 & -\frac{1}{L_{sw}} & 0 & -\frac{1}{L_{sw}} & 0 & 0 & 0 \\
0 & 0 & 0 & \frac{1}{C_{sw}} & -\frac{1}{r_{sw}C_{sw}} & 0 & 0 & 0 \\
0 & 0 & -\frac{1}{L_d} & 0 & 0 & -\frac{\left(r_{Load}+r_{L_d}\right)}{L_d} - \frac{\left(r_d+r_{C_d}\right)}{\left(r_{C_d}+r_d\right)L_d} & -\frac{1}{L_d}+\frac{r_{C_d}}{\left(r_{C_d}+r_d\right)L_d} & \frac{r_{Load}}{L_d} \\
0 & 0 & 0 & 0 & 0 & \frac{r_d}{\left(r_{C_d}+r_d\right)C_d} & -\frac{1}{\left(r_{C_d}+r_d\right)C_d} & 0 \\
0 & -\frac{1}{L_C} & 0 & 0 & 0 & \frac{r_{Load}}{L_C} & 0 & \frac{\left(r_{Load}+r_C\right)}{L_C}
\end{bmatrix}$$

$$\mathbf{B}=\begin{bmatrix}
0 & 0 \\
0 & 0 \\
0 & 0 \\
\frac{1}{L_{sw}} & 0 \\
0 & 0 \\
\frac{1}{L_d} & -\frac{r_{C_d}}{\left(r_{C_d}+r_d\right)L_d} \\
0 & \frac{1}{\left(r_{C_d}+r_d\right)C_d} \\
0 & 0
\end{bmatrix} \quad \mathbf{C}=\mathbf{I}_8 \quad \mathbf{D}=[0]_{8\times 2}$$

C.2 Class-E Amplifier

$$\mathbf{A}=\begin{bmatrix}
\frac{-r_{L_1}}{L_1} & 0 & 0 & 0 & 0 & 0 & 0 & 0 & \frac{1}{L_1} & 0 \\
0 & 0 & 0 & 0 & 0 & 0 & \frac{1}{C_1} & 0 & 0 & 0 \\
0 & 0 & \frac{-r_{L_2}}{L_2} & 0 & 0 & 0 & 0 & 0 & 0 & \frac{1}{L_2} \\
0 & 0 & 0 & 0 & 0 & 0 & 0 & \frac{1}{C_2} & 0 & 0 \\
0 & 0 & 0 & 0 & 0 & -\frac{1}{L_{sw}} & 0 & 0 & -\frac{1}{L_{sw}} & 0 \\
0 & 0 & 0 & 0 & \frac{1}{C_{sw}} & -\frac{1}{r_{sw}C_{sw}} & 0 & 0 & 0 & 0 \\
0 & -\frac{1}{L_{C_1}} & 0 & 0 & 0 & 0 & -\frac{r_{C_1}}{L_{C_1}} & 0 & -\frac{1}{L_{C_1}} & 0 \\
0 & 0 & 0 & -\frac{1}{L_{C_2}} & 0 & 0 & 0 & -\frac{\left(R_{Load}+r_{C_2}\right)}{L_{C_2}} & -\frac{1}{L_{C_2}} & -\frac{1}{L_{C_2}} \\
-\frac{1}{C_{L_1}} & 0 & 0 & 0 & \frac{1}{C_{L_1}} & 0 & \frac{1}{C_{L_1}} & \frac{1}{C_{L_1}} & 0 & 0 \\
0 & 0 & -\frac{1}{C_{L_2}} & 0 & 0 & 0 & 0 & \frac{1}{C_{L_2}} & 0 & 0
\end{bmatrix}\quad \mathbf{B}=\begin{bmatrix}
0 \\ 0 \\ 0 \\ 0 \\ \frac{1}{L_{sw}} \\ 0 \\ \frac{1}{L_{C_1}} \\ \frac{1}{L_{C_2}} \\ 0 \\ 0
\end{bmatrix}\quad \mathbf{C}=\mathbf{I}_{10}\ \mathbf{D}=[0]_{10\times 1}$$

C.3 Cascaded Converter

$$\mathbf{A}_{Boost}=\begin{bmatrix}
-\frac{r_{L_1}}{L_1} & 0 & 0 & 0 & 0 & 0 & \frac{1}{L_1} \\
0 & 0 & 0 & 0 & 0 & \frac{1}{C_1} & 0 \\
0 & 0 & 0 & -\frac{1}{L_{sw}} & 0 & 0 & -\frac{1}{L_{sw}} \\
0 & 0 & \frac{1}{C_{sw}} & -\frac{1}{r_{sw}C_{sw}} & 0 & 0 & 0 \\
0 & 0 & 0 & 0 & \frac{1}{r_dC_d} & \frac{1}{C_d} & 0 \\
0 & -\frac{1}{L_C} & 0 & 0 & -\frac{1}{L_C} & -\frac{r_C}{L_C} & -\frac{1}{L_C} \\
-\frac{1}{C_L} & 0 & \frac{1}{C_L} & 0 & 0 & \frac{1}{C_L} & 0
\end{bmatrix}\quad \mathbf{B}_{Boost}=\begin{bmatrix}
0 & 0 & 0 \\ 0 & 0 & 0 \\ \frac{1}{L_{sw}} & 0 & 0 \\ 0 & 0 & 0 \\ 0 & \frac{1}{C_d} & 0 \\ \frac{1}{L_C} & 0 & 0 \\ 0 & \frac{1}{C_L} & 0
\end{bmatrix}\quad \mathbf{C}_{Boost}=\mathbf{I}_7\ \mathbf{D}_{Boost}=[0]_{7\times 3}$$

$$\mathbf{A}_{Buck-Boost}=\begin{bmatrix} -\frac{r_{L_2}}{L_2} & 0 & 0 & 0 & 0 & 0 & \frac{1}{L_2} \\ 0 & -\frac{1}{C_2\left(R_{Load}+r_{C_2}\right)} & 0 & 0 & 1-\frac{r_{C_2}}{\left(R_{Load}+r_{C_2}\right)} & 0 & 0 \\ 0 & 0 & 0 & -\frac{1}{L_{sw}} & 0 & 0 & -\frac{1}{L_{sw}} \\ 0 & 0 & \frac{1}{C_{sw}} & -\frac{1}{r_{sw}C_{sw}} & 0 & 0 & 0 \\ 0 & -\frac{R_{Load}}{L_d\left(R_{Load}+r_{C_2}\right)} & 0 & 0 & -\frac{r_{L_d}}{L_d}-\frac{r_{C_2}R_{Load}}{L_d\left(R_{Load}+r_{C_2}\right)} & -\frac{1}{L_d} & -\frac{1}{L_d} \\ 0 & 0 & 0 & 0 & \frac{1}{C_{d_2}} & -\frac{1}{r_{d_2}C_{d_2}} & 0 \\ -\frac{1}{C_L} & 0 & \frac{1}{C_L} & 0 & \frac{1}{C_L} & 0 & 0 \end{bmatrix}$$

$$\mathbf{B}_{Buck-Boost}=\begin{bmatrix} 0 & 0 \\ 0 & 0 \\ \frac{1}{L_{sw}} & 0 \\ 0 & 0 \\ 0 & 0 \\ 0 & \frac{1}{r_{d_2}C_{d_2}} \\ 0 & 0 \end{bmatrix} \quad \mathbf{C}_{Buck-Boost}=\mathbf{I}_7 \;\; \mathbf{D}_{Buck-Boost}=\left[0\right]_{7\times 2}$$

C.4 Synchronous Buck Converter

$$\mathbf{A}=\begin{bmatrix} -\frac{r_L}{L} & 0 & 0 & 0 & 0 & 0 & 0 & \frac{1}{L} \\ 0 & 0 & 0 & 0 & 0 & 0 & \frac{1}{C} & 0 \\ 0 & 0 & -\frac{R_{Load}}{L_{sw_1}} & -\frac{R_{Load}}{L_{sw_1}} & -\frac{1}{L_{sw_1}} & 0 & -\frac{R_{Load}}{L_{sw_1}} & -\frac{1}{L_{sw_1}} \\ 0 & 0 & -\frac{R_{Load}}{L_{sw_2}} & -\frac{R_{Load}}{L_{sw_2}} & 0 & \frac{1}{L_{sw_2}} & -\frac{R_{Load}}{L_{sw_2}} & -\frac{1}{L_{sw_2}} \\ 0 & 0 & \frac{1}{C_{sw_1}} & 0 & -\frac{1}{r_{sw_1}C_{sw_1}} & 0 & 0 & 0 \\ 0 & 0 & 0 & -\frac{1}{C_{sw_2}} & 0 & -\frac{1}{r_{sw_2}C_{sw_2}} & 0 & 0 \\ 0 & -\frac{1}{L_C} & \frac{R_{Load}}{L_C} & \frac{R_{Load}}{L_C} & 0 & 0 & \frac{\left(R_{Load}+r_C\right)}{L_C} & 0 \\ -\frac{1}{C_L} & 0 & \frac{1}{C_L} & \frac{1}{C_L} & 0 & 0 & 0 & 0 \end{bmatrix} \quad \mathbf{B}=\begin{bmatrix} 0 \\ 0 \\ \frac{1}{L_{sw_{1,2}}} \\ 0 \\ 0 \\ 0 \\ 0 \\ 0 \end{bmatrix}$$

$$\mathbf{C}=\mathbf{I}_8 \quad \mathbf{D}=\left[0\right]_{8\times 1}$$

C.5 MFA Representation of an Ideal Boost Converter

$$\mathbf{A}(\omega_s)=\begin{bmatrix} 0 & \frac{D-1}{L} & 0 & 0 & \frac{\sin(2\pi D)}{L\pi} & \frac{\cos(2\pi D)-1}{L\pi} \\ \frac{1-D}{C} & -\frac{1}{r_{Load}C} & -\frac{\sin(2\pi D)}{C\pi} & \frac{1-\cos(2\pi D)}{C\pi} & 0 & 0 \\ 0 & \frac{\sin(2\pi D)}{2L\pi} & 0 & \omega_s & \frac{D-1}{L} & 0 \\ 0 & \frac{\cos(2\pi D)-1}{2L\pi} & -\omega_s & 0 & 0 & \frac{D-1}{L} \\ -\frac{\sin(2\pi D)}{2\pi C} & 0 & \frac{1-D}{C} & 0 & -\frac{1}{RC} & \omega_s \\ \frac{1-\cos(2\pi D)}{2\pi C} & 0 & 0 & \frac{1-D}{C} & -\omega_s & -\frac{1}{RC} \end{bmatrix} \qquad \mathbf{B}(\omega_s)=\begin{bmatrix} \frac{1}{L} \\ 0 \\ 0 \\ 0 \\ 0 \\ 0 \end{bmatrix}$$

APPENDIX D

MATLAB CODES

D.1 Quasi Pole/Zero Cancellation

```
% Order reduction of the input system, "sys", based on the quasi pole-zero method
full_model=sys;

full_dcgain=dcgain(full_model);          % Full-order model dc gain
full_zero=zero(full_model);              % Full-order model zeros
full_pole=pole(full_model);              % Full-order model poles

full_zero_sorted=sort(abs(full_zero),'descend');   % Full-order model zeros SORTED
full_pole_sorted=sort(abs(full_pole),'descend');   % Full-order model poles SORTED

pp=full_pole_sorted;
zz=full_zero_sorted;
index_buffer=[];

for con=1:min(length(pp),length(zz));

   small=min(pp(con),zz(con));
   big=max(pp(con),zz(con));

   if (((big-small)/big)<0.10)                    %  10% tolerance level; can be adjusted arbitrarily
         index_buffer=[index_buffer con];
   end

end

pole_reduced=-pp;
zero_reduced=-zz;

pole_reduced(index_buffer)=[];
zero_reduced(index_buffer)=[];

sys_reduced=zpk(zero_reduced,pole_reduced,1);
al=dcgain(sys)/dcgain(sys_reduced);
sys_reduced=zpk(zero_reduced,pole_reduced,al);
```

D.2 Arnoldi via Modified Gram-Schmidt

```
function W=Arnoldi(A,B,E,q)

% W is the projection vector used in projection and reduction
% E could be the identity matrix in most cases
% q is the reduced model order

[m,n]=size(A);
V=zeros(m,q);
temp=A\B;
V(:,1)=temp/norm(temp);
for i=1 : q-1
   V(:,i+1)=A\E*V(:,i);
   for j=1 : i
      V(:,i+1)=V(:,i+1)-(V(:,i+1)'*V(:,j))*V(:,j);          %Orthogonalize
      V(:,i+1)=V(:,i+1)/norm(V(:,i+1));                     %Normalize
   end
end
```

D.3 FEM of an Inductor

```
%  FEM of a linear toroidal core adopted from modified PLC code.
%  Core structure is first constructed  in MATLAB PDE toolbox.
% "P", "e", and "t" parameters from have to be retrieved from MATLAB's PDE Toolbox

Nel= max(size(t));              % Number of elements
Nnodes= max(size(p));           % Number of nodes

% Regions definition
copperreg= [ 4:21 ];
ferritereg= [1];
airreg= [2 3];
metreg= union(copperreg,ferritereg);
poscopreg= copperreg(1:2:length(copperreg));
negcopreg= copperreg(2:2:length(copperreg));

% define set of nodes in metal, possibly shared
metind= find(ismember(t(4,:),metreg));
mnodes= unique(union(union(t(1,metind),t(2,metind)),t(3,metind)));

% define set of nodes in air, possibly shared
airind= find(ismember(t(4,:),airreg));
anodes= unique(union(union(t(1,airind),t(2,airind)),t(3,airind)));
```

```
% define set of nodes on outer boundary (with air, automatically)
regbl= find(e(6,:) == 0);
regbr= find(e(7,:) == 0);
regbaonly= union(regbl,regbr);
banodes= unique([e(1,regbaonly) e(2,regbaonly)]);

% define set of nodes on metal-air boundary
manodes= intersect(mnodes,anodes);

% define set of nodes in metal only
mmnodes= setdiff(mnodes,manodes);

% define set of nodes in air only- not with metal or boundary
aanodes= setdiff(setdiff(anodes,manodes),banodes);

map= [mmnodes manodes aanodes banodes];
[y,index]= sort(map);
list= [1:Nnodes];
imap= list(index);
pnew= p(:,map);
tnew(1,:)= imap(t(1,:));
tnew(2,:)= imap(t(2,:));
tnew(3,:)= imap(t(3,:));
tnew(4,:)= t(4,:);
p=pnew; t=tnew;
p=p'; t=t';


% Material Charactersitcs
munot= 4*pi*1e-7;
perm(copperreg)= munot;
perm(ferritereg)= 80.43*munot;                    % Actual expected value of mu
perm(airreg)= munot;

sigma(copperreg)= 5.8e7;
sigma(ferritereg)= 20;
sigma(airreg)= 0;

% Current direction
Jbar(poscopreg)= 1;
Jbar(negcopreg)= -1;
Jbar(ferritereg)= 0;
Jbar(airreg)= 0;

% Find triangle areas
[AR,A1,A2,A3]=PDETRG(p',t');

% Formulation of FEA matrices  (S,C,T) and vectors ,b

bcols= zeros(Nnodes,length(poscopreg)+length(negcopreg));
```

```
Cglob= zeros(Nnodes,Nnodes);

for x=1:length(poscopreg)
   bfind= find(t(:,4)==poscopreg(x));
   areabp(x)= sum(AR(bfind));

   for y= 1:length(bfind)
      z= bfind(y);
      bcols(t(z,1),x)= bcols(t(z,1),x) + AR(z);
      bcols(t(z,2),x)= bcols(t(z,2),x) + AR(z);
      bcols(t(z,3),x)= bcols(t(z,3),x) + AR(z);
   end

   bcols(:,x)= bcols(:,x)*sigma(poscopreg(x))/3;
   Ct= [1;1;1]*bcols(:,x)';

   for y=1:length(bfind)
      z= bfind(y);
      Cglob(t(z,1),:)= Cglob(t(z,1),:) + AR(z)*Ct(1,:)/areabp(x)/3;
      Cglob(t(z,2),:)= Cglob(t(z,2),:) + AR(z)*Ct(2,:)/areabp(x)/3;
      Cglob(t(z,3),:)= Cglob(t(z,3),:) + AR(z)*Ct(3,:)/areabp(x)/3;
   end

end

for x=1:length(negcopreg)
   bfind= find(t(:,4)==negcopreg(x));
   areabn(x)= sum(AR(bfind));

   for y= 1:length(bfind)
      z= bfind(y);
      bcols(t(z,1),x+length(poscopreg))= bcols(t(z,1),x+length(poscopreg)) + AR(z);
      bcols(t(z,2),x+length(poscopreg))= bcols(t(z,2),x+length(poscopreg)) + AR(z);
      bcols(t(z,3),x+length(poscopreg))= bcols(t(z,3),x+length(poscopreg)) + AR(z);
   end

   bcols(:,x+length(poscopreg))= bcols(:,x+length(poscopreg))*sigma(negcopreg(x))/3;
   Ct= [1;1;1]*bcols(:,x+length(poscopreg))';

   for y=1:length(bfind)
      z= bfind(y);
      Cglob(t(z,1),:)= Cglob(t(z,1),:) + AR(z)*Ct(1,:)/areabn(x)/3;
      Cglob(t(z,2),:)= Cglob(t(z,2),:) + AR(z)*Ct(2,:)/areabn(x)/3;
      Cglob(t(z,3),:)= Cglob(t(z,3),:) + AR(z)*Ct(3,:)/areabn(x)/3;
   end

end

Sglob= zeros(Nnodes,Nnodes);
Tglob= zeros(Nnodes,Nnodes);
q2glob= zeros(Nnodes,1);
```

```
for x=1:Nel
   xi= p(t(x,1),1);
   xj= p(t(x,2),1);
   xk= p(t(x,3),1);
   yi= p(t(x,1),2);
   yj= p(t(x,2),2);
   yk= p(t(x,3),2);

   ai= xj*yk - xk*yj;
   bi= yj - yk;
   ci= xk - xj;

   aj= xk*yi - xi*yk;
   bj= yk - yi;
   cj= xi - xk;

   ak= xi*yj - xj*yi;
   bk= yi - yj;
   ck= xj - xi;

   locperm= perm(t(x,4));
   locsig= sigma(t(x,4));
   locJbar= Jbar(t(x,4));

   Se= (1/(locperm*4*AR(x)))*[ (bi^2 + ci^2) (bi*bj +ci*cj) (bi*bk + ci*ck);
      (bi*bj + ci*cj) (bj^2 + cj^2) (bj*bk + cj*ck);
      (bi*bk + ci*ck) (bj*bk + cj*ck) (bk^2 + ck^2)];
   Te= (locsig*AR(x)/12)*[ 2 1 1; 1 2 1; 1 1 2];

   k=0;
   if (ismember(t(x,4),negcopreg))
      kfind= find(negcopreg==t(x,4));
      k= -1*AR(x)/areabn(kfind)/3;
   end
   if (ismember(t(x,4),poscopreg))
      kfind= find(poscopreg==t(x,4));
      k= 1*AR(x)/areabp(kfind)/3;
   end
   q2e= k*[1 1 1]';

   Sglob(t(x,1),t(x,1))= Sglob(t(x,1),t(x,1))+Se(1,1);
   Sglob(t(x,1),t(x,2))= Sglob(t(x,1),t(x,2))+Se(1,2);
   Sglob(t(x,1),t(x,3))= Sglob(t(x,1),t(x,3))+Se(1,3);
   Sglob(t(x,2),t(x,1))= Sglob(t(x,2),t(x,1))+Se(2,1);
   Sglob(t(x,2),t(x,2))= Sglob(t(x,2),t(x,2))+Se(2,2);
   Sglob(t(x,2),t(x,3))= Sglob(t(x,2),t(x,3))+Se(2,3);
   Sglob(t(x,3),t(x,1))= Sglob(t(x,3),t(x,1))+Se(3,1);
   Sglob(t(x,3),t(x,2))= Sglob(t(x,3),t(x,2))+Se(3,2);
   Sglob(t(x,3),t(x,3))= Sglob(t(x,3),t(x,3))+Se(3,3);

   Tglob(t(x,1),t(x,1))= Tglob(t(x,1),t(x,1))+Te(1,1);
```

```
    Tglob(t(x,1),t(x,2))= Tglob(t(x,1),t(x,2))+Te(1,2);
    Tglob(t(x,1),t(x,3))= Tglob(t(x,1),t(x,3))+Te(1,3);
    Tglob(t(x,2),t(x,1))= Tglob(t(x,2),t(x,1))+Te(2,1);
    Tglob(t(x,2),t(x,2))= Tglob(t(x,2),t(x,2))+Te(2,2);
    Tglob(t(x,2),t(x,3))= Tglob(t(x,2),t(x,3))+Te(2,3);
    Tglob(t(x,3),t(x,1))= Tglob(t(x,3),t(x,1))+Te(3,1);
    Tglob(t(x,3),t(x,2))= Tglob(t(x,3),t(x,2))+Te(3,2);
    Tglob(t(x,3),t(x,3))= Tglob(t(x,3),t(x,3))+Te(3,3);

    q2glob(t(x,1))= q2glob(t(x,1))+q2e(1);
    q2glob(t(x,2))= q2glob(t(x,2))+q2e(2);
    q2glob(t(x,3))= q2glob(t(x,3))+q2e(3);

end

Sglob= 0.5*(Sglob + Sglob');
Tglob= 0.5*(Tglob + Tglob');
Cglob= 0.5*(Cglob + Cglob');

% Boundary condition
lenouter= length(banodes);
leninner= Nnodes - lenouter;

Sglob= Sglob(1:leninner,1:leninner);
Tglob= Tglob(1:leninner,1:leninner);
q2glob= q2glob(1:leninner);
Cglob= Cglob(1:leninner,1:leninner);

T= -Cglob + Tglob;
T= (T + T')/2;

% Kron reduction
numma= length(manodes);
nummm= length(mmnodes);
numaa= length(aanodes);
Smm= Sglob(1:nummm,1:nummm);
Smb= Sglob(1:nummm,nummm+1:nummm+numma);
Sbb= Sglob(nummm+1:nummm+numma,nummm+1:nummm+numma);
Sba= Sglob(nummm+1:nummm+numma,nummm+1+numma:leninner);
Saa= Sglob(nummm+numma+1:leninner, nummm+numma+1:leninner);
SBB= Sbb - Sba*inv(Saa)*Sba';

numred= numma+nummm;
Sred= [Smm Smb ; Smb' SBB];
Tred= T(1:numred,1:numred);
q2red= q2glob(1:numred);
bred= bcols(1:numred,:);


% System formulation
depth= 0.033 + 0.022;              % depth of system into 3-D
```

```
iTred= inv(Tred);
Amat= -iTred*Sred;
Bmat= iTred*q2red;
Cmat1= 0*bred(:,1)';
Dmat1= 0;
Cmat2= 0*bred(:,1)';
Dmat2= 0;

for x= 1:9
   Cmat1= Cmat1 -depth*bred(:,x)'*iTred*Sred/5.8e7/areabp(x);
   y= x+9;
   Cmat2= Cmat2 + depth*bred(:,y)'*iTred*Sred/5.8e7/areabn(x);
   Dmat1= Dmat1 + depth*(1 + bred(:,x)'*iTred*q2red)/5.8e7/areabp(x);
   Dmat2= Dmat2 + depth*(1 - bred(:,y)'*iTred*q2red)/5.8e7/areabn(x);
end

Cmat= Cmat1+Cmat2;
Dmat= Dmat1+Dmat2;
sys= ss(Amat,Bmat,Cmat,Dmat);
```

D.4 Reduced-order Modeling of HFMEC

D.4.1 HFMEC Formulation of a Toroidal Core

```
function sys_full=mec_sat_full(jar)

%%%%%%%%%%%%%%%%% Geometrical Characteristics, jar is the magnitude of input current

rad_in=46.75/2*1e-3;                    % Inner diameter
rad_out=61.5/2*1e-3;                    % Outter diameter
h=4.7498*1e-4*50;                       % Height

wind_num=76;                            % # of turns
Sigma=200;                              % Conductivity

wire_res=85.76*1e-3;

slice_num=100;

dx=(rad_out-rad_in)/(2*slice_num-1);    % x-axis incremetals
dy=h/(2*slice_num-1);                   % y-axis incrementals

%%%%%%%%%%%%%%%%%%%%%%%%% Slice Area and area_len Calculation

for con=1:slice_num-1
```

```
   areaa(con)=0;
   areaa_len(con)=0;

% Permeance in parallel branches are added for the start side
areaa_len(con)=areaa_len(con)+dx*dy*(2*(slice_num-con)+1)/(2*pi*(rad_in-dx/2+con*dx));

% Permeance in parallel branches are added for the end side
areaa_len(con)=areaa_len(con)+dx*dy*(2*(slice_num-con)+1)/(2*pi*(rad_out+dx/2-con*dx));

areaa(con)=areaa(con)+dx*dy*(2*(slice_num-con)+1)*2;

   for con2=1:2*(slice_num-con)-1
      areaa_len(con)=areaa_len(con)+dx*dy*2/(2*pi*(rad_in+con*dx-dx/2+con2*dx));
      areaa(con)=areaa(con)+dx*dy*2;
   end

end

areaa(slice_num)=dx*dy;
areaa_len(slice_num)=dx*dy/pi*(rad_in+rad_out);

%%%%%%%%%%%%%%%%%%%%%%%%%%%%%%%%%%%   Muu calculation

for con=1:slice_num
      Muu(con)=gor(wind_num,jar,areaa_len(con),areaa(con));
end

%%%%%%%%%%%%%%%%%%%%%%%%%%%%%%%%%%%% Slice Reluctance Calculation

for con=1:slice_num-1

% Permeance in parallel branches are added for the start side
   permeance_start=Muu(con)*dx*dy*(2*(slice_num-con)+1)/(2*pi*(rad_in-dx/2+con*dx));

% Permeance in parallel branches are added for the end side
   permeance_end=Muu(con)*dx*dy*(2*(slice_num-con)+1)/(2*pi*(rad_out+dx/2-con*dx));
   permeance_between=0;

   for con2=1:2*(slice_num-con)-1
         temp=Muu(con)*dx*dy*2/(2*pi*(rad_in+con*dx-dx/2+con2*dx));
         permeance_between=permeance_between+temp;
   end

   permeance(con)=permeance_end+permeance_start+permeance_between;        % Total permeance

   reluc(con)=1/permeance(con);                                            % Total reluctance

end

reluc(slice_num)=(pi*(rad_in+rad_out))/(Muu(con)*dx*dy);                  % Last slice reluctance
```

```
%%%%%%%%%%%%%%%%%%%%%%%% Slice Conductance Calculation

for con=1:slice_num-1

   Resistance_start=dy*(2*(slice_num-con)+1)/(Sigma*dx*2*pi*(rad_in+con*dx-dx/2));
   Ressitance_end=dy*(2*(slice_num-con)+1)/(Sigma*dx*2*pi*(rad_out-con*dx+dx/2));
   Resistance_between=0;

   for con2=1:2*(slice_num-con)-1
         temp=2*dx/(Sigma*dy*(2*pi*(rad_in+con*dx+con2*dx-dx/2)));
         Resistance_between=Resistance_between+temp;
   end

   Resistance(con)=Ressitance_end+Resistance_start+Resistance_between;
   conduc(con)=1/Resistance(con);

end

conduc(slice_num)=0;      % Doesn't matter since doesn't cause any eddy current

%%%%%%%%%%%%%%%%%%%%%%%%%%%%%%%%%%%%%%%%   Full order model formulation

mat_D=[0];
mat_C=zeros(1,slice_num);mat_C(1,1)=reluc(1)/wind_num;mat_C(1,2)=-reluc(1)/wind_num;

mat_B=zeros(slice_num,1);mat_B(1,1)=1/wind_num;
mat_A=zeros(slice_num,slice_num);
mat_A(1,1)=-wire_res*reluc(1)/wind_num/wind_num;
mat_A(1,2)=wire_res*reluc(1)/wind_num/wind_num;

for con=2:slice_num-1
   mat_A(con,con-1)=reluc(con-1)/conduc(con-1);
   mat_A(con,con)=-(reluc(con-1)+reluc(con))/conduc(con-1);
   mat_A(con,con+1)=(reluc(con))/conduc(con-1);
end

   mat_A(slice_num,slice_num-1)=reluc(slice_num-1)/conduc(slice_num-1);
   mat_A(slice_num,slice_num)=-(reluc(slice_num-1)+reluc(slice_num))/conduc(slice_num-1);

sys_full=ss(mat_A,mat_B,mat_C,mat_D)
```

D.4.2 Effective permeability

```
function MM=gor(N,cur,areaa_lent,areaat)

% N is the number of winding, M is the effective Mu, cur is current magnitude,  areaa_len is the flux tube
% area divided by length, areaa is the flux tube area, p are the interpolating coefficients

% Mu versus B are extracted from the data sheet
```

M=[0.00002373486190
0.00006386971345
0.00011844476451
0.00018539020587
0.00030405383441
0.00040703777188
0.00057118223318
0.00085489235813
0.00135335648920
0.00321625458309
0.00553584410620
0.00732732718430
0.00941300833039
0.01041000743758
0.00891231639793
0.00626751427485
0.00626751427485
0.00891231639793
0.01041000743758
0.00941300833039
0.00732732718430
0.00553584410620
0.00321625458309
0.00135335648920
0.00085489235813
0.00057118223318
0.00040703777188
0.00030405383441
0.00018539020587
0.00011844476451
0.00006386971345
0.00002373486190];

B=[-2.1
-2
-1.9
-1.8
-1.7
-1.65
-1.6
-1.55
-1.5
-1.4
-1.3
-1.2
-1
-0.7
-0.4
-0.2
0.2
0.4

```
0.7
1
1.2
1.3
1.4
1.5
1.55
1.6
1.65
1.7
1.8
1.9
2
2.1
];


  function y=fun(x)

        M_int=interp1(B,M,x/areaat,'linear');
        M_int=max(M_int,1.2566e-006);          % Air permeance used for initiaization
        M_int=min(M_int,max(M));
        y=N*cur-x/areaa_lent/M_int;
  end

% finding the effective flux with initial condition from linear material assumption
phi=fsolve(@fun,N*cur*4*pi*1e-7*800*areaa_lent);

MM=interp1(B,M,phi/areaat,'linear');               % Effective permeability

end
```

D.4.3 Lookup table generation

```
con=1;
for x=0:0.1:10                    % current range to be covered

sys_red=mec_sat(x);               % Accepting the reduced-order model
[z,p,k] = ss2zp(sys_red.a,sys_red.b,sys_red.c,sys_red.d);          % generating the gain, pole, and zero

% Poles and zeros are in the left half plane; use abs and then multiply with -1.
z=abs(z);
p=abs(p);

zz(con,1:2)=z;
pp(con,1:3)=p;
kk(con)=k;
```

```
 con=con+1
end

% clean up and sort the numerical data
save num
```

D.4.4 Transient simulation of the nonlinear reduced-order model

```
load num;                       % Load the previously saved lookup tables that parameterized
                                %gain/pole/zeros versus current magnitudes

con=1;
delta=1e-5;                     % Step size for the Backward Euler
xx(:,con)=zeros(5,1);
i(con)=0;
   x=0;
   interpolator;
v(con)=0;

time=0;

for t=0:delta:2
   con=con+1;
   time=[time t];
   v(con)=7.5*sin(120*pi*t);            % sinusoidal or PWM voltage waveform
   x=abs(i(con-1));


   z1=interp1(x_num,z_num(:,1),x,'nearest','extrap');
   z2=interp1(x_num,z_num(:,2),x,'nearest','extrap');

   p1=interp1(x_num,p_num(:,1),x,'nearest','extrap');
   p2=interp1(x_num,p_num(:,2),x,'nearest','extrap');
   p3=interp1(x_num,p_num(:,3),x,'nearest','extrap');


   k=interp1(x_num,k_num,x,'nearest','extrap');

   z=-[z1,z2];
   p=-[p1,p2,p3];
   [A,B,C,D]=zp2ss(z,p,k);

   xx(:,con)=(eye(3)-delta*A)\(xx(:,con-1)+delta*B*v(con));      % Backward Euler
   i(con)=C*xx(:,con)+D*v(con);                                  % Current as the output variable

end
```

D.5 FEM of a Plunger

D.5.1 Fixed grid generation

```
depth=1e-1;                 % Depth into Z-axis
mu0=4*pi*1e-7;              % Free Space Permeability
mur=4000;                   %  Steel Permeability

%%%%%%%%%%%%%%%  First Region
out_len_x=12e-2;            % The containing box in x-axis
out_len_y=2e-1;             % The containing box in y-axis
dx=5e-3;
dy=5e-3;
sec_num_x=out_len_x/dx;      % number of sections in x-axis for a rectangular shape
sec_num_y=out_len_y/dy;      % number of sections in y-axis for a rectangular shape
ele_no=2*sec_num_x*sec_num_y;

x=[];                       % Initializing x-coordinates
y=[];                       % Initializing x-coordinates

for con=1:((sec_num_x+1)*(sec_num_y+1))        % Node enumeration and coordination, from left to
right, then bottom to top, for a rectangular shape
   x=[x dx*rem((con-1),(sec_num_x+1))];
   y=[y dy*floor((con-1)/(sec_num_x+1))];
end

nod_no=(sec_num_x+1)*(sec_num_y+1);     % Total # of nodes generated

% Global Element-Nodal Identification, the order is 1-2-3 locally and CounterClockWise

% Initializing nod_id; nod_id is a n*3 matrix, Each row is an element, and within each rwo there are three
% components refering to nodes 1-2-3 in CounterClockWise order

nod_id=[];

for con=1:ele_no
   if rem(con,2)~=0     % Iff it is an odd element
      temp=floor((con-1)/(2*sec_num_x))*(sec_num_x+1)+(rem(con,2*sec_num_x)+1)/2;
      nod_id=[nod_id;temp temp+1 temp+sec_num_x+1];
   else
      temp=floor((con-1)/(2*sec_num_x))*(sec_num_x+1)+(rem(con-1,2*sec_num_x)+1)/2+1;
      nod_id=[nod_id;temp temp+1+sec_num_x temp+sec_num_x];
   end
end

%%%%%%%%%%  Globalization , First we only have first region
x_glob=x;
y_glob=y;
```

```
nod_glob=nod_id;

%%%%%%%%%%%%%%%  Bottom box- Second area
out_len_x=12e-2;            % The containing box in x-axis
out_len_y=8e-2;             % The containing box in y-axis
x_offset=12e-2;
dx=5e-3;
dy=5e-3;

sec_num_x=out_len_x/dx;      % number of sections in x-axis for a rectangular shape
sec_num_y=out_len_y/dy;      % number of sections in y-axis for a rectangular shape
ele_no=2*sec_num_x*sec_num_y;

x=[];                        % Initializing x-coordinates
y=[];                        % Initializing x-coordinates

% Node enumeration and coordination, from left to right, then bottom to top, for a rectangular shape
for con=1:((sec_num_x+1)*(sec_num_y+1))
   x=[x dx*rem((con-1),(sec_num_x+1))];
   y=[y dy*floor((con-1)/(sec_num_x+1))];
end

nod_no=(sec_num_x+1)*(sec_num_y+1);

nod_id=[];

for con=1:ele_no
   if rem(con,2)~=0     % Iff  it is an odd element
      temp=floor((con-1)/(2*sec_num_x))*(sec_num_x+1)+(rem(con,2*sec_num_x)+1)/2;
      nod_id=[nod_id;temp temp+1 temp+sec_num_x+1];
   else
      temp=floor((con-1)/(2*sec_num_x))*(sec_num_x+1)+(rem(con-1,2*sec_num_x)+1)/2+1;
      nod_id=[nod_id;temp temp+1+sec_num_x temp+sec_num_x];
   end
end

% Now, we have to shift elements to the right for bottom box; remember the
% fixed grid generation is from left to right and bottom to top

x=x+x_offset;

%%%%% Globalization after the second block is added; Remove redundant nodes
k=1;
x_size=length(x);
temp_nod=zeros(x_size,1);

for con=1:x_size                                % Absorb the new node numbering into the global system
        temp_flag=intersect(find(x_glob==x(con)),find(y_glob==y(con)));
        if length(temp_flag)==0
        temp_nod(con)=length(x_glob)+k;
        k=k+1;
```

```
        else
        temp_nod(con)=temp_flag;
        end
end

for con=1:length(nod_id)                    % Absorb the new elemental numbering into the global system
   new_column=temp_nod(nod_id(con,:));
   new_row=new_column';
   nod_glob=[nod_glob;new_row];
end

for con=1:length(temp_nod)                  % Absorb the new xy-coordinates into the global system
   temp_con=temp_nod(con);
   x_glob(temp_con)=x(con);
   y_glob(temp_con)=y(con);
end

%%%%%%%%%%%%%%  Bottom box- Third area

out_len_x=12e-2;          % The containing box in x-axis
out_len_y=4e-2;           % The containing box in y-axis
x_offset=12e-2;
y_offset=8e-2;

dx=4e-3;
dy=1e-3;

sec_num_x=out_len_x/dx;       % number of sections in x-axis for a rectangular shape
sec_num_y=out_len_y/dy;       % number of sections in y-axis for a rectangular shape

ele_no=2*sec_num_x*sec_num_y;

x=[];                 % Initializing x-coordinates
y=[];                 % Initializing x-coordinates

% Node enumeration and coordination, from left to right, then bottom to top, for a rectangular shape
for con=1:((sec_num_x+1)*(sec_num_y+1))
   x=[x dx*rem((con-1),(sec_num_x+1))];
   y=[y dy*floor((con-1)/(sec_num_x+1))];
end

nod_no=(sec_num_x+1)*(sec_num_y+1);

% Global Element-Nodal Identification, the order is 1-2-3 locally and counterclockwise

nod_id=[];
for con=1:ele_no
   if rem(con,2)~=0     % Iff it is an odd element
      temp=floor((con-1)/(2*sec_num_x))*(sec_num_x+1)+(rem(con,2*sec_num_x)+1)/2;
      nod_id=[nod_id;temp temp+1 temp+sec_num_x+1];
   else
```

```
      temp=floor((con-1)/(2*sec_num_x))*(sec_num_x+1)+(rem(con-1,2*sec_num_x)+1)/2+1;
      nod_id=[nod_id;temp temp+1+sec_num_x temp+sec_num_x];
   end
end

x=x+x_offset;
y=y+y_offset;

%%%%%%%%%%%%%%% Globalization after the "third" block (dense) is added

k=1;
x_size=length(x);
temp_nod=zeros(x_size,1);

for con=1:x_size                                % Absorb the new node numbering into the global system
         temp_flag=intersect(find(x_glob==x(con)),find(y_glob==y(con)));
         if length(temp_flag)==0
            temp_nod(con)=length(x_glob)+k;
            k=k+1;
         else
            temp_nod(con)=temp_flag;
         end
end

for con=1:length(nod_id)                    % Absorb the new elemental numbering into the global system
   new_column=temp_nod(nod_id(con,:));
   new_row=new_column';
   nod_glob=[nod_glob;new_row];
end

for con=1:length(temp_nod)                  % Absorb the new xy-coordinates into the global system
   temp_con=temp_nod(con);
   x_glob(temp_con)=x(con);
   y_glob(temp_con)=y(con);
end

%%%%%%%%%%%%%%%  Top box- Fourth area

out_len_x=12e-2;          % The containing box in x-axis
out_len_y=8e-2;           % The containing box in y-axis
x_offset=12e-2;
y_offset=12e-2;

dx=5e-3;
dy=5e-3;

sec_num_x=out_len_x/dx;       % number of sections in x-axis for a rectangular shape
sec_num_y=out_len_y/dy;       % number of sections in y-axis for a rectangular shape

ele_no=2*sec_num_x*sec_num_y;
```

```
x=[];                   % Initializing x-coordinates
y=[];                   % Initializing x-coordinates

for con=1:((sec_num_x+1)*(sec_num_y+1))        % Node enumeration and coordination, from left to
                                                %  right, then bottom to top, for a rectangular shape
   x=[x dx*rem((con-1),(sec_num_x+1))];
   y=[y dy*floor((con-1)/(sec_num_x+1))];
end

nod_no=(sec_num_x+1)*(sec_num_y+1);

% Global Element-Nodal Identification, the order is 1-2-3 locally and counterclockwise

nod_id=[];         % nod_id is a n*3 matrix, providing overall nodal equation for each element

for con=1:ele_no

    if rem(con,2)~=0     % Iff it is an odd element
      temp=floor((con-1)/(2*sec_num_x))*(sec_num_x+1)+(rem(con,2*sec_num_x)+1)/2;
      nod_id=[nod_id;temp temp+1 temp+sec_num_x+1];
   else
      temp=floor((con-1)/(2*sec_num_x))*(sec_num_x+1)+(rem(con-1,2*sec_num_x)+1)/2+1;
      nod_id=[nod_id;temp temp+1+sec_num_x temp+sec_num_x];
   end

end

x=x+x_offset;
y=y+y_offset;

%%%%%%%%%%%%%%%% Globalization after the "Fourth" block (dense) is added

k=1;
x_size=length(x);
temp_nod=zeros(x_size,1);

for con=1:x_size
         temp_flag=intersect(find(x_glob==x(con)),find(y_glob==y(con)));
            if length(temp_flag)==0
            temp_nod(con)=length(x_glob)+k;
            k=k+1;
         else
            temp_nod(con)=temp_flag;
         end
end

for con=1:length(nod_id)
   new_column=temp_nod(nod_id(con,:));
   new_row=new_column';
   nod_glob=[nod_glob;new_row];
end
```

```
for con=1:length(temp_nod)
   temp_con=temp_nod(con);
   x_glob(temp_con)=x(con);
   y_glob(temp_con)=y(con);
end

%%%%%%%%%%%%%%%
```

D.5.2 Global C matrix and b vectors

```
function [C_glob,mat_b]= b_vecs(x_glob,y_glob,nod_glob)

% Building two b-vectors
% The final product is checked to see if it is in the copper area, and if so, which one!(+/-).
% is a nod*2 Matrix; The elemental C_1 and C_2 are 3*nod; The final C matrix is nod *no

cond_copper=5.8e7;                    % Assumed conductivity of the copper
wire_area=4*1e-4;

nod_no=length(x_glob);                % number of nodes
ele_no=length(nod_glob);              % Number of elements

mat_b=zeros(nod_no,2);
C_glob=zeros(nod_no,nod_no);

                                      % Building b-vectors
for con=1:ele_no

  n1=nod_glob(con,1);
  n2=nod_glob(con,2);
  n3=nod_glob(con,3);

  x1=x_glob(n1);
  x2=x_glob(n2);
  x3=x_glob(n3);

  y1=y_glob(n1);
  y2=y_glob(n2);
  y3=y_glob(n3);

  A=0.5*abs(det([1 x1 y1;1 x2 y2;1 x3 y3]));

                                      % Check for the copper area

 if ((x1>=2e-2)&(x1<=3e-2))&((x2>=2e-2)&(x2<=3e-2))&((x3>=2e-2)&(x3<=3e-2))&((y1>=8e-
2)&(y1<=12e-2))&((y2>=8e-2)&(y2<=12e-2))&((y3>=8e-2)&(y3<=12e-2))
```

```
    A=A*cond_copper/3;                  % Copper
    mat_b(n1,1)=mat_b(n1,1)+A;
    mat_b(n2,1)=mat_b(n2,1)+A;
    mat_b(n3,1)=mat_b(n3,1)+A;

 elseif ((x1>=7e-2)&(x1<=8e-2))&((x2>=7e-2)&(x2<=8e-2))&((x3>=7e-2)&(x3<=8e-2))&((y1>=8e-
2)&(y1<=12e-2))&((y2>=8e-2)&(y2<=12e-2))&((y3>=8e-2)&(y3<=12e-2))

    A=A*cond_copper/3;                  % Copper
    mat_b(n1,2)=mat_b(n1,2)+A;
    mat_b(n2,2)=mat_b(n2,2)+A;
    mat_b(n3,2)=mat_b(n3,2)+A;

 end

end


C_1=[1;1;1]*mat_b(:,1)';
C_2=[1;1;1]*mat_b(:,2)';


                                % Building C_global
for con=1:ele_no

  n1=nod_glob(con,1);
  n2=nod_glob(con,2);
  n3=nod_glob(con,3);

  x1=x_glob(n1);
  x2=x_glob(n2);
  x3=x_glob(n3);

  y1=y_glob(n1);
  y2=y_glob(n2);
  y3=y_glob(n3);

 A=0.5*abs(det([1 x1 y1;1 x2 y2;1 x3 y3]));
                                                % Check for the copper area

 if ((x1>=2e-2)&(x1<=3e-2))&((x2>=2e-2)&(x2<=3e-2))&((x3>=2e-2)&(x3<=3e-2))&((y1>=8e-
2)&(y1<=12e-2))&((y2>=8e-2)&(y2<=12e-2))&((y3>=8e-2)&(y3<=12e-2))

                                                % The first matrx C_1 is incorporated
    C_glob(n1,:)= C_glob(n1,:) + A*C_1(1,:)/wire_area/3;
    C_glob(n2,:)= C_glob(n2,:) + A*C_1(2,:)/wire_area/3;
    C_glob(n3,:)= C_glob(n3,:) + A*C_1(3,:)/wire_area/3;

 elseif ((x1>=7e-2)&(x1<=8e-2))&((x2>=7e-2)&(x2<=8e-2))&((x3>=7e-2)&(x3<=8e-2))&((y1>=8e-
2)&(y1<=12e-2))&((y2>=8e-2)&(y2<=12e-2))&((y3>=8e-2)&(y3<=12e-2))
```

```
                                                % The second matrx C_2 is incorporated
    C_glob(n1,:)= C_glob(n1,:) + A*C_2(1,:)/wire_area/3;
    C_glob(n2,:)= C_glob(n2,:) + A*C_2(2,:)/wire_area/3;
    C_glob(n3,:)= C_glob(n3,:) + A*C_2(3,:)/wire_area/3;

  end
end
```

D.5.3 Node grouping

```
function [metal,bound,air,outter,new_order]= nod_group(k,x_glob,y_glob)

% Finding the global node locations and their coordinates
% K is the x-axis shift


nod_no=length(x_glob);

x_shift=k*5e-3;
                        % Initialize the node numbering
nod_no=length(x_glob);

outter_nod=unique([find(x_glob==0) find(x_glob==24e-2) find(y_glob==0) find(y_glob==20e-2)]);

metal_nod=unique([find(2e-2<=x_glob & x_glob<=3e-2 & 8e-2<=y_glob & y_glob<=12e-2) find(7e-
2<=x_glob & x_glob<=8e-2 & 8e-2<=y_glob & y_glob<=12e-2) find(3e-2<=x_glob & x_glob<=7e-2 &
1.5e-2<=y_glob & y_glob<=18.5e-2) find(7e-2<=x_glob & x_glob<=12e-2 & 1.5e-2<=y_glob &
y_glob<=5.5e-2) find(7e-2<=x_glob & x_glob<=12e-2 & 14.5e-2<=y_glob & y_glob<=18.5e-2)
find(12e-2<=x_glob & x_glob<=16e-2 & 1.5e-2<=y_glob & y_glob<=8.3e-2) find(12e-2<=x_glob &
x_glob<=16e-2 & 11.7e-2<=y_glob & y_glob<=18.5e-2) find((x_shift+12e-2)<=x_glob &
x_glob<=(x_shift+18e-2) & 8.5e-2<=y_glob & y_glob<=11.5e-2)]);

bound_nod=unique([find(3e-2<=x_glob & x_glob<=16e-2 & y_glob==1.5e-2) find(3e-2<=x_glob &
x_glob<=16e-2 & y_glob==18.5e-2) find(7e-2<=x_glob & x_glob<=12e-2 & y_glob==5.5e-2) find(7e-
2<=x_glob & x_glob<=12e-2 & y_glob==14.5e-2) find(5.5e-2<=y_glob & y_glob<=8e-2 & x_glob==7e-
2) find(12e-2<=y_glob & y_glob<=14.5e-2 & x_glob==7e-2) find(12e-2<=y_glob & y_glob<=18.5e-2 &
x_glob==3e-2) find(1.5e-2<=y_glob & y_glob<=8e-2 & x_glob==3e-2) find(8e-2<=y_glob &
y_glob<=12e-2 & x_glob==2e-2) find(8e-2<=y_glob & y_glob<=12e-2 & x_glob==8e-2) find(2e-
2<=x_glob & x_glob<=3e-2 & y_glob==8e-2) find(7e-2<=x_glob & x_glob<=8e-2 & y_glob==8e-2)
find(2e-2<=x_glob & x_glob<=3e-2 & y_glob==12e-2) find(7e-2<=x_glob & x_glob<=8e-2 &
y_glob==12e-2) find(5.5e-2<=y_glob & y_glob<=8.3e-2 & x_glob==12e-2) find(11.7e-2<=y_glob &
y_glob<=14.5e-2 & x_glob==12e-2) find(1.5e-2<=y_glob & y_glob<=8.3e-2 & x_glob==16e-2)
find(11.7e-2<=y_glob & y_glob<=18.5e-2 & x_glob==16e-2) find(12e-2<=x_glob & x_glob<=16e-2 &
y_glob==8.3e-2) find(12e-2<=x_glob & x_glob<=16e-2 & y_glob==11.7e-2) find((12e-
2+x_shift)<=x_glob & x_glob<=(18e-2+x_shift) & y_glob==8.5e-2) find((12e-2+x_shift)<=x_glob &
x_glob<=(18e-2+x_shift) & y_glob==11.5e-2) find(8.5e-2<=y_glob & y_glob<=11.5e-2 &
x_glob==(12e-2+x_shift)) find(8.5e-2<=y_glob & y_glob<=11.5e-2 & x_glob==(18e-2+x_shift))]);
```

```
metal_metal_nod=setdiff(metal_nod,bound_nod);

non_air_nod=unique(union(outter_nod,union(bound_nod,metal_nod)));

air_air_nod=setdiff([1:nod_no],non_air_nod);

metal=metal_metal_nod;
bound=bound_nod;
air=air_air_nod;
outter=outter_nod;

new_order=[metal,bound,air,outter];
```

D.5.4 Node renumbering

```
function [newx,newy,newele]= nod_ren(x,y,ele,order)

 % node renumbering and restructuring
newx=x(order);
newy=y(order);

for con1=1:length(ele)

   for con2=1:3
      con3=ele(con1,con2);
      con4=find(order==con3);
      newele(con1,con2)=con4;
   end

end
```

D.5.5 Elemental matrix T

```
function ele_t = T_ele(n1,n2,n3,k,x_glob,y_glob)

% n1,n2,n3 are the nodal numbers of the corresponding element in 1,2,3 order

cond_steel=80;                  % Assumed conductivity of the steel ferrite
cond_copper=5.8e7;              % Assumed conductivity of the copper

x_shift=k*5e-3;                  % Shift in plunger; our discreet movement step-size is 4 mm.

  x1=x_glob(n1);
  x2=x_glob(n2);
  x3=x_glob(n3);
```

```
   y1=y_glob(n1);
   y2=y_glob(n2);
   y3=y_glob(n3);

   A=0.5*abs(det([1 x1 y1;1 x2 y2;1 x3 y3]));

% Initializ the T-matrix
   ele_t=A/12*(ones(3,3)+eye(3,3));


   % Including the conductivity of steel, copper, and air

  if ((x1>=3e-2)&(x1<=16e-2))&((x2>=3e-2)&(x2<=16e-2))&((x3>=3e-2)&(x3<=16e-2))&((y1>=1.5e-
2)&(y1<=5.5e-2))&((y2>=1.5e-2)&(y2<=5.5e-2))&((y3>=1.5e-2)&(y3<=5.5e-2))

      ele_t=ele_t*cond_steel;      % Steel

  elseif ((x1>=3e-2)&(x1<=7e-2))&((x2>=3e-2)&(x2<=7e-2))&((x3>=3e-2)&(x3<=7e-2))&((y1>=5.5e-
2)&(y1<=14.5e-2))&((y2>=5.5e-2)&(y2<=14.5e-2))&((y3>=5.5e-2)&(y3<=14.5e-2))

      ele_t=ele_t*cond_steel;      % Steel

 elseif ((x1>=3e-2)&(x1<=16e-2))&((x2>=3e-2)&(x2<=16e-2))&((x3>=3e-2)&(x3<=16e2))&((y1>=
14.5e-2)&(y1<=18.5e-2))&((y2>=14.5e-2)&(y2<=18.5e-2))&((y3>=14.5e-2)&(y3<=18.5e-2))

      ele_t=ele_t*cond_steel;      % Steel

  elseif ((x1>=12e-2)&(x1<=16e-2))&((x2>=12e-2)&(x2<=16e-2))&((x3>=12e-2)&(x3<=16e-2))&((
y1>=5.5e-2)&(y1<=8.3e-2))&((y2>=5.5e-2)&(y2<=8.3e-2))&((y3>=5.5e-2)&(y3<=8.3e-2))

      ele_t=ele_t*cond_steel;      % Steel

  elseif ((x1>=12e-2)&(x1<=16e-2))&((x2>=12e-2)&(x2<=16e-2))&((x3>=12e-2)&(x3<=16e-2))&((
y1>=11.7e-2) &(y1<= 14.5e-2))&((y2>=11.7e-2)&(y2<=14.5e-2))&((y3>=11.7e-2)&(y3<=14.5e-2))

      ele_t=ele_t*cond_steel;      % Steel

  elseif ((x1>=(12e-2+x_shift))&(x1<=(18e-2+x_shift)))&((x2>=(12e-2+x_shift))&(x2<=(18e-2+x_shift
)))&((x3>=(12e-2+x_shift))&(x3<=(18e-2+x_shift)))&((y1>=8.5e-2)&(y1<=11.5e-2))&((y2>=8.5e-2)&
(y2<=11.5e-2))&((y3>=8.5e-2)&(y3<=11.5e-2))

      ele_t=ele_t*cond_steel;      % Steel

  elseif ((x1>=2e-2)&(x1<=3e-2))&((x2>=2e-2)&(x2<=3e-2))&((x3>=2e-2)&(x3<=3e-2))&((y1>=8e-
2)&(y1<=12e-2))&((y2>=8e-2)&(y2<=12e-2))&((y3>=8e-2)&(y3<=12e-2))

      ele_t=ele_t*cond_copper;     % Copper

  elseif ((x1>=7e-2)&(x1<=8e-2))&((x2>=7e-2)&(x2<=8e-2))&((x3>=7e-2)&(x3<=8e-2))&((y1>=8e-
2)&(y1<=12e-2))&((y2>=8e-2)&(y2<=12e-2))&((y3>=8e-2)&(y3<=12e-2))
```

```
    ele_t=ele_t*cond_copper;     % Copper

  else

    ele_t=ele_t*0;              % Air

  end
```

D.5.6 Elemental matrix S

```
function ele_s = s_ele(n1,n2,n3,k,x_glob,y_glob)

% Building elemental matrix
% n1,n2,n3 are the nodal numbers of the corresponding element in 1,2,3 order
% K is the shift made in the plunger (k*4e-3 is the mechanical shift)

mu0=4*pi*1e-7;                  % Free Space Permeability
mur=4000;                       % Steel Permeability

x_shift=k*5e-3;                 % Shift in plunger

   x1=x_glob(n1);
   x2=x_glob(n2);
   x3=x_glob(n3);

   y1=y_glob(n1);
   y2=y_glob(n2);
   y3=y_glob(n3);

   a1=x2*y3-x3*y2;
   b1=y2-y3;
   c1=x3-x2;

   a2=x3*y1-x1*y3;
   b2=y3-y1;
   c2=x1-x3;

   a3=x1*y2-x2*y1;
   b3=y1-y2;
   c3=x2-x1;

   A=0.5*abs(det([1 x1 y1;1 x2 y2;1 x3 y3]));

  ele_s=0.25/A/mu0*[(b1^2+c1^2) (b1*b2+c1*c2) (b1*b3+c1*c3);(b1*b2+c1*c2) (b2^2+c2^2)
(b2*b3+c2*c3);(b1*b3+c1*c3) (b2*b3+c2*c3) (b3^2+c3^2)];
                                                        % Here we check for the steel
if ((x1>=3e-2)&(x1<=16e-2))&((x2>=3e-2)&(x2<=16e-2))&((x3>=3e-2)&(x3<=16e-2))&((y1>=1.5e-
2)&(y1<=5.5e-2))&((y2>=1.5e-2)&(y2<=5.5e-2))&((y3>=1.5e-2)&(y3<=5.5e-2))
```

```
    ele_s=ele_s/mur;

 elseif ((x1>=3e-2)&(x1<=7e-2))&((x2>=3e-2)&(x2<=7e-2))&((x3>=3e-2)&(x3<=7e-2))&((y1>=5.5e-
2)&(y1<=14.5e-2))&((y2>=5.5e-2)&(y2<=14.5e-2))&((y3>=5.5e-2)&(y3<=14.5e-2))

    ele_s=ele_s/mur;

 elseif ((x1>=3e-2)&(x1<=16e-2))&((x2>=3e-2)&(x2<=16e-2))&((x3>=3e-2)&(x3<=16e-2))&((y1>=
14.5e-2)&(y1<=18.5e-2))&((y2>=14.5e-2)&(y2<=18.5e-2))&((y3>=14.5e-2)&(y3<=18.5e-2))

    ele_s=ele_s/mur;

 elseif ((x1>=12e-2)&(x1<=16e-2))&((x2>=12e-2)&(x2<=16e-2))&((x3>=12e-2)&(x3<=16e-
2))&((y1>=5.5e-2)&(y1<=8.3e-2))&((y2>=5.5e-2)&(y2<=8.3e-2))&((y3>=5.5e-2)&(y3<=8.3e-2))

   ele_s=ele_s/mur;

 elseif ((x1>=12e-2)&(x1<=16e-2))&((x2>=12e-2)&(x2<=16e-2))&((x3>=12e-2)&(x3<=16e-2))&((y1
>=11.7e-2)&(y1<=14.5e-2))&((y2>=11.7e-2)&(y2<=14.5e-2))&((y3>=11.7e-2)&(y3<=14.5e-2))

   ele_s=ele_s/mur;

 elseif ((x1>=(12e-2+x_shift))&(x1<=(18e-2+x_shift)))&((x2>=(12e-2+x_shift))&(x2<=(18e-
2+x_shift)))&((x3>=(12e-2+x_shift))&(x3<=(18e-2+x_shift)))&((y1>=8.5e-2)&(y1<=11.5e-
2))&((y2>=8.5e-2)&(y2<=11.5e-2))&((y3>=8.5e-2)&(y3<=11.5e-2))

    ele_s=ele_s/mur;
 end
```

D.5.7 Elemental matrix P

```
function ele_p = p_ele(n1,n2,n3,x_glob,y_glob)

% Building elemental p- matrix
% n1,n2,n3 are the nodal numbers of the corresponding element in 1,2,3 order
% The final product is checked to see if we are in the copper area (positive for the left-side copper,
% negative for the right-side copper).
% We do not need to consider the shift,
% since there is no wire on the moving part

  wire_area=4*1e-4;            % Wire area for each 1cm * 4 cm copper plates;

  x1=x_glob(n1);
  x2=x_glob(n2);
  x3=x_glob(n3);
```

```
   y1=y_glob(n1);
   y2=y_glob(n2);
   y3=y_glob(n3);

   p=[(y2-y3);(y3-y1);(y1-y2)];
   q=[(x3-x2);(x1-x3);(x2-x1)];

   A=0.5*(p(2)*q(3)-p(3)*q(2));

% Initializ the p-matrix, current direction will be taken into account later based on the coordinates

   ele_p=A/3/wire_area*(ones(3,1));

 % Finding the wires and current polarities

  if ((x1>=2e-2)&(x1<=3e-2))&((x2>=2e-2)&(x2<=3e-2))&((x3>=2e-2)&(x3<=3e-2))&((y1>=8e-
2)&(y1<=12e-2))&((y2>=8e-2)&(y2<=12e-2))&((y3>=8e-2)&(y3<=12e-2))

      ele_p=ele_p;                    % Positive current

  elseif ((x1>=7e-2)&(x1<=8e-2))&((x2>=7e-2)&(x2<=8e-2))&((x3>=7e-2)&(x3<=8e-2))&((y1>=8e-
2)&(y1<=12e-2))&((y2>=8e-2)&(y2<=12e-2))&((y3>=8e-2)&(y3<=12e-2))

      ele_p=-1*ele_p;                 % Negative Copper

  else

      ele_p=ele_p*0;                  % Air

  end
```

D.5.8 State model formulation

```
function [A,B,C,D]= dis_state_model(P_g,C_g,S_g,T_g,b1,b2,nod_seg)

% nod_seg=[metal,bound,air,outter]
% Here are the system parameters

depth=1e-1;                         % Depth into Z-axis
wide=4e-2;                          % The leg width used in the compensation for the corner effect
L=wide+depth;                       % The effective depth including the corner effects
wire_cond=5.8e7;                    % The conductivity is assumed the same for both sides of wires
wire_area=4e-4;                     % The area at each side
r_ext=0.02;                         % 20 m-Ohm
cond_copper=5.8e7;                  % Copper conductivity
```

```
T_g=T_g-C_g;
T_g=(T_g+T_g')/2;

 Smm=S_g(1:nod_seg(1),1:nod_seg(1));
 Smb=S_g(1:nod_seg(1),nod_seg(1)+1:nod_seg(1)+nod_seg(2));
 Sbb=S_g(nod_seg(1)+1:nod_seg(1)+nod_seg(2),nod_seg(1)+1:nod_seg(1)+nod_seg(2));
 Sba=S_g(nod_seg(1)+1:nod_seg(1)+nod_seg(2),nod_seg(1)+nod_seg(2)+1:sum(nod_seg)-nod_seg(4));
 Saa=S_g(nod_seg(1)+nod_seg(2)+1:sum(nod_seg)-

nod_seg(4),nod_seg(1)+nod_seg(2)+1:sum(nod_seg)-nod_seg(4));

 SBB=Sbb-Sba*inv(Saa)*Sba';

 Sred=[Smm Smb;Smb' SBB];
 Tred=T_g(1:nod_seg(1)+nod_seg(2),1:nod_seg(1)+nod_seg(2));


 inv_Tred=inv(Tred);

 Pred=P_g(1:nod_seg(1)+nod_seg(2));

b1red=b1(1:nod_seg(1)+nod_seg(2));
 b2red=b2(1:nod_seg(1)+nod_seg(2));

 % System matrix extraction
  A=-inv_Tred*Sred;
  B=inv_Tred*Pred;
  C=L/cond_copper/wire_area*(-b1red'*inv_Tred*Sred+b2red'*inv_Tred*Sred);
  D=r_ext+L/cond_copper/wire_area*(2+b1red'*inv_Tred*Pred-b2red'*inv_Tred*Pred);
```

D.5.9 Plunger full and reduced model generation

```
%%% Plunger Modeling with a fixed grid; The movement is discretized in 0.5 cm segments


function [sys,rsys]=plunger(seg);

grid_gen;                                          % Generates the fixed grid

nod_no=length(x_glob);
ele_no=length(nod_glob);

% Node numbering is sorted
[metal,bound,air,outter,new_order]=nod_group(seg,x_glob,y_glob);
nod_seg=[length(metal),length(bound),length(air),length(outter)];

% Sorted global x,y,element list
[x_glob,y_glob,nod_glob]=nod_ren(x_glob,y_glob,nod_glob,new_order);
```

```
s_global=sparse(nod_no,nod_no);                 % Initialization the global S matrix
T_global=sparse(nod_no,nod_no);                 % Initialization the global T matrix
p_global=sparse(nod_no,1);                      % Initialization the global P matrix

for con=1:ele_no

  nod1=nod_glob(con,1);                         % Finding the overall nodes of the corresponding element
  nod2=nod_glob(con,2);
  nod3=nod_glob(con,3);

  ele_tem_t=T_ele(nod1,nod2,nod3,seg,x_glob,y_glob);    % Create the temporary elemental T matrix
  ele_tem_s=s_ele(nod1,nod2,nod3,seg,x_glob,y_glob);    % Create the temporary elemental S matrix
  ele_tem_p=p_ele(nod1,nod2,nod3,x_glob,y_glob);        % Create the temporary elemental P matrix

%%%% Creating the global T matrix

  T_global(nod1,nod1)=T_global(nod1,nod1)+ele_tem_t(1,1);
  T_global(nod1,nod2)=T_global(nod1,nod2)+ele_tem_t(1,2);
  T_global(nod1,nod3)=T_global(nod1,nod3)+ele_tem_t(1,3);

  T_global(nod2,nod1)=T_global(nod2,nod1)+ele_tem_t(2,1);
  T_global(nod2,nod2)=T_global(nod2,nod2)+ele_tem_t(2,2);
  T_global(nod2,nod3)=T_global(nod2,nod3)+ele_tem_t(2,3);

  T_global(nod3,nod1)=T_global(nod3,nod1)+ele_tem_t(3,1);
  T_global(nod3,nod2)=T_global(nod3,nod2)+ele_tem_t(3,2);
  T_global(nod3,nod3)=T_global(nod3,nod3)+ele_tem_t(3,3);

%%%% Creating the global S matrix

  s_global(nod1,nod1)=s_global(nod1,nod1)+ele_tem_s(1,1);
  s_global(nod1,nod2)=s_global(nod1,nod2)+ele_tem_s(1,2);
  s_global(nod1,nod3)=s_global(nod1,nod3)+ele_tem_s(1,3);

  s_global(nod2,nod1)=s_global(nod2,nod1)+ele_tem_s(2,1);
  s_global(nod2,nod2)=s_global(nod2,nod2)+ele_tem_s(2,2);
  s_global(nod2,nod3)=s_global(nod2,nod3)+ele_tem_s(2,3);

  s_global(nod3,nod1)=s_global(nod3,nod1)+ele_tem_s(3,1);
  s_global(nod3,nod2)=s_global(nod3,nod2)+ele_tem_s(3,2);
  s_global(nod3,nod3)=s_global(nod3,nod3)+ele_tem_s(3,3);

%%%% Creating the global P matrix

  p_global(nod1)=p_global(nod1)+ele_tem_p(1);
  p_global(nod2)=p_global(nod2)+ele_tem_p(2);
  p_global(nod3)=p_global(nod3)+ele_tem_p(3);

end
```

```
s_global=0.5*(s_global+s_global');
T_global=0.5*(T_global+T_global');

[C_glob,mat_b]= b_vecs(x_glob,y_glob,nod_glob);                    % Global C-matrix and b1,b2-vectors

b1=mat_b(:,1);
b2=mat_b(:,2);

% State-Model Extraction
[A,B,C,D]= dis_state_model(p_global,C_glob,s_global,T_global,b1,b2,nod_seg);

%  Model-Order Reduction; different linear reduction techniques can be applied

sys=ss(A,B,C,D);

sys1=ssbal(sys);

[z,p,k]=ss2zp(sys1.a,sys1.b,sys1.c,sys1.d);
sys2=zpk(z,p,k);

sys3=minreal(sys2,1e-6);

z=zero(sys3);
p=pole(sys3);
k=dcgain(sys3);

sys3=zp2ss(z,p,k);
sys3=minreal(sys2,1e-6);
sys3=sys3*dcgain(sys2)/dcgain(sys3);

[sys4,G] = balreal(sys3);                    % Balanced realization

 rsys = modred(sys4,4:size(G));              % Adjusting the bandwidth
```

REFERENCES

[1] M. Rahimi and A. Emadi, "An analytical investigation of dc/dc power electronic converters with constant power loads in vehicular power systems," *IEEE Transactions on Vehicular Technology*, vol. 7, pp. 2689-2702, July 2009.

[2] M. Amrhein and P. T. Krein, "Dynamic simulation for anaysis of hybrid electric vehicle system and subsystem interactions, including power electronics," *IEEE Transactions on Vehicular Technology*, vol. 54, pp. 825-836, May 2005.

[3] M. Andrus, M. Steurer, C. Edrington, and F. Bogdan, "Real-time simulation-based design of a power-hardware-in-the-loop setup to support studies of shipboard MVDC issues," in *Proc. Electric Ship Technologies Symposium*, 2009, pp. 142-151.

[4] D. Cottet, "Industry perspective on multi domain simulation and virtual prototyping," in *Proc. 11th IEEE Workshop on Computer Application in Power Electronics,* 2008, pp. 1-6.

[5] J. R. Brauer, "Time-varying resistors, capacitors, and inductors in nonlinear transient finite element models," *IEEE Transactions on Magnetics*, vol. 34, pp. 3086-3089, Sept. 1998.

[6] M. Cotorogea, "Physics-based SPICE-model for IGBTs with transparent emitter," *IEEE Transactions on Power Electronics*, vol. 24, pp. 2821-2832, Dec. 2009.

[7] R. Chibante, A. Armando, and A. Carvalho, "Finite-element modeling and optimization-based parameter extraction algorithm for NPT-IGBTs," *IEEE Transactions on Power Electronics*, vol. 24, pp. 1417-1427, May 2009.

[8] S. Rael and B. Davat, "A physics-based modeling of interelectrode MOS capacitances of power MOSFET and IGBT," *IEEE Transactions on Power Electronics*, vol. 23, pp. 2585-2594, Sept. 2008.

[9] C. L. Ma, P. O. Lauritzen, and J. Sigg, "Modeling of power diodes with the lumped-charge modeling technique," *IEEE Transactions on Power Electronics*, vol. 12, pp. 398-405, May 1997.

[10] G. M. Buiatti, F. Cappelluti, and G. Ghione, "Physics-based PiN diode spice model for power-circuit simulation," *IEEE Transactions on Industry Applications*, vol. 43, pp. 911-919, July-Aug. 2007.

[11] A. T. Bryant, X. Kang, E. Santi, P. R. Palmer, and J. L. Hufgins, "Two-step parameter extraction procedure with formal optimization for physics-based circuit simulator IGBT and p-i-n diode models," *IEEE Transactions on Power Electronics*, vol. 21, pp. 295-309, March 2006.

[12] A. F. Witulski, "Introduction to modeling of transformers and coupled inductors," *IEEE Transactions on Power Electronics*, vol. 10, pp. 349-357, May 1995.

[13] T. C. O'Connell, P. T. Krein, M. Yilmaz, and A. Friedl, "On the feasibility of using large-scale numerical electric machine field analysis software in complex electric drive system design tools," in *Proc. 11th IEEE Workshop on Control and Modeling in Power Electronics*, 2008, pp. 1-8.

[14] P. Bauer and P. J. VanDuijsen, "Challenges and advances in simulation," in *Proc. 36th IEEE Power Electronics Specialists Conference*, 2005, pp. 1030-1036.

[15] R. J. Kerkman, "Twenty years of PWM AC drives: When secondary issues become primary concerns," in *Proc. 22nd International Conference on Industrial Electronics*, 1996, pp. LVII-LXIII.

[16] A. Davoudi and P. L. Chapman, "Summary of recent work on reduction techniques applied to electromechanical modeling," in *Proc. IEEE Electric Ship Technologies Symposium*, 2007, pp. 363-370.

[17] A. Davoudi, A. Khaligh, M. Amrhein, P. L. Chapman, and J. Jatskevich, "Low-order dynamic magnetic equivalent circuits of saturated steel laminations," in *Proc. Vehicular Power and Propulsion Conference*, 2007, pp. 725-729.

[18] A. Davoudi, S. V. Dhople, P. L. Chapman, and J. Jatskevich, "Variable-resolution simulation of nonlinear power circuits," in *Proc. IEEE International Symposium on Circuits and Systems*, submitted for publication.

[19] A. Davoudi and P. Chapman, "Reduced-order modeling of high-fidelity magnetic equivalent circuits," *IEEE Transactions on Power Electronics*, vol. 24, pp. 2847-2855, Dec. 2009.

[20] A. Davoudi, P. L. Chapman, and J. Jatskevich, "Nonlinear order reduction in dynamics magnetic equivalent circuits of electromagnetic actuators: Incorporating relative motion and back EMF," in *Proc. 39th IEEE Power Electronics Specialists Conference*, 2008, pp. 3992-3995.

[21] A. Davoudi, P. L. Chapman, and J. Jatskevich, "Multi-resolution simulation of PWM Dc-Dc converters," in *Proc. IEEE International Telecommunications Energy Conference*, 2008, pp. 1-7.

[22] A. Davoudi and P. L. Chapman, "A general framework for automated physics-based reduced-order modeling of electromechanical system," in *Proc. Summer Computer Simulation Conference*, 2007, pp. 221-228.

[23] A. Davoudi and P. L. Chapman, "Eddy current modeling with order reduction in dynamic magnetic equivalent circuits," in *Proc. 38th IEEE Power Electronics Specialists Conference*, 2007, pp. 2069-2074.

[24] Y. Chen, A. Davoudi, and P. L. Chapman, "Multifrequency modeling of a multiple-input dc-dc converter," in *Proc. 39th IEEE Power Electronics Specialists Conference*, 2008, pp. 4604-4610.

[25] I. Newton, *Optics*. London, England, 1704.

[26] B. Taylor, *Methodus Incrementorum Directa et Inverse*. London, England, 1715.

[27] L. Euler, *Institutiones Calculi Differentiatis*. St. Petersburg, Russia, 1755.

[28] J. L. Lagrange, *Theories des Fonctions Analytiques*. Paris, France, 1759.

[29] H. Pade, "Sur la representation approchee d'une fonction par des fractions rationelles," Philosophy of Doctorate, Mathematics, Sorbonne, Paris, France, 1982.

[30] C. Lanczos, "An iteration method for the solution of the eigenvalue problem of linear differential and integral operators," *Research of the National Bureau of Standards,* vol. 45, pp. 255-282, 1950.

[31] W. E. Arnoldi, "The principle of minimized iterations in the solution of the matrix eigenvalue problem," *Quarterly Journal of Applied Mathematics,* vol. 9, pp. 17-29, 1951.

[32] R. Fletcher, "Conjugate gradient methods for indefinite systems," in *Lecture Notes in Mathematics,* vol. 506, *Numerical Analysis:Proceedings of the Dundee Conference on Numerical Analysis*, 1975, G. A. Watson, Ed. Berlin, Germany: Springer-Verlag, 1976, pp. 73-89.

[33] Y. Saad and M. H. Schultz, "GMRES: A generalized minimal residual algorithm for solving nonsymmetric linear systems," *SIAM Journal on Scientific and Statistical Computing,* vol. 7, pp. 856-869, 1986.

[34] B. C. Moore, "Principal component analysis in linear systems: Controllability, observability, and model reduction," *IEEE Transactions on Automatic Control,* vol. 26, pp. 17-32, 1981.

[35] K. Glover, "All optimal Hankel-norm approximations of linear multivariable systems and their L∞-error bounds," *International Journal of Control,* vol. 39, pp. 1115-1193, 1984.

[36] L. Sirovich, "Turbulence and the dynamics of coherent structures. Part I: Coherent structures," *Quarterly of Applied Mathematics,* vol. 45, pp. 561-571, 1987.

[37] L. T. Pillage and R. A. Rohrer, "Asymptotic waveform evaluation for timing analysis," *IEEE Transactions on Computer-Aided Design,* vol. 9, pp. 352-366, April 1990.

[38] P. Feldmann and R. W. Freund, "Efficient linear circuit analysis by Pade approximation via the Lanczos process," *IEEE Transactions on Computer-Aided Design of Integrated Circuits and Systems,* vol. 14, pp. 137-158, 1993.

[39] L. M. Silveira, M. Kamon, J. White, L. Miguel, S. Mattan, and K. J. White, "Efficient reduced-order modeling of frequency-dependent coupling inductances associated with 3-D interconnect structures," in *Proc. ACM/IEEE,* 1995, pp. 474-479.

[40] R. W. Freund, "Reduced-order modeling techniques based on Krylov subspaces and their use in circuit simulation," Bell Laboratories, Murray Hill, NJ, Numerical Analysis Manuscript No. 98-3-02, Feb. 1998.

[41] A. C. Cangellaris, M. Celik, S. Pasha, and L. Zhao, "Electromagnetic model order reduction for system-level modeling," *IEEE Transactions on Microwave Theory Application,* vol. 47, pp. 840-850, June 1999.

[42] D. Li and S. X. D. Tan, "Hierarchical Krylov subspace reduced order modeling of large RLC circuits," *in Proc. Asia and South Pacific Design Automation Conference*, 2008, pp. 170-175.

[43] A. C. Antoulas, "An overview of approximation methods for large-scale dynamical systems," *Annual Review in Control*, vol. 29, pp. 181-190, 2005.

[44] D. M. Vasilyev, "Theoretical and practical aspects of linear and nonlinear model order reduction techniques," Ph.D. dissertation, Massachusetts Inst. Technol., Cambridge, MA, 2008.

[45] A. C. Antoulas, "Approximation of large-scale dynamical systems: An overview," *International Journal of Applied Mathematics and Computer Science*, vol. 11, pp. 1093-1121, 2005.

[46] P. J. Heres, "Robust and efficient Krylov subspace methods for model order reduction," Department of Mathematics and Computer Science, Technische Universiteit Eindhoven, Eindhoven, 2005.

[47] W. H. A. Schilders, H. A. van der Vorst, and J. Rommes, Eds., *Model Order Reduction: Theory, Research Aspects and Applications*. Berlin, Germany: Springer, 2008.

[48] P. Benner, V. Mehrmann, and D. C. Sorensen, Eds., *Dimension Reduction of Large-Scale Systems*. Berlin, Germany: Springer-Verlag, 2005.

[49] R. Subbayyan and M. C. Vaithilingam, "Walsh function approach for simplification of linear systems," in *Proc. of IEEE,* vol. 67, pp. 1676-1678, Dec. 1979.

[50] B. H. Wilson, B. Shafai, and V. Uddin, "A structurally based approach to model order reduction using bond graphs," in *Proc. American Control Conference*, 1998, pp. 151-156.

[51] E. Gad and M. Nakhla, "Efficient model reduction of linear periodically time-varying systems via compressed transient system function," *IEEE Transactions on Circuits and Systems-I: Regular Papers,* vol. 52, pp. 1188-1204, June 2005.

[52] S. Mei and Y. I. Ismail, "Stable parallelizable model order reduction for circuits with frequency-dependent elements," *IEEE Transactions on Circuit and Systems II,* vol. 56, pp. 1214-1220, June 2009.

[53] A. Odabasioglu, M. Celik, and L. T. Pileggi, "PRIMA: Passive reduced-order interconnect macromodeling algorithm," *IEEE Transactions on Computer-Aided Design of Integrated Circuits and Systems*, vol. 17, pp. 645-654, Aug. 1998.

[54] C. C. Chu, M. H. Lai, and W. S. Feng, "The global Lanczos method for MIMO interconnect order reductions," in *Proc. IEEE International Symposium on Circuits and Systems*, 2006, pp. 1103-1106.

[55] M. H. Lai, C. C. Chu, and W. S. Feng, "MIMO interconnects order reductions by using the global Arnoldi algorithm," in *Proc. IEEE International Symposium on Circuits and Systems*, 2006, pp. 1107-1110.

[56] G. Shi and C. J. R. Shi, "Model-order reduction by dominant subspace projection: Error bound, subspace computation, and circuit applications," *IEEE Transactions on Circuits and Systems I*, vol. 52, pp. 975-993, May 2005.

[57] *Control System Toolbox 8: User's Guide*, The MathWorks Inc., 2009.

[58] R. C. Degeneff, M. R. Gutierrez, S. J. Salon, D. W. Burow, and R. J. Nevins, "Kron reduction method applied to the time stepping finite element analysis of induction machines," *IEEE Transactions on Energy Conversion*, vol. 10, pp. 669-674, Dec. 1995.

[59] F. E. Cellier and E. Kofman, *Continuous System Simulation*. NewYork, NY: Springer-verlag, 2006.

[60] G. Kron, *Tensor Analysis of Networks*. NewYork, NY: General Electric Series, 1939.

[61] P. J. McKenny and J. M. Schneider, "Linear, lumped parameter transformer model reduction technique," *IEEE Transactions on Power Delivery*, vol. 10, pp. 853-861, April 1995.

[62] H. W. Dommel, "Digital computer solution of electromagnetic transients in single and multiphase networks," *IEEE Transactions on Power Apparatus and Systems*, vol. PAS-88, pp. 388-399, April 1969.

[63] M. Gutierrez, R. C. Degeneff, S. J. Salon, and S. Raedy, "Transient finite element analysis computational reduction technique," *IEEE Transactions on Magnetics*, vol. 30, pp. 2992-2995, Sept. 1994.

[64] K. C. Sou, A. Megretski, and L. Daniel, "A quasi-convex optimization approach to parametrized model order reduction," *IEEE Transactions on Computer-Aided Design of Integrated Circuits and Systems*, vol. 27, pp. 456-469, March 2008.

[65] Z. Gajic and M. Lelic, "Singular perturbation analysis of system order reduction via system balancing," in *Proc. American Control Conference*, 2000, pp. 2420-2424.

[66] A. C. Antoulas, "Approximation of linear dynamical systems," in *Wiley Encyclopedia of Electrical and Computer Engineering*, vol. 11, J. G. Webster, Ed. New York, NY: John Wiley, 1999, pp. 403-422.

[67] J. Roychowdhury, "Reduced-order modeling of time-varying systems," *IEEE Transactions on Circuits and Systems II*, vol. 46, pp. 1273-1288, Oct. 1999.

[68] Y. Wan and J. Roychowdhury, "Operator-based model-order reduction of linear periodically time-varying systems," in *Proc. Design Automation Techniques*, 2005, pp. 391-396.

[69] T. B. Fowler, "A time-domain solution approach to model reduction," *IEEE Transactions on Circuits and Systems*, vol. 35, pp. 1020-1024, Aug. 1988.

[70] Y. Liu, L. T. Pileggi, and A. J. Strojwas, "FTD: Frequency to time domain conversion for reduced-order interconnect simulation," *IEEE Transactions on Circuits and Systems I*, vol. 48, pp. 500-506, April 2001.

[71] B. N. Bond and L. Daniel, "A piecewise-linear moment-matching approach to parametrized model-order reduction for highly nonlinear systems," *IEEE Transactions on Computer-Aided Design of Integrated Circuits and Systems*, vol. 26, pp. 2116-2129, Dec. 2007.

[72] A. C. Cangellaris and M. Igarashi, "Rules for robust generation of accurate reduced-order models for high-speed coupled interconnections," *IEEE Transactions on Advanced Packaging*, vol. 24, pp. 120-125, May 2001.

[73] A. C. Cangellaris, S. Pasha, J. L. Prince, and M. Celik, "A new discrete transmission line model for passive model order reduction and macromodeling of high-speed interconnections," *IEEE Transactions on Advanced Packaging*, vol. 22, pp. 356-364, Aug. 1999.

[74] M. Celik and A. C. Cangellaris, "Simulation of multiconductor transmission lines using Krylov subspace order-reduction techniques," *IEEE Transactions on Computer-Aided Design of Integrated Circuits and Systems*, vol. 16, pp. 485-496, May 1997.

[75] A. C. Cangellaris, M. Celik, S. Pasha, and L. Zhao, "Electromagnetic model order reduction for system-level modeling," *IEEE Transactions on Microwave Theory and Techniques*, vol. 47, pp. 840-850, June 1999.

[76] Y. Zhu and A. C. Cangellaris, "A new finite element model for reduced order electromagnetic modeling," *IEEE Microwave and Wireless Components Letters*, vol. 11, pp. 211-213, May 2001.

[77] H. Wu and A. C. Cangellaris, "Model-order reduction of finite-element approximations of passive electromagnetic devices including lumped electrical-circuit models," *IEEE Transactions on Microwave Theory and Techniques*, vol. 52, pp. 2305-2313, Sept. 2004.

[78] D. Chaniotis and M. A. Pai, "Model reduction in power systems using Krylov subspace methods," *IEEE Transactions on Power Systems,* vol. 20, pp. 888-894, May 2005.

[79] M. Rewienski and J. White, "A trajectory piece-wise linear approach to model order reduction and fast simulation of nonlinear circuits and micromachined devices," *IEEE Transactions on Computer-Aided Micromachined Device*, vol. 22, pp. 155-170, Feb. 2003.

[80] M. Celik, A. Atalar, and M. A. Tan, "Transient analysis of nonlinear circuits by combining asymptotic waveform evaluation with volterra series," *IEEE Transactions on Circuits and Systems I,* vol. 42, pp. 470-473, Aug. 1995.

[81] D. Vasilyev, M. Rewienski, and J. White, "A TBR-based trajectory piecewise-linear algorithm for generating accurate low-order models for nonlinear analog circuits and mems," in *Proc. ACM/IEEE Design Automation Conference*, 2003, pp. 490-495.

[82] N. Dong and J. Roychowdhury, "Piecewise polynomial nonlinear model reduction," in *Proc. Design Automation Conference*, 2003, pp. 484-489.

[83] N. Dong and J. Roychowdhury, "General-purpose nonlinear model order reduction using piecewise polynomial representation," *IEEE Transactions on Computer-Aided Design of Integrated Circuits and Systems,* vol. 27, pp. 249-264, Feb. 2008.

[84] Y. Chen and J. White, "A quadratic method for nonlinear model reduction," in *Proc. International Conference on Modeling and Simulation of Microsystems*, 2000, pp. 477-480.

[85] N. Dong and J. Roychowdhury, "Automated nonlinear macromodelling of output buffers for high-speed digital applications," in *proc. 42nd ACM/IEEE Des. Autom. Conf.*, 2005, pp. 51-56.

[86] K. Willcox and J. Peraire, "Balanced model reduction via the proper orthogonal decomposition," *AIAA Journal*, vol. 13, pp. 2323-2330, Nov. 2002.

[87] B. N. Bond and L. Daniel, "Stable reduced models for nonlinear descriptor systems through piecewise-linear approximation and projection," *IEEE Transactions on Computer-Aided Design of Integrated Circuits and Systems,* vol. 28, pp. 1467-1480, Oct. 2009.

[88] S. Pullela, N. Menezes, and L. T. Pileggi, "Moment-sensitivity-based wire sizing for skew reduction in on-chip clock nets," *IEEE Transactions on Computer-Aided Design of Integrated Circuits and Systems,* vol. 16, pp. 210-215, Feb. 1997.

[89] L. Daniel, O. C. Siong, L. S. Chay, K. H. Lee, and J. White, "A multiparameter moment matching model reduction approach for generating geometrically parametrized interconnect performance models," *IEEE Transactions on Computer-Aided Design of Integrated Circuits and Systems,* vol. 23, pp. 678-693, May 2004.

[90] L. Daniel and J. White, "Automatic generation of geometrically parameterized reduced order models for integrated spiral RF-inductors," in *Proc. IEEE International Workshop on Behavioral Modeling and Simulation*, 2003, pp. 18-23.

[91] J. R. Philips, "Variational interconnect analysis via PMTBR," in *Proc. IEEE/ACM International Conference on Computer-Aided Design*, 2004, pp. 872-879.

[92] B. Bond and L. Daniel, "Parameterized model order reduction of nonlinear dynamical systems," *in Proc. IEEE/ACM International Conference on Computer-Aided Design*, 2005, pp. 487-494.

[93] D. C. Jiles and D. L. Atherton, "Ferromagnetic hysteresis," *IEEE Transactions on Magnetics*, vol. 19, pp. 2183-2185, Sept. 1983.

[94] D. C. Jiles and D. L. Atherton, "Theory of ferromagnetic hysteresis," *Journal of Applied Physics*, vol. 55, pp. 2115-2120, March 1984.

[95] F. Preisach, "Uber die magnetische nachwirkung," *Zeitschrift für Physik*, vol. 94, pp. 277-302, 1935.

[96] J. H. Chan, A. Vladimirescu, X. C. Gao, P. Liebmann, and J. Valainis, "Nonlinear transformer model for circuit simulation," *IEEE Transactions on Computer-Aided Design of Integrated Circuits and Systems*, vol. 10, pp. 476-482, April 1991.

[97] K. H. Carpenter, "A wide bandwidth dynamic hysteresis model for magnetization in soft ferrites," *IEEE Transactions on Magnetics*, vol. 28, pp. 2037-2040, Sept. 1992.

[98] M. L. Hodgdon, "Applications of a theory of ferromagnetic hysteresis,," *IEEE Transactions on Magnetics*, vol. 27, pp. 4404-4406, Nov. 1991.

[99] P. R. Wilson, J. N. Ross, and A. D. Brown, "Modeling frequency-dependent losses in ferrite cores," *IEEE Transactions on Magnetics*, vol. 40, pp. 1537-1541, May 2004.

[100] Y. Chen and P. Pillay, "An improved formula for lamination core loss calculations in machines operating with high frequency and high flux density excitation," in *37th Industry Application Conference*, 2002, pp. 759-766.

[101] T. Sato and Y. Sakaki, "Physical meaning of equivalent loss resistance of magnetic cores," *IEEE Transactions on Magnetics*, vol. 26, pp. 2894-2897, Sept. 1990.

[102] C. D. Graham, "Physical origin of losses in conducting ferromagnetic materials," *Journal of Applied Physics*, vol. 53, pp. 8276-8280, Nov. 1982.

[103] W. Roshen, "Iron losses in permanent magnet synchronous motors," in *Proc. 31st Annual IEEE Industrial Electronics Conference*, 2005, pp. 2566-2569.

[104] W. Roshen, "Ferrite core loss for power magnetic components design," *IEEE Transactions on Magnetics*, vol. 27, pp. 4407-4415, Nov. 1991.

[105] W. A. Roshen, "Magnetic losses for non-sinusoidal waveforms found in AC motors," *IEEE Transactions on Power Electronics,* vol. 21, pp. 1138-1141, July 2006.

[106] W. A. Roshen, "A practical, accurate and very general core loss model for nonsinusoidal waveforms," *IEEE Transactions on Power Electronics,* vol. 22, pp. 30-40, Jan. 2007.

[107] R. H. Pry and C. P. Bean, "Calculation of the energy loss in magnetic sheet materials using a domain model," *Journal of Applied Physics,* vol. 29, pp. 532-533, 1958.

[108] G. Bertotti, "General properties of power losses in soft ferromagnetic materials," *IEEE Transactions on Magnetics,* vol. 24, pp. 621-630, Jan. 1988.

[109] F. Fiorillo and A. Novikov, "An improved approach to power losses in magnetic lamination under nonsinusoidal induction waveform," *IEEE Transactions on Magnetics,* vol. 26, pp. 2904-2910, Sept. 1990.

[110] E. E. Kriezis, T. D. Tsiboukis, S. M. Panas, and J. A. Tegopoulos, "Eddy current: Theory and applications," in *Proceedings of the IEEE,* vol. 80, pp. 1559-1589, Oct. 1992.

[111] J. Gyselinck, L. Vandevelda, and J. Melkebeek, "Calculation of eddy currents and associated losses in electrical steel lamination," *IEEE Transactions on Magnetics,* vol. 35, pp. 1191-1194, May 1999.

[112] T. C. O'Connell and P. T. Krein, "The Schwarz-Christoffel analytical method applied to electric machine slot shape optimization," in *Proc. IEEE International Electric Machines and Drives Conference,* 2007, pp. 341-346.

[113] T. C. O'Connell and P. T. Krein, "A Schwarz-Christoffel-based analytical method for electric machine field analysis," *IEEE Transactions on Energy Conversion,* vol. 24, pp. 565-577, Sept. 2009.

[114] D. C. J. Krop, E. A. lomonova, and A. J. A. Vandenput, "Application of Schwarz-Christoffel mapping to permanent-magnet linear motor analysis," *IEEE Transactions on Magnetics,* vol. 44, pp. 352-359, March 2008.

[115] A. J. Adzima, P. T. Krein, and T. C. O'Connell, "Investigation of accelerating numerical-field analysis methods for electric machines with the incorporation of graphic-processor based parallel processing techniques," in Proc. *Electric Ship Technologies Symposium*, 2009, pp. 59-64.

[116] J. Cale, S. D. Sudhoff, and L. Q. Tan, "Accurately modeling EI core inductors using a high-fidelity magnetic equivalent circuit approach," *IEEE Transactions on Magnetics,* vol. 42, pp. 40-46, Jan. 2006.

[117] B. Lequesne, "Dynamic model of solenoids under impact excitations, including motion and eddy currents," *IEEE Transactions on Magnetics,* vol. 26, pp. 1107-1116, March 1990.

[118] W. N. Fu, S. L. Ho, H. L. Li, H. C. Wong, "An effective method to reduce the computing time of nonlinear time-stepping finite-element magnetic field computation," *IEEE Transactions on Magnetics,* vol. 38, pp. 441-444, March 2002.

[119] R. Lee and V. Chupongstimun, "A partitioning technique for the finite element solution of electromagnetic scattering from electrically large dielectric cylinders," *IEEE Transactions on Antennas and Propagation,* vol. 42, pp. 737-741, May 1994.

[120] J. Shaeffer, "Direct solve of electrically large integral equations for problem sizes to 1 M unknowns," *IEEE Transactions on Antennas and Propagation,* vol. 56, pp. 2306-2313, Aug. 2008.

[121] E. C. Cherry, "The duality between the inter-linked electric and magnetic circuits," in *Proc. Physical Society,* 1949, pp. 101-111.

[122] C. J. Carpenter, "Magnetic equivalent circuits," in *Proceedings of the IEEE,* vol. 115, pp. 1503-1511, Oct. 1968.

[123] A. D. Brown, J. N. Ross, and K. G. Nichols, "Time-domain simulation of mixed nonlinear magnetic and electronic systems," *IEEE Transactions on Magnetics,* vol. 37, pp. 522-532, Jan. 2001.

[124] A. D. Brown, J. N. Ross, K. G. Nichols, and M. D. Penny, "Simulation of magneto-electric systems using kirchoffian networks," in *Proc. Eur. Conf. Magn. Sen. Act.,* 1998.

[125] M. Yilmaz and P. T. Krein, "Capabilities of finite element analysis and magnetic equivalent circuits for electrical machine analysis and design," in *Proc. 39th IEEE Power Electronics Specialists Conference,* 2008, pp. 4027-4033.

[126] M. Amrhein and P. T. Krein, "3-D magnetic equivalent circuit framework for modeling electromechanical devices," *IEEE Transactions on Energy Conversion,* vol. 24, pp. 397-405, June 2009.

[127] H. W. Derbas, J. M. Williams, A. C. Koenig, and S. D. Pekarek, "A comparison of nodal- and mesh-based magnetic equivalent circuits," *IEEE Transactions on Energy Conversion,* vol. 24, pp. 388-396, June 2009.

[128] M. Amrhein and P. T. Krein, "Magnetic equivalent circuit modeling of induction machines design-oriented approach with extension to 3-D," in *Proc. IEEE International Electric Machines and Drives Conference,* 2007, pp. 1557-1563.

[129] M. Amrhein and P. T. Krein, "Magnetic equivalent circuit simulations of electrical machines for design purposes," in *Proc. IEEE Electric Ship Technologies Symposium,* 2007, pp. 254-260.

[130] B. M. Nee and P. L. Chapman, "Integrated filter elements in electric drives," in *Proc. IEEE Vehicle Power and Propulsion Conference,* 2007, pp. 148-153.

[131] S. D. Sudhoff, B. T. Kuhn, K. Crozine, and B. T. Branecky, "Magnetic equivalent circuit modeling of induction motors," *IEEE Transactions on Energy Conversion,* vol. 22, pp. 259-270, June 2007.

[132] C. Delforge and B. Lemaire-Semail, "Induction machine modeling using finite element and permeance network methods," *IEEE Transactions on Magnetics,* vol. 31, pp. 2092-2095, May 1995.

[133] V. Ostovic, "A simplified approach to magnetic equivalent-circuit modeling of induction machines," *IEEE Transactions on Industry Applications,* vol. 24, pp. 308-316, march/April 1988.

[134] V. Ostovic, J. M. Miller, V. K. Garg, R. D. Schultz, and S. H. Swales, "A magnetic-equivalent-circuit-based performance computation of a Lundell alternator," *IEEE Transactions on Industry Applications,* vol. 35, pp. 825-830, July-Aug 1999.

[135] M. Amrhein and P. T. Krein, "Force calculation in 3-D magnetic equivalent circuit networks with a Maxwell stress tensor," *IEEE Transactions on Energy Conversion,* vol. 24, pp. 587-593, Sept. 2009.

[136] R. Qin and M. A. Rahman, "Magnetic equivalent circuit of PM hysteresis synchronous motor," *IEEE Transactions on Magnetics,* vol. 39, pp. 2998-3000, Sept. 2003.

[137] J. M. Kokernak and D. A. Torrey, "Magnetic circuit model for the mutually coupled switched-reluctance machine," *IEEE Transactions on Magnetics,* vol. 36, pp. 500-507, March 2000.

[138] K. F. Ramussen, J. H. Davies, T. J. E. Miller, M. I. McGilp, and M. Olaru, "Analytical and numerical computation of air-gap magnetic fields in brushless motors with suface permanent magnets," *IEEE Transactions on Industry Applications,* vol. 36, pp. 1547-1554, Nov./Dec. 2000.

[139] J. Hur, S. B. Yoon, D. Y. Hwang, and D. S. Hyun, "Analysis of PMLSM using three dimensional equivalent magnetic circuit network methods," *IEEE Transactions on Magnetics,* vol. 33, pp. 4143-4145, Sept. 1997.

[140] A. Yoshitake, K. Harada, T. Todaka, and Y. Ishihara, "Dynamic analysis of a linear oscillatory actuator under feedback control," *IEEE Transactions on Magnetics,* vol. 33, pp. 1662-1665, March 1997.

[141] J. R. Brauer and Q. M. Chen, "Alternative dynamic electromechanical models of magnetic actuators containing eddy currents," *IEEE Transactions on Magnetics,* vol. 36, pp. 1333-1336, July 2000.

[142] F. Sixdenier, M.-A. Raulet, R. Marion, R. Goyet, G. Clerc, and F. Allab, "Dynamical models for eddy current in ferromagnetic cores introduced in an FE-tuned magnetic equivalent circuit of an electromagnetic relay," *IEEE Transactions on Magnetics,* vol. 44, pp. 866-869, June 2008.

[143] M. Moallem and G. E. Dawson, "An improved magnetic equivalent circuit method for predicting the characteristics of highly saturated electromagnetic devices," *IEEE Transactions on Magnetics*, vol. 34, pp. 3632-3635, Sept. 1998.

[144] M. A. Batdorff and J. H. Lumkes, "High-fidelity magnetic equivalent circuit model for an axisymmetric electromagnetic actuator," *IEEE Transactions on Magnetics*, vol. 45, pp. 3064-3072, August 2009.

[145] J. Sagarduy, A. J. Moses, and F. J. Anayi, "Eddy current losses in electrical steels subjected to matrix and classical PWM excitation waveforms," *IEEE Transactions on Magnetics*, vol. 42, pp. 2818-2820, Oct. 2006.

[146] Y. Gao, K. Muramatsu, K. Shida, K. Fujiwara, S. Fukuci, and T. Takahata, "Loss calculation of reactor connected to inverter power supply taking account of eddy currents in laminated steel core," *IEEE Transactions on Magnetics*, vol. 45, pp. 1044-1047, March 2009.

[147] D. Ribbenfjard and G. Engdahl, "Novel method for modeling of dynamic hysteresis," *IEEE Transactions on Magnetics*, vol. 44, pp. 854-857, June 2008.

[148] E. J. Tarasiewicz, A. S. Morehed, A. Narang, and E. P. Dick, "Frequency dependent eddy current models for nonlinear iron cores," *IEEE Transactions on Power Systems*, vol. 8, pp. 588-597, May 1993.

[149] F. Deleon and A. Semlyen, "Time domain modeling of eddy current effects for transformer transients," *IEEE Transactions on Power Delivery*, vol. 8, pp. 271-280, Jan. 1993.

[150] S. Y. R. Hui, J. G. Zhu, and V. S. Ramsden, "A generalized dynamic circuit model of magnetic cores for low- and high-frequency applications – Part I: theoretical calculation of the equivalent core loss resistance," *IEEE Transactions on Power Electronics*, vol. 11, pp. 246-250, March 1996.

[151] S. Y. R. Hui, J. G. Zhu, and V. S. Ramsden, "A generalized dynamic circuit model of magnetic cores for low- and high-frequency applications – Part II: circuit model formulation and implementation," *IEEE Transactions on Power Electronics*, vol. 11, pp. 251-259, March 1996.

[152] J. G. Zhu, S. Y. R. Hui, and V. S. Ramsdon, "A dynamic equivalent circuit model for solid magnetic cores," in *Proc. 24th IEEE Power Electronics Specialists Conference*, 1993, pp. 1111-1115.

[153] J. G. Zhu, S. Y. R. Hui, and V. S. Ramsdon, "Discrete modeling of magnetic cores including hysteresis eddy current and anomalous losses," in *Proc. of IEEE*, vol. 140, pp. 317-322, July 1993.

[154] J. G. Zhu, S. Y. R. Hui, and V. S. Ramsdon, "A dynamic equivalent circuit model for solid magnetic cores for high switching frequency operations," *IEEE Transactions on Power Electronics,* vol. 10, pp. 791-795, Nov. 1995.

[155] J. A. M. Velasco and B. A. Mork, "Transformer modeling for low frequency transients – The state of the art," in *Proc. International Conference on Power Systems Transients*, 2003, pp. 1-6.

[156] O. Bottauscio, A. Manzin, A. Canova, M. Chiampi, G. Grusso, and M. Repetto, "Field and circuit approaches for diffusion phenomena in magnetic cores," *IEEE Transactions on Magnetics,* vol. 40, pp. 1322-1325, March 2004.

[157] K. C. Wicks, W. G. Dunford, and L. R. Lineares, "A dynamic circuit-based ferromagnetic model," *IEEE Transactions on Circuits and Systems,* vol. 56, pp. 2292-2300, Oct. 2009.

[158] R. Prieto, R. Asensi, C. Fernandez, J. A. Oliver, and J. A. Cobos, "Bridging the gap between FEA field solution and the magnetic component model," *IEEE Transactions on Power Electronics,* vol. 22, pp. 943-951, May 2007.

[159] S. M. Lee, S. H. Lee, C. H. Soon, and I. H. Park, "Reduced modeling of eddy current-driven electromechanical system using conductor segmentation and circuit parameters extracted by FEA," *IEEE Transactions on Magnetics,* vol. 41, pp. 1448-1451, May 2005.

[160] S. Rutenkroger, B. Denken, and S. Pekarek, "Reduction of model dimension in nonlinear finite element approximations of electromagnetic systems," in *Proc. 9th IEEE Workshops on Computer Applications in Power Electronics*, 2004, pp. 20-27.

[161] Y. Zhai and L. V. Quoc, "Analysis of power magnetic components with nonlinear static hysteresis: Proper orthogonal decomposition and model reduction," *IEEE Transactions on Magnetics,* vol. 43, pp. 1888-1897, May 2007.

[162] J. D. Owens and P. L. Chapman, "Reduced FEA-state space modeling of stationary magnetic devices," in *Proc. 34th IEEE Power Electronics Specialists Conference*, 2003, pp. 265-271.

[163] J. D. Owens and P. L. Chapman, "Automated generation of accurate low-order models for magnetic devices," *IEEE Transactions on Power Electroics,* vol. 20, pp. 732-742, July 2005.

[164] L. Qu and P. L. Chapman, "Extraction of low-order non-linear inductor models from a high-order physics-based representation," *IEEE Transactions on Power Electronics,* vol. 21, pp. 813-817, May 2006.

[165] L. Qu and P. L. Chapman, "Extraction of dynamic low-order nonlinear inductor models based on steady state solutions," in *Proc. 37th IEEE Power Electronics Specialists Conference*, 2006, pp. 1-9.

[166] L. Qu and P. L. Chapman, "Toward a system for automatic extraction of low-order models for magnetic devices," in *Proc. IEEE Workshops on Computers in Power Electronics*, 2006, pp. 193-198.

[167] L. Qu and P. L. Chapman, "Extraction of dynamic low order models for multiwinding magnetic devices based on finite element analysis," in *Proc. 39th IEEE Power Electronics Specialists Conference*, 2008, pp. 4611-4416.

[168] L. Qu and P. L. Chapman, "Extraction of dynamic, low-order models for magnetic devices based on finite element analysis with hysteresis," in *Proc. 38th IEEE Power Electronics Specialists Conference*, 2007, pp. 2082-2088.

[169] Micrometals, Inc. (2005). [Online]. Available: http://www.micrometals.com /images/curves/2640BH.html.

[170] *Lamination Steels: Types, Properties, and Specifications*, The Electric Motor Education and Research Foundation, South Dartmouth, MA, 2007.

[171] Z. Liu, *et al.*, "Equivalent hardware representation of PM synchronous motors from the physics-based phase variable model obtained through FE computation," *IEEE Transactions on Magnetics*, vol. 45, pp. 1450-1453, March 2009.

[172] Ferroxcube Inc., http://www.ferroxcube.com.

[173] R. C. Degeneff, M. R. Gutierrez, and P. J. McKenny, "A method for constructing reduced order transformer models for system studies from detailed lumped parameter models," *IEEE Transactions on Power Delivery*, vol. 7, pp. 649-655, April 1992.

[174] F. D. Leon and A. Semlyen, "Reduced order model for transformer transients," *IEEE Transactions on Power Delivery*, vol. 7, pp. 361-369, Jan. 1992.

[175] W. G. Hurley, W. H. Wolfle, and J. G. Breslin, "Optimized transformer design: Inclusive of high-frequency effects," *IEEE Transactions on Power Electronics*, vol. 13, pp. 651-659, July 1998.

[176] G. Liang, H. Sun, X. Zhang, and X. Cui, "Study on parameter calculation and order reduction of transformer model," in *Proc. International Conference on Power System Technology*, 2004, pp. 487-491.

[177] D. Ioan and I. Munteanu, "Models for capacitive effects in iron core transformers," *IEEE Transactions on Magnetics*, vol. 36, pp. 990-994, July 2000.

[178] G. Liang, M. Yao, H. Dong, and C. Ji, "Modeling of transformer windings under VFTO using the lumped element equivalent circuit appraoch," in *Proc. DRPT*, 2008, pp. 1109-1114.

[179] S. M. Lee, S. H. Lee, H. S. Choi, and I. H. Park, "Reduced modeling of eddy current-driven electromechanical system conductor segmentation and circuit parameter extracted by FEA," *IEEE Tran. Magnetics,* vol. 41, pp. 1448-1451, May 2005.

[180] O. Bottauscio, M. Chiampi, and A Manzin, "Advanced model for dynamic analysis of electromechanical devices," *IEEE Transactions on Magnetics,* vol. 41, pp. 36-46, Jan. 2005.

[181] H. Mohellebi,M. E. Latreche, and M. Feliachi, "Coupled axisymmetric analytical and finite element analysis for induction devices having moving parts," *IEEE Transactions on Magnetics,* vol. 34, pp. 3308–3310, Sept. 1998.

[182] J. M. Jin, *The Finite Element Method in Electromagnetics*. NewYork, NY: Wiley, 1993.

[183] S. J. Salon, *Finite element analysis of electrical machines*. Boston, MA: Kluwer, 1995.

[184] P. Pejovic and D. Maksimovic, "A method for fast time-domain simulation of networks with switches," *IEEE Transactions on Power Electronics,* vol. 9, pp. 449-456, July 1994.

[185] H. S. Chung and A. Ioinovici, "Fast computer-aided simulation of switching power regulator based on progressive analysis of the switches' state," *IEEE Transactions on Power Electronics,* vol. 9, pp. 206-212, March 1994.

[186] A. M. Luciano and A. G. M. Strollo, "A fast time-domain algorithm for the simulation of switching power converters," *IEEE Transactions on Power Electronics,* vol. 5, pp. 363-370, July 1990.

[187] H. J. Wu and W. S. Feng, "Efficient simulation of switched networks using reduced unification matrix," *IEEE Transactions on Power Electronics,* vol. 14, pp. 481-494, May 1999.

[188] T. Kato, K. Inoue, and J. Ogoshi, "Efficient multi-rate steady-state analysis of a power electronic system by the envelope following method," in *Proc. 38th IEEE Power Electronics Specialists Conference,* 2007, pp. 2103-2108.

[189] D. Li and R. Tymerski, "Comparison of simulation algorithms for accelerated determination of periodic steady state of switched networks," *IEEE Transactions on Industrial Electronics,* vol. 47, pp. 1278-1285, Dec. 2000.

[190] K. K. Tse, S. H. Chung, and S. Y. R. Hui, "Stepwise quadratic state-space modeling technique for simulation of power electronics circuits," *IEEE Transactions on Industrial Electronics,* vol. 46, pp. 91-99, Feb. 1999.

[191] J. White and S. B. Leeb, "An envelop-following approach to switching power converter simulation," *IEEE Transactions on Power Electronics,* vol. 6, pp. 303-307, April 1991.

[192] L. Wang, J. Jatskevich, and S. Pekarek, "Modeling of induction machines using a voltage-behind-reactance formulation," *IEEE Transactions on Energy Conversion,* vol. 23, pp. 382-392, 2008.

[193] L. Wang, A. Davoudi, J. Jatskevich, and P. L. Chapman, "Accelerated state-variable modeling of synchronous machine-converter systems," in *Proc. International Symposium on Circuits and Systems,* 2008, pp. 3037-3040.

[194] R. E. Araujo, A. V. Letie, and D. S. Freitas, "Modeling and simulation of power electronic systems using a bond graph formalism," in *Proc. 10th Mediterranean Conference on Control and Automation*, 2002.

[195] M. Filippa, M. Chunting, J. Shen, and R. C. Stevenson, "Modeling of a hybrid electric vehicle powertrain test cell using bond graphs," in *Proc. Power Electronics in Transportation*, 2004, pp. 167-172.

[196] B. Allard, H. Helali, C. C. Lin, and H. Morel, "Power converter average model computation using the bond graph and Petri net techniques," in *Proc. 26th IEEE Power Electronics Specialists Conference*, 1995, pp. 830-836.

[197] J. Mahdavi, A. Emaadi, M. D. Bellar, and M. Ehsani, "Analysis of power electronics converters using the generalized state-space averaging approach," *IEEE Transactions on Circuits and Systems- I,* vol. 44, pp. 767-770, Aug. 1997.

[198] A. Emadi, "Modeling of power electronics loads in AC distribution systems using the generalized state-space averaging method," *IEEE Transactions on Industrial Electronics,* vol. 51, pp. 992-1000, Oct. 2004.

[199] A. Emadi, "Modeling and analysis of multiconverter DC power electronic systems using the generalized state-space averaging method," *IEEE Transactions on Industrial Electronics*, vol. 51, pp. 661-668, June 2004.

[200] V. A. Caliskan, O. C. Verghese, and A. M. Stankovic, "Multifrequency averaging of dc/dc converters," *IEEE Transactions on Power Electronics,* vol. 14, pp. 124-133, Jan. 1999.

[201] D. Maksimovic, A. M. Stankovic, V. J. Thottuvelli, and G. C. Verghese, "Modeling and simulation of power electronics converters," in *Proc. The IEEE,* vol. 89, pp. 898-912, June 2001.

[202] K. Strunz, "Flexible numerical integration for efficient representation of switching in real time electromagnetic transients simulation," *IEEE Transactions on Power Delivery,* vol. 19, pp. 1276-1283, July 2004.

[203] B. D. Kelper, H. F. Blanchetter, and L. A. Dessaint, "Switching time model updating for the real-time simulation of power-electronic circuits and motor drives," *IEEE Transactions on Energy Conversion,* vol. 20, pp. 181-186, March 2005.

[204] L. F. Shampine and M. W. Reichelt, "The MATLAB ODE suite," *SIAM Journal on Scientific Computing*, vol. 18, pp. 1-22, 1997.

[205] U. M. Ascher and L. R. Petzold, *Computer Methods for Ordinary Differential Equations and Differential-Algebraic Equations*. Philadelphia, PA: SIAM, 1998.

[206] S. D. Sudhoff, J. L. Tichenor, and J. L. Drewniak, "Wide bandwidth multi-resolutional analysis of a surface-mounted PM synchronous machine," *IEEE Transactions on Energy Conversion*, vol. 14, pp. 1011-1018, Dec. 1999.

[207] P. L. Chapman, "Multi-resolution switched system modeling," in *Proc. IEEE Workshops on Power Electronics*, 2004, pp. 167-172.

[208] S. D. Pekarek et al., "An efficient multirate simulation technique for power-electronics-based systems," *IEEE Transactions on Power Systems*, vol. 19, pp. 399-409, Feb. 2004.

[209] M. L. Crow and J. G. Chen, "The multirate method for simulation of FACTS devices in power system dynamics," *IEEE Transactions on Power Systems*, vol. 11, pp. 376-382, Feb. 1996.

[210] M. L. Crow and J. G. Chen, "The multirate method for simulation of power system dynamics," *IEEE Transactions on Power Systems*, vol. 9, pp. 1684-1690, Aug. 1994.

[211] T. Kato, K. Inoue, T. Fukutani, and Y. Kanda, "Multirate analysis method of a power electronic converter by circuit partitioning," in *Proc. 37th IEEE Power Electronics Specialists Conference*, 2006, pp. 1-7.

[212] R. E. Crosbie, J. J. Zenor, R. Bednar, D. Word, and N. G. Hingorani, "Multi-rate simulation techniques for electric ship design," in *Proc. IEEE Electric Ship Technologies Symposium*, 2007, pp. 384-389.

[213] C. E. Lucas, E. A. Walters, J. Jatskevich, O. Wasynczuk, and P. T. Lamm, "Communication interval selection in distributed heterogeneous simulation of large-scale dynamical systems," in *Proc. International Society for Optical Engineering*, 2003, pp. 86-97.

[214] Y. Luo, R. Dougal, and E. Santi, "Multi-resolution modeling of power converter using waveform reconstruction," in *Proc. 33rd Annual Simulation Symposium*, 2000, pp. 165-174.

[215] P. T. Krein and R. M. Bass, "A new approach to fast simulation of periodically switching power converters," in *Proc. IEEE Industrial Applications Society Annual Meeting*, 1990, pp. 1185-1189.

[216] H. Wu, R. Dougal. and C. Jin, "Modeling power diode by combining the behavioral and the physical model," in *Proc. 31st Annual Conference of IEEE Industerial Electronics Society*, 2005, pp. 685-690.

[217] H. Wu and R. Dougal, "Dynamic multi-resolution modeling of power super capacitor," in *Proc. 37th Annual North American Power Symposium*, 2005, pp. 241-246.

[218] P. W. Sauer, D. J. LaGesse, S. Ahmed-Zaid, and M. A. Pai, "Reduced-order modeling of interconnected multimachine power systems using time-scale decomposition," *IEEE Transactions on Power Systems*, vol. PWRS-2, pp. 310-319, May 1987.

[219] P. W. Sauer, S. Ahmed-zaid, and P. V. Kokotovic, "An integral manifold approach to reduced order dynamic modeling of synchronous machines," *IEEE Transactions on Power Systems*, vol. 3, pp. 17-23, 1988.

[220] S. Ahmed-zaid, P. Sauer, M. Pai, and M. Sarioglu, "Reduced order modeling of synchronous machines using singular perturbation," *IEEE Transactions on Circuits and Systems*, vol. 29, pp. 782-786, 1982.

[221] Z. Sorchini and P. T. Krein, "Formal derivation of direct torque control for induction machines," *IEEE Transactions on Power Electronics*, vol. 21, pp. 1428-1436, Sept. 2006.

[222] J. W. Kimball and P. T. Krein, "Singular perturbation theory for dc-dc converters and pplication to PFC converters," *IEEE Transactions on Power Electronics*, vol. 23, pp. 2970-2981, Nov. 2008.

[223] P. K. Kokotovic, B. Avramovic, J. H. Chow, and J. R. Winkelman, "Coherency based decomposition and aggregation," *Automatica*, vol. 18, pp. 47-56, 1982.

[224] R. Podmore, "Identification of coherent generators for dynamic equivalents," *IEEE Transactions on Power System Applications*, vol. PAS-97, pp. 1344-1354, July/Aug. 1978.

[225] G. N. Ramaswary, L. Rouco, O. Filiatre, and G. C. Verghese, "Synchrony, aggeregation, and multi-area eigenanalysis," *IEEE Transactions on Power Systems*, vol. 10, pp. 1986-1993, Nov. 1995.

[226] G. N. Ramaswary, L. Rouco, O. Filiatre, and G. C. Verghese, "Synchronic modal equivalencing (SME) for structure-preserving dynamic equivaence," *IEEE Transactions on Power Systems*, vol. 11, pp. 19-29, Feb. 1996.

[227] N. Femia, S. Giovanni, and V. Tucci, "State-space models and order reduction for dc-dc switching converters in discontinous modes," *IEEE Transactions on Power Electronics*, vol. 10, pp. 640-650, Nov. 1995.

[228] L. Arnedo, D. Boroyevich, R. Burgos, and F. Wang, "Un-terminated frequency response measurements and model order reduction for black-box terminal characterization characterization models," in *Proc. 23rd Annual IEEE Applied Power Electronics Conference and Exposition*, 2008, pp. 1054-1060.

[229] L. Arnedo, D. Boroyevich, R. Burgos, and F. Wang, "Black-box terminal characterization models for the analysis and simulation of distributed power electronic

systems," in *Proc. 38th IEEE Power Electronics Specialists Conference*, 2007, pp. 1968-1973.

[230] A. Dehbi et al., "Efficient electrothermal simulation of power electronics for hybrid electric vehicles," in *Proc. International Conference on Thermal Mechanical and Multi-physics Simulation and Experiments in Microelectronics and Micro-systems*, 2008, pp. 1-7.

[231] Y. Yasuda, A. Yokoyama, and Y. Tada, "A study on effect on simulation by using reduced model of transmission network for real-time power system simulator," in *Proc. International Conference on Power System Technology*, 2002, pp. 1545-1549.

[232] A. Massarini and M. K. Kazimierczuk, "Self-capacitance of inductors," *IEEE Transactions on Power Electronics*, vol. 12, pp. 671-676, July 1997.

[233] Y. Ren, M. Xu, J. Zhou, and F. C. Lee, "Analytical loss model of power MOSFET," *IEEE Transactions on Power Electronics*, vol. 21, pp. 310-319, March 2006.

[234] "IRFP360 data sheet. " [Online]. Available http:/www.datasheetcatalog.org/datasheet/irf/irfp360.pdf.

[235] Y. C. Liang and V. J. Gosbell, "Diode forward and reverse recovery model for power electronic SPICE simulation," *IEEE Transactions on Power Electronics*, vol. 5, pp. 346-356, July 1990.

[236] E. Elwarraki and A. Sabir, "PSpice behavior and thermal modeling of the PIN diode: A circuit approach," in *Proc. 14th IEEE International Electronics, Circuits, and Systems*, 2007, pp. 1031-1034.

[237] L. V. Karadzinov and D. C. Hamill, "Analysis of the influence of diode reverse recovery on the operation and design of high-frequency rectifiers," *IEEE Transactions on Power Electronics*, vol. 15, pp. 386-398, March 2000.

[238] G. C. Verghese, M. E. Elbuluk, and J. G. Kassakian, "A general approach to sampled-data modeling for power electronics circuits," *IEEE Transactions on Power Electronics*, vol. PE-1, pp. 76-89, 1986.

[239] P. T. Krein and R. M. Bass, "Autonomous control technique for high-performance switches," *IEEE Transactions on Industerial Electronics*, vol. 39, pp. 215-222, June 1992.

[240] N. Wu, "Simulation-based average-value modeling of power electronics converters and subsystems," Ph.D. dissertation, Electrical and Computer Engineering, Purdue University, West Lafayette, IN, 2006.

[241] J. Jatskevich et al., "Continuous state-space modeling of switched networks," in *IEEE Conference on Control Application*, 2000, pp. 902-907.

[242] J. Jatskevich and T. Aboul-Seoud, "Automated state-variable formulation for power electronic circuits and systems," in *IEEE Int. Symposium on Circuit and Systems*, 2004, pp. 952-955.

[243] L. O. Chua and P. M. Lin, *Computer-Aided Analysis of Electronic Circuits: Algorithms and Computational Techniques*. Englewood Cliffs, NJ: Prentice-Hall, 1975.

[244] O. Wasynczuk and S. D. Sudhoff, "Automated state model generation algorithm for power circuits and systems," *IEEE Transactions on Power Systems,* vol. 11, pp. 1951-1956, 1996.

[245] L. F. Shampine and M. E. Hosea, "Analysis and implementation of TR-BDF2," *Applied Numerical Mathematics,* vol. 20, pp. 21-37, 1996.

[246] T. Suetsugu and M. K. Kazimierczuk, "Design procedure of Class-E amplifier for off-nominal operation at 50% duty ratio," *IEEE Transactions on Circuits and Systems- I,* vol. 53, pp. 1468-1476, July 2006.

[247] T. Suetsugu and M. K. Kazimierczuk, "Maximum operating frequency of Class-E amplifier at any duty ratio," *IEEE Transactions on Circuit and Systems- II,* vol. 55, pp. 768-770, Aug. 2008.

[248] T. Suetsugu and M. K. Kazimierczuk, "Off-nominal operation of Class-E amplifier at any duty ratio," *IEEE Transactions on Circuit and Systems- I,* vol. 54, pp. 1389-1397, June 2007.

[249] T. Suetsugu and M. K. Kazimierczuk, "Comparison of Class-E amplifier with nonlinear and linear shunt capacitance," *IEEE Transactions on Circuit and Systems- I,* vol. 50, pp. 1089-1097, Aug. 2003.

[250] J. Xu and C. Q. Lee, "A unified averaging technique for the modeling of quasi-resonant converters," *IEEE Transactions on Power Electronics,* vol. 13, pp. 556-563, May 1998.

[251] A. M. Stankovic, S. R. Sanders, and T. Aydin, "Dynamic phasors in modeling and analysis of unbalanced polyphase AC machines," *IEEE Transactions on Energy Conversion,* vol. 17, pp. 107-113, March 2002.

[252] P. Mattavelli, G. C. Verghese, and A. M. Stankovic, "Phasor dynamics of thyristor-controlled series capacitor systems," *IEEE Transactions on Power Systems,* vol. 12, pp. 1259-1267, Aug. 1997.

[253] S. Almer and U. Jonsson, "Dynamic phasor analysis of periodic systems," *IEEE Transactions on Automatic Control,* vol. 54, pp. 2007-2012, Aug. 2009.

[254] L. Qu and P. L. Chapman, "Extraction of dynamic, low-order models for magnetic devices based on finite element analysis with hysteresis," in *Proc. 38th IEEE Power Electronics Specialists Conference*, 2007, pp. 2082-2088.

[255] S. D. Sudhoff, B. T. Kuhn, and P. L. Chapman, "An induction machine model for predicting inverter-machine interaction," *IEEE Transactions on Energy Conversion,* vol. 17, pp. 203-210, June 2002.

[256] D. C. Aliprantis, S. D. Sudhoff, and B. T. Kuhn, "A synchronous machine model with saturation and arbitrary rotor network representation," *IEEE Transactions on Energy Conversion,* vol. 20, pp. 584-594, Sept. 2005.

[257] S. D. Pekarek, M. T. Lemanski, and E. A. Walters, "On the use of singular perturbations to neglect the dynamics saliency of synchronous machines," *IEEE Transactions on Energy Conversion,* vol. 17, pp. 385-391, Sept. 2002.

[258] S. D. Pekarek and E. A. Walters, "An advanced method of neglecting dynamic saliency of synchronous machines in power electronics based systems," *IEEE Transactions on Energy Conversion,* vol. 14, pp. 1177-1183, Dec. 1999.

[259] P. L. Chapman, S. D. Sudhoff, and C. A. Whitcomb, "Multiple reference frame analysis of non-sinusoidal brushless dc drives," *IEEE Transactions on Energy Conversion,* vol. 14, pp. 440-446, Sep. 1999.

[260] Toroidal cores data, T300 through T650, Micrometals, Inc. [Online]. Available: http://www.micrometals.com/pcparts /torcore7.html, 2005.

[261] Toroidal cores data, T-184 through T250, Micrometals, Inc. [Online]. Available: http://www.micrometals. com/pcparts/torcore6.html, 2005.

[262] "Nonoriented electrical steels," AK Steel Inc. [Online]. Available: http://www.aksteel. com/pdf/markets_products/electrical/Non_Oriented_Bulletin.pdf.